Magnetic pumping as a source of particle heating

by

Emily Lichko

A dissertation submitted in partial fulfillment of

the requirements for the degree of

Doctor of Philosophy

(Physics)

at the

UNIVERSITY OF WISCONSIN–MADISON

2020

Date of final oral examination: 2/14/2020

The dissertation is approved by the following members of the Final Oral Committee:

Jan Egedal, Professor, Physics
Cary B. Forest, Professor, Physics
Stanislav Boldyrev, Professor, Physics
Ellen Zweibel, Professor, Astronomy

MAGNETIC PUMPING AS A SOURCE OF PARTICLE HEATING

Emily Lichko

Under the supervision of Professor Jan Egedal

At the University of Wisconsin-Madison

Abstract

Energetic particle generation is an important component of a variety of astrophysical systems, from seed particle generation in shocks to the heating of the solar wind. Starting from the drift kinetic equation, we have derived a magnetic pumping model, where particles are heated by the largest scale turbulent fluctuations. We have shown that for a spatially-uniform flux tube, this is an effective heating mechanism up to $v \leq \omega/k$, and naturally produces power-law distributions like those observed in the solar wind, as verified by particle-in-cell simulations. When this model is extended to a spatially-varying flux tube, magnetic trapping renders magnetic pumping an effective Fermi heating process for particles with $v \gg \omega/k$. To test this, we used satellite observations of the strong, compressional magnetic fluctuations near the Earth's bow shock from the Magnetospheric MultiScale mission and found strong agreement with our model. Given the ubiquity of such fluctuations in different astrophysical systems, this mechanism has the potential to be transformative to our understanding of how the most energetic particles in the universe are generated.

Acknowledgments

First, thank you to my committee, Jan Egedal, Ellen Zweibel, Cary Forest, and Stas Boldyrev for taking the time to read and improve this thesis.

It has been a pleasure working for the past six years with my advisor, Jan Egedal. You taught me how to be a scientist and I deeply appreciate the drive for excellence that you've instilled in me over the course of graduate school.

I feel incredibly lucky to have been surrounded by an incredible support system both in and out of the department over the past seven years. I would not have made it through graduate school without them. Ethan Peterson, you are an incredible office mate and an even better friend. For the support, for the physics sanity checks, for the puppy pictures, for everything I can't possibly list, I am so grateful and feel so lucky that we became friends. John Boguski, thank you for reading everything I ever wrote in graduate school and for always being there to take a break when I needed one - I owe you a grant application. Joe Olson and Sam Greess, I really can't thank you enough for everything you've done for me over the years. Your support at the times when I was the most exhausted and overwhelmed means so much.

The sheer number of people that have lifted me up during my graduate career is overwhelming. Norah Bushman, you are an incredibly special person and I'm so lucky to have you and your friendship in my life. Kyle Bunkers, I so value your kindness and patience and steady friendship. Zach Griffith, Chelsea Griffith, Trevor Knapp, and Zach Williams, I am so grateful for your friendship. As running buddies, board gamers, and ice cream eating companions, I couldn't ask for better. Extended lunch crew, Matt Meehan, Adam Frees, Cameron King, Logan Wille, James Bourbeau, Julian Irwin, Lisa Charron, Laura Vander Woude, Claire Frees, Caitlin Bourbeau, and Sarah King I'm so happy to have had your friendship and support in my life. From buying me flowers when you could tell that I was having a rough time, to bringing the best pool toys to my barbecue, to the best Holiday Colloquium ever, to the comradery of our Sunday night Game of Thrones gatherings, you have all filled graduate school with so much joy. Vanessa López Barquero, I've loved our lunches at Med Café and I really value that I can turn to you whenever I need an honest opinion. Erin Middlemas, I can't tell you how grateful I am for all the times you've helped me talk through a problem - I can't tell you how much I value our friendship. You are formidable and brilliant and I can't wait to see all the things you accomplish. GMaWiP members past and present, I am so proud to see you continuing to grow this community.

A very special thanks to Lisa Everett - I know I've said this before but the time and care you put into listening to and helping every member of the department is an incredible gift, and one I am very thankful for.

None of this would have been possible without the ever-present support of my family. For all the phone calls, for all the time you spent proofreading emails and telling me things were going to be okay, I can't possibly thank you enough.

Definitions

MHD	Magnetohydrodynamics - a fluid model description of plasma dynamics
CGL	Chew, Goldberger, and Low - a closure for the fluid equations that assumes that there is zero heat flux ($q = 0$)
DSA	Diffusive Shock Acceleration
PIC	Particle-In-Cell - a method for performing kinetic simulations that involves dividing the simulation domain into a set of smaller regions, or "cells", then computing the electric and magnetic fields on the domains of the cells, then updating the locations of the particles accordingly
VPIC	Vector Particle-In-Cell - a kinetic plasma simulation code developed at Los Alamos

Table of Contents

List of Figures

Chapter 1

Introduction and Motivation

How are superthermal power-law tails generated throughout the universe? What are the other heating mechanisms that have been used to explain this phenomenon?

Throughout the universe, nonthermal distributions of electrons and ions are commonly observed. This observation is not entirely surprising - space and astrophysical plasmas tend to have low collisionality, so it follows that the distributions of the constituent particles should deviate from Maxwellians, and reflect that fact that such plasmas are far from thermodynamic equilibrium. A feature of these distributions that is not necessarily expected is the presence of hot tails of the distribution that follow a power-law, *i.e.* $f \propto v^{-\gamma}$. Such distributions are commonly observed in cosmic rays as well as galaxy clusters, as shown in Fig. 1.1**(a)** and **(b)**. There are many other space and astrophysical systems that exhibit such power-law heating, a few examples of which, with a range of values given for their estimated power-law indices, can be seen in Fig. 1.1**(c)**, including interplanetary shocks, the Earth's bow shock and magnetosheath, and the solar wind. While we do not expect the distributions to be in thermal equilibrium, determining the physical mechanism which heats these particles and produces these specific, ubiquitous velocity signatures is still an open question, and is the question that is at the heart of this thesis.

This thesis details a mechanism called magnetic pumping, which uses magnetic fluctuations to heat the plasma and naturally generate superthermal power-law distributions. The most important result of this thesis is the extension of the magnetic pumping mechanism that incorporates the effects of trapped and passing particles. It is this extension that allows the heating of particles moving far faster than the wave speed, a regime where few other heating mechanisms are applicable. Because of the ubiquity of magnetic fluctuations, we think that magnetic pumping may play a role in heating particles across the universe. While there are a wide variety of systems where this heating mechanisms is applicable, for the purposes of this thesis we have focused on the heating of space plasmas, specifically the problems of anomalous heating of the solar wind, where one would expect the solar wind to cool adiabatically as it streams away from the Sun, but observations show that this is not the case, and heating of the plasma preceding the Earth's bow shock. These applications were chosen in part because of the relative abundance of *in situ* observational data on these superthermal power-law tails.

In the remainder of this introduction I will put magnetic pumping in context of the other heating mechanisms believed to be at work for collisionless space and astrophysical plasmas. Because this thesis focuses in particular on heating in the solar wind and directly prior to the Earth's bow shock, this section will focus in particular on mechanisms that are believed to have a strong role there.

1.1 Potential heating mechanisms

Understanding the transport of energy in these space and astrophysical systems is a complicated problem, involving competing processes of charged particles interacting with electric and magnetic fields. For these distributions which are far from equilibrium, we often discuss heating mechanisms as being either wave-particle or wave-wave interactions. Wave-particle refers to mechanisms where the dominant mode of energy transfer is in-between the waves and the particles, and wave-wave refers to those where the dominant mode of energy transfer is between the magnetic or electric field fluctuations. For the purposes of this thesis a more

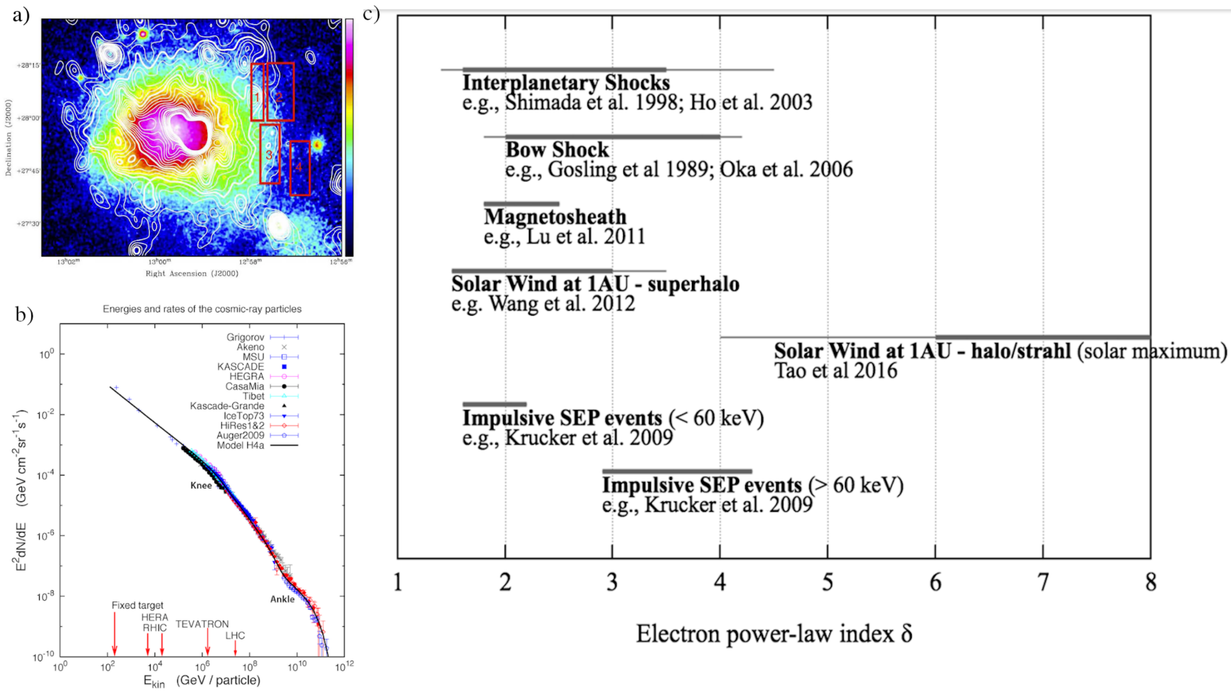

Figure 1.1: **(a)** Plot of the halo of the Coma cluster of galaxies - an example of galaxy clusters where hot, power-law tails ar observed. Here the x-ray emission is shown in color and the radio synchrotron emission shown in the contours. This figure is reproduced from Brown and Rudnick[1]. **(b)** Plot of the observed power-law of cosmic rays with data from a number of observations, with the plot reproduced from the IceCube Collaboration[2]. **(c)** Power-law indices for a number of observed electron distributions within the heliosphere. This plot was reproduced from Oka, *et al.* [3].

helpful organizing question to differentiate between these heating mechanisms is ‘at what scale does this heating mechanism inject energy into the plasma?’ This allows us to differentiate between heating mechanisms where energy is injected at a particular velocity scale and those that act on the entire distribution function. Two of the most common examples of heating mechanisms that inject energy at a particular scale are heating through the turbulent cascade, where energy travels from the largest scale fluctuations to progressively smaller fluctuations, until the particles are ultimately heated at the kinetic scale, and resonant wave-particle interactions, where only particles at a particular velocity are heated. Whereas a few common examples of non-resonant heating mechanisms are magnetic reconnection [4], stochastic acceleration, and Fermi-like heating processes.

The reason this is such a helpful question is that it is very difficult to reproduce the near-ubiquitous observations of power-law distributions of superthermal particles. However, much of the work on a possible explanation for heating in the solar wind centers on resonant processes as the primary heating mechanism, particularly resonant wave-particle interactions, where energy is provided by the turbulence associated with propagating waves [5, 6, 7, 8, 9, 10]. The best know examples of these resonant wave-particle interactions are the Landau and cyclotron resonances. In these models, particles are energized at the resonant velocities, where $vk\cos\Theta \simeq \omega$, with $\cos\Theta = \mathbf{v}\cdot\mathbf{k}/(vk)$, where v is the speed of the particle, ω is the frequency of the wave, and k is the wavelength. Particle energization is then limited to $v \leq \omega/(k\cos\Theta)$. Superthermal electrons then require energization by waves with large phase velocities, $v_p = \omega/k$, such as whistler waves [11]. However, in many systems, the energy available in whistler waves has been found to be insufficient to explain the observed level of electron energization. In a recent analysis using spacecraft data from the Magnetospheric Multiscale (MMS) mission it was found that while whistlers are effective for pitch angle scattering, the whistler bursts did not correlate well with electron energization [12]. Another such method commonly used to explain the observed heating is a subclass of wave-particle models developed for particles with $\cos\Theta \simeq 0$. In this case the energization schemes only apply to a limited fraction of the overall electron population. While the models of wave-particle interactions play a strong role in heating particles up to $v \simeq \omega/(k\cos\Theta)$, observations often require energization beyond this limit.

While it is difficult to reproduce these superthermal power-law tails with a set of resonant wave-particle interactions, such distributions are known to form in Fermi-like heating processes where the energy gains of individual particles are proportional to their initial energies. One such model which was able to provide an explanation for the observed power-law distribution is a compressional pumping mechanism proposed by Fisk and Gloeckler [13, 14]. In their model, particles are accelerated by random compressions driven by interplanetary wave turbulence. The theory explores diffusion due to spatial non-uniformities and provides a mechanism for redistributing particle energies to yield power-law distributions with the observed index of $\gamma \sim -5$. Critically, we note that this process is energy neutral and operates without a net transfer of energy from the driving turbulence to the particles. The model is derived from the Parker equation, and the lack of energy transfer is directly related to the fact that the distribution function, $f(v)$, is isotropic in velocity space. In contrast to this model, magnetic pumping includes the diffusion of anisotropic features that develop in velocity space. This difference is important because it allows energy to be transferred to the particles directly and efficiently from the turbulent fluctuations. This energy transfer means that magnetic pumping, in contrast to the model developed by Fisk and Gloeckler, will not just generate power-law distributions but also will heat the plasma.

1.2 Overview of the work presented in this thesis

The remainder of the thesis will detail work we have done investigating magnetic pumping. Chapter 2 will be devoted to a description of how magnetic pumping works physically and how the main results of this thesis fit into existing work. After that point, we will review the major results in detail. Chapter 3 will go through the results of work on the 1D magnetic pumping model, its verification using particle-in-cell (PIC) simulations, and its application to heating in the solar wind, including its extension to include an approximation of the effects of spatial variation along a flux tube. In Chapter 4 we will detail the most important elements of the 2D magnetic pumping model and compare it to spacecraft observations. Chapter 5 will go through the derivation of the analytic model used in Chapter 4. Finally, in Chapter 6 we will review the conclusions of this work as well as some possibilities for future extensions of this work.

Chapter 2

Background and Connection to Other Mechanisms

What is magnetic pumping? How do our results fit in with existing work?

In this chapter we will start with an overview of the fundamental physics of magnetic pumping. We begin by discussing adiabatic invariants and how the plasma responds to a changing magnetic field in an infinite, spatially-uniform flux tube, then use this to obtain physical intuition for how magnetic pumping works. The ultimate goal of this portion of the chapter is both to gain a physical intuition for how magnetic pumping works and also to understand the parameters that will determine when the mechanism is most effective, to better recognize when it will play an important role in the energy transfer in a plasma.

Following this discussion of the magnetic pumping mechanism in a uniform flux tube, we discuss how the introduction of spatial variation along the flux tube changes the heating and energy transfer due to magnetic pumping. To the best of our knowledge the work in this thesis is the first time the effects of spatial variation have been included in a model of magnetic pumping. The goal the remainder of the chapter is to connect our assumptions and results to existing work. The structure of the remaining two sections of this chapter parallels the discussion of the main results in the remainder of the thesis. We start with an approximation of the effects of spatial variation. To do this we incorporate the effects of thermal streaming, which has been used to capture kinetic effects in fluid closure models. This approximation is followed by a more rigorous treatment of spatial variation along a flux tube. For this more rigorous treatment we use a derivation very similar to quasilinear theory, a framework commonly used to find the energization from wave-particle interactions. While very similar in practice, our treatment violates some of the fundamental assumptions of quasilinear theory, so it can be better thought of as an extension of quasilinear theory. The main results and assumptions of the derivation are given in more detail in Chapter 4 and 5, but it is helpful to review the the fundamentals of quasilinear theory and how our treatment deviates from the standard version of quasilinear theory.

2.1 Physical Explanation of Magnetic Pumping

To understand how magnetic pumping works in a physical sense we start by considering the behavior of a plasma in an infinite, uniform flux tube, for which the magnetic moment, $\mu = mv_\perp^2/(2B)$, and the action, $J = \oint v_\parallel dl$, are conserved [1]. The parallel and perpendicular directions are defined with respect to the magnetic field. We consider an element of this flux tube of length L and radius r. From the form of $\mu = mv_\perp^2/(2B) \sim T_\perp/B$ we can see that the perpendicular temperature is positively correlated with the magnetic field, $T_\perp \sim \mu B$, so if the magnetic field increases $T_\perp$ will increase as well. For a uniform flux tube we know that $J = \oint v_\parallel dl = v_\parallel L$, so we can use this expression to find that the parallel temperature is positively correlated with the length of the flux tube element, $T_\parallel \propto (J/L)^2$. From this equation it is not immediately clear how a changing magnetic field will change the temperature in the parallel direction. However, using the fact that the number of particles, $N = n(\pi r^2)L$, where n is the density, and the magnetic flux, $\phi = B(\pi r^2)$ are conserved, we can find a relationship for how the length of the flux tube element varies with a changing magnetic field.

[1] This analysis can easily be generalized to a relativistic system using the appropriate replacements for the relativistic momenta and fields.

By taking the ratio of the two conserved quantities we find $N/\phi = nL/B$, so $L \propto B/n$, and when this length is increased the parallel temperature will decrease.

It is worth noting at this point that through our assumptions of an infinite, uniform flux tube that undergoes motion such that the magnetic moment and action are conserved we recover the Chew, Goldberger, and Low (CGL) [15] pressure relationship, namely

$$p_{\parallel} \propto n^3/B^2, \qquad p_{\perp} \propto nB \qquad . \tag{2.1}$$

The CGL limit is a closure scheme for the moments of the fluid equation for well-magnetized particles in a collisionless plasma. This closure assumes that there is no heat flux in the system ($q = 0$), which is an assumption that should be applicable to an infinite, uniform, double-adiabatic flux tube.

Now that we have these relationships for $T_{\parallel}$ and $T_{\perp}$ we can examine how the changing magnetic field will affect the distribution function of the plasma. This process is detailed in Fig. 2.1. If the magnetic field is increased the plasma will be heated in the perpendicular direction and cooled in the parallel direction, with the reverse occurring if we decrease the magnetic field. If we return to our original magnetic field amplitude, we will recover our original distribution, and over the course of the cycle we will get no net heating.

However, we can consider the case where we increase the magnetic field as before, but before we decrease it we apply some sort of isotropization mechanism - that could be Coulomb collisions, thermal streaming, or scattering off of waves, as shown in Fig. 2.2. This will redistribute f over the phase-space elements, so that when the magnetic field decreases we will not recover our initial distribution function, and we'll get net work from the positive work done by the $p_{\perp}\nabla_{\perp} \cdot v$ term averaged over the course of a cycle. This is the basic, physical mechanism of magnetic pumping.

The amount of work done by magnetic pumping depends on a number of factors. From Figs. 2.1 and 2.2 as well as our analysis for $p_{\perp}$ above, we can see that the amount that the distribution function is heated in the perpendicular direction when the magnetic field is

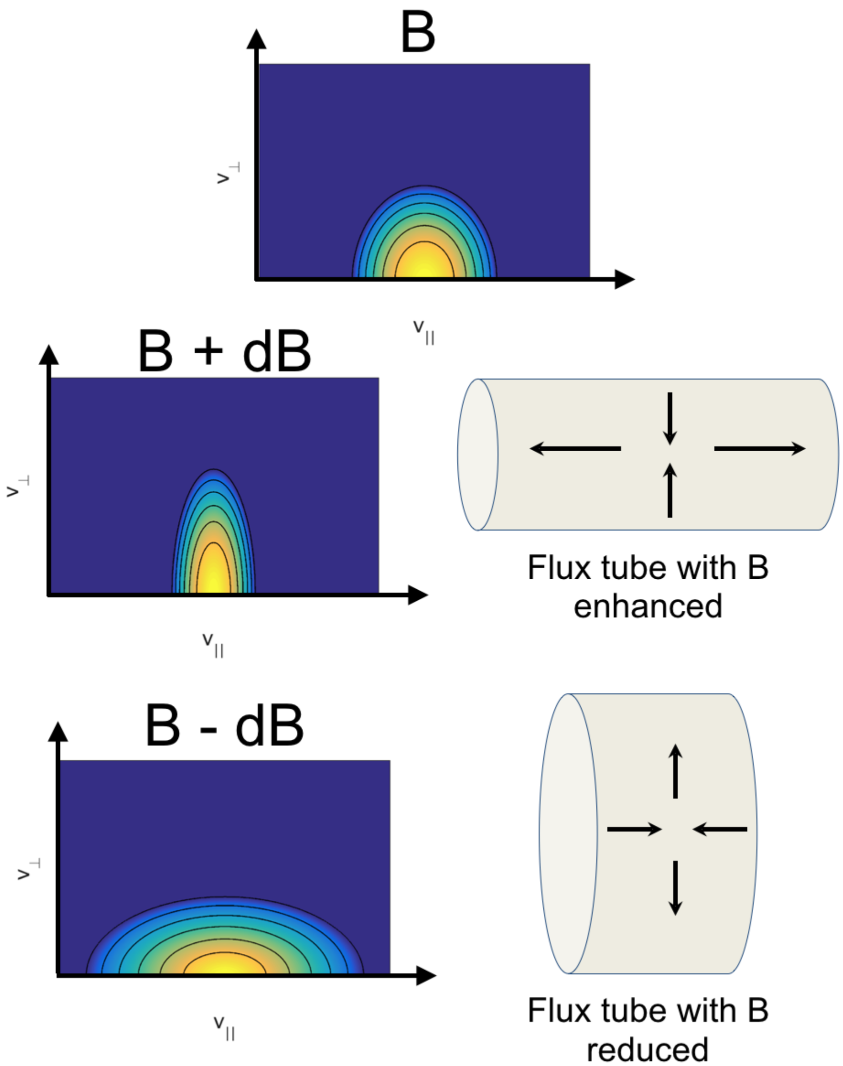

Figure 2.1: This cartoon demonstrates how the velocity distribution function and the magnetic flux tube deforms under the effects of a changing magnetic field. The initial distribution function is shown at the top of the figure. The second row shows the effects of increasing the magnetic field. As discussed in the text, the distribution function is heated in the perpendicular direction and cooled in the parallel direction. The flux tube increases in length and decreases in area. The third row shows the results for a decrease in magnetic field, where the effects are the opposite as in the second row.

increased is dependent on how much the magnetic field is increased, *i.e.* $\Delta B/B_0$. When the distribution is redistributed over the phase-space elements a higher amount of initial heating, or a larger magnetic field perturbation, will lead to more work over the course of the cycle.

If we examine the plot of the distribution function as a function of energy, $\log_{10} f(E)$

in Fig. 2.2, we can glean further insight into the pumping mechanisms. The most obvious result from this plot is that the overall amount of heating from magnetic pumping is directly dependent on how many pumps the system undergoes - with more pumps corresponding to a higher overall amount of energy transferred to the particles from the fluctuations. However, we can see the suggestion of a more subtle aspect of magnetic pumping from this plot as well. Specifically, we can see that the amount of heating is dependent on the particles' initial energy. If the amount of heating were independent of the initial energy, the shape of the distribution function would not change and the whole distribution function would instead be shifted to a higher energy. Instead, we see a decrease of the number of particles at low energy and a commensurate increase of the particles at high energies, so the amount of heating per particle is proportional to the particle's initial energy.

An important physical aspect of magnetic pumping, and the way in which it differs from other models[2], is in the role of pressure anisotropy in relation to the fluctuating magnetic field. In the case with no scattering the pressure anisotropy and magnetic field fluctuate in sync and there is no net work. We can think of collisions as pushing the pressure anisotropy out of phase with the magnetic field, where this phase difference between the fluctuating magnetic field and the pressure anisotropy accounts for the net work over the course of the cycle.

To get a better sense for what is happening physically we can consider a magnetosonic wave. Assuming a background magnetic field, $\mathbf{B_0} = B_0\hat{z}$, and linear perturbations of the form $\exp[-i\omega t + i\mathbf{k}\cdot\mathbf{r}]$, with $\mathbf{E_1}+\mathbf{v_1}\times\mathbf{B_0} = 0$ we can rewrite Faraday's law, $\nabla\times\mathbf{E_1} = -(\partial\mathbf{B_1}/\partial t)$, as

$$\frac{\partial\mathbf{B_1}}{\partial t} = \nabla\times(\mathbf{v_1}\times\mathbf{B_0}) \quad , \tag{2.2}$$

from which we can obtain the expression

$$B_{1z} = \frac{k_\perp B_0 v_{1x}}{\omega} \quad . \tag{2.3}$$

[2]Although not all models, notably [16] and [17]

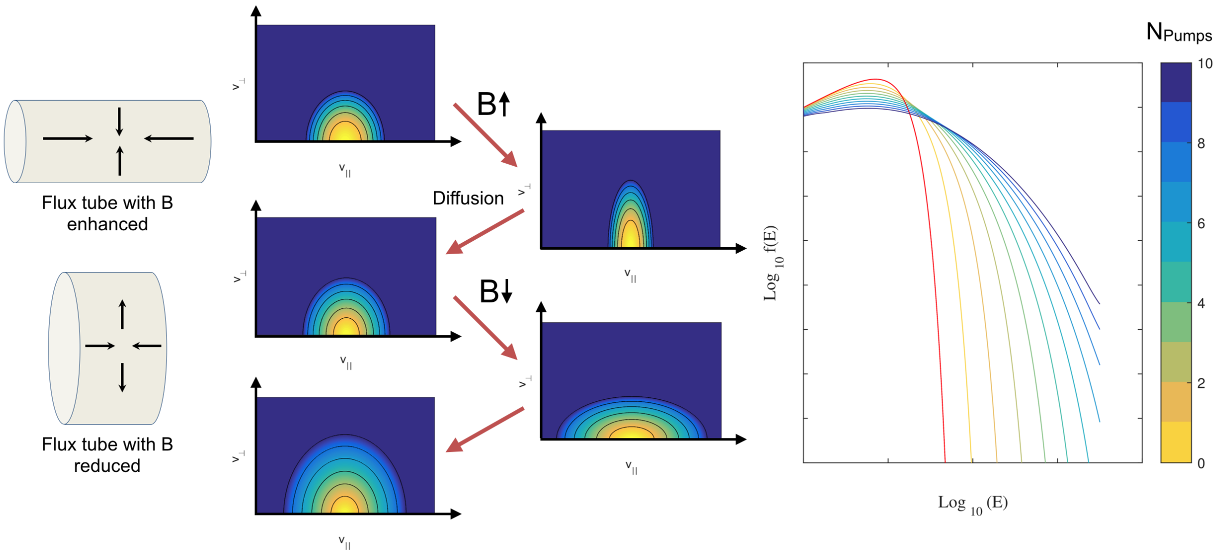

Figure 2.2: An illustration of the principles underlying magnetic pumping. The flux tubes on the left hand side of the plot illustrate the deformations that occur in the flux tube as the magnetic field, B, is enhanced (top) and reduced (bottom) in order to conserve the magnetic flux, $\Phi = B\pi r^2$, and the total number of particles, $N = \pi r^2 nL$. The distribution functions in the center correspond to the steps in the cartoon version of the magnetic pumping cycle. The first distribution on the top left corresponds to the initial distribution function, the second corresponds to the distribution function after the magnetic field is increased, the third after a scattering operator is applied, the fourth when the magnetic field is decreased, and the final distribution is the result after the magnetic field is returned to its initial value. This final distribution function then becomes the initial distribution function for the next cycle. The results for the pitch-angle-averaged distribution function as a function of energy, $\log_{10} f(E)$, over the course of ten pumps is shown in the plot on the far right. The initial distribution function is denoted in red.

For a standing fast magnetosonic wave we find that the velocity and magnetic field vary as

$$v_x = v_{1x}\left(e^{-i\omega t+ik_\perp x} + e^{-i\omega t-ik_\perp x}\right) \tag{2.4}$$

$$B_z = B_0 + B_{1z}\left(e^{-i\omega t+ik_\perp x} - e^{-i\omega t-ik_\perp x}\right) \tag{2.5}$$

Here it is important to note that the sign of B_{1z} depends on $k_\perp$, explaining the relative phase difference between v_x and B_z. This phase difference can be seen more clearly by taking the

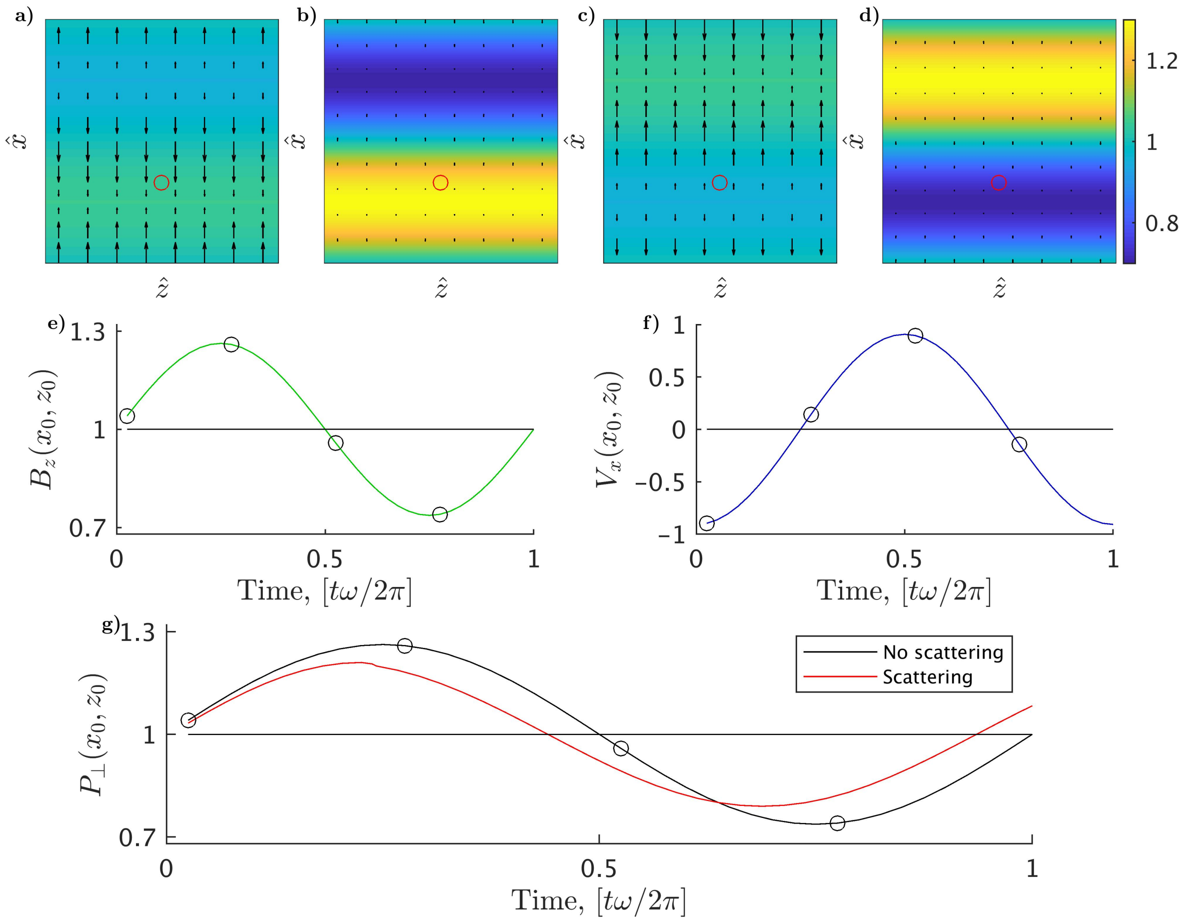

Figure 2.3: **(a-d)** These plots show the direction and magnitude of the perpendicular velocity, where $v_\perp = v_x$, in arrows overlaid on the overall magnetic field in the z direction for various points along the cycle. Points slightly off the maximum and minimum were chosen to more easily ascertain which point in the cycle the plot corresponded to. **(e)** shows the magnetic field in the z direction and **(f)** shows the velocity in the x direction. Both of these values were taken at the point marked with the red circle in plots (a-d). (g) shows both the expected perpendicular pressure for the the magnetosonic wave in black, as well as a cartoon of how the perpendicular pressure would change if there was some sort of isotropizing process present in red.

real part of this result,

$$v_x = 2v_{1x}\cos(\omega t)\cos(k_x x) \tag{2.6}$$

$$B_z = B_0 + 2B_{1z}\sin(\omega t)\sin(k_x x) \quad . \tag{2.7}$$

As we can see, the flow is perpendicular to the background magnetic field, as shown in Fig. 2.3. We start with an unperturbed magnetic field, and the appropriate velocity perturbation for a compressional Alfvén wave with alternating areas of rarefaction and compression. In the areas of compression, the velocity perturbation, v_1, will compress the magnetic field until the magnetic field can be compressed no more. At this point of maximum compression, the velocity perturbation will go to zero. After that point the velocity perturbation will reverse its previous direction, and the regions of compression will become regions of rarefaction until the adjacent regions of compression can be compressed no more, at which point the cycle will again reverse.

From this description it is clear that the magnetic field and the perpendicular velocity perturbation are out of phase by a factor of $\pi/2$. From the CGL pressure relations we know that the perpendicular pressure will oscillate with the magnetic field. So to obtain the amount of expected heating we can integrate our energization term over the course of a pump cycle, *i.e.*

$$\int_0^{2\pi} p_\perp \nabla \cdot v_\perp dt \propto \int_0^{2\pi} \sin(t)\cos(t)dt = 0 \quad . \tag{2.8}$$

This makes sense if we recall the physical explanation of magnetic pumping, where if there is no scattering, there is no heating.

If we add in scattering, however, as the pressure increases, more and more of the perpendicular pressure will be scattered away so the pressure will start decreasing faster than it would in the same system without scattering. This will cause a phase difference between the velocity perturbation and the pressure, which we can see from our energization term will lead to a net amount of heating,

$$\int_0^{2\pi} p_\perp \nabla \cdot v_\perp dt \propto \int_0^{2\pi} \sin(x)\cos(x+\phi)dx = \pi \sin(\phi) \tag{2.9}$$

that is dependent on the amount of scattering. From this form we can see that with no phase difference, or no scattering, there is no heating. Similarly, in the limit where there is an infinite amount of scattering the distribution function will always be a Maxwellian, the pressure anisotropy will approach zero, and there will be no heating.

The previous discussion is a very basic description of how magnetic pumping works, but it does encapsulate some of the key elements of magnetic pumping, specifically that

1. The amount of heating is dependent on the strength of the magnetic perturbation ($\Delta B/B_0$).
2. The amount of heating is dependent on the amount of scattering.
3. The amount of heating is dependent on the number of pumps.
4. The amount of heating per particle is proportional to the particle's initial energy, leading to power-law distributions.

The last point is one of the most critical, as it is this $\Delta v \sim v$ dependence in the heating that naturally generates the power-law distributions. This type of heating is typically called a Fermi process, after Fermi's 1949 theory for the origin of cosmic rays[18]. The idea was that cosmic rays would have random reflections with interstellar magnetic clouds. Energy is gained during a head-on encounter with a cloud, and lost during an encounter with a trailing cloud so if each type of collision were equally likely, there would be no net energization of the plasma. However, it turns out that head-on collisions are more likely than trailing collisions. For relativistic particles we get an average increase of energy per collision that is second order in velocity, $\Delta\mathcal{E}/\mathcal{E} = 2(u/c)^2$, and when we calculate the spectrum using the diffusion-loss equation we get that the number of particles as a function of energy is a power-law distribution, $N(\mathcal{E}) \propto \mathcal{E}^{-x}$, where x is dependent on the time between encounters, or collisions, and the time that the cosmic ray spent in the system. The energy gains in this model are second order $\mathcal{O}(v^2/c^2)$, but if the cosmic rays were to be trapped between two clouds that were approaching each other, then every encounter would result in an increase of energy and the acceleration mechanism would be much more efficient, becoming a first order process, $\mathcal{O}(v/c)$. This very behavior is seen in diffusive shock acceleration (DSA), where particles bounce off magnetic fluctuations upstream and downstream of the shock front, leading to multiple shock crossings and naturally generating power laws. While a different physical mechanism, because of the first-order velocity dependence of the energization and the power-law generation, we refer to magnetic pumping as a first-order Fermi process.

Magnetic pumping is not a newly discovered heating mechanism - it was first proposed by Hannes Alfvén in 1950 as a possible way to explain observations of cosmic rays [19]. The idea was further investigated as a possible heating mechanism for fusion plasmas[20, 21]. It was abandoned in favor of other mechanisms, such as radio-frequency heating, that yielded better heating rates. To the best of our knowledge, our work is the first time it has been applied to explain heating in the solar wind, although it has been discussed as a possibility in other space and astrophysical plasmas[22].

Historically speaking, one of the reasons magnetic pumping did not get more attention is because of the low overall heating rate. From our basic physical model we can see why this might be an issue. We know that the amount of heating is dependent on the amount of scattering. From our initial description of magnetic pumping we know that in the limit of no scattering there's no heating and most space and astrophysical systems have extremely low levels of Coulomb collisions. For example, during a typical transit from the Sun to the Earth a particle will undergo on average one collision. For fusion systems its implementation was hindered by the difficulty of squeezing the toroidal field in tokamaks. However, in a field-reversed configuration (FRC) there is no toroidal field, so it is feasible to perturb the plasma enough to obtain reasonable levels of magnetic pumping. This fact, combined with the built-in scattering in the non-adiabatic orbits, make magnetic pumping a candidate for heating fusion plasmas in FRCs [23].

2.2 Importance of spatial variation

The major contribution of the work detailed in this thesis, beyond applying the mechanism to novel space and astrophysical systems, is in adding in the effects of spatial variation along the flux tube into the magnetic pumping mechanism. We have used two different methods of incorporating the spatial variation into the magnetic pumping model. The first is a more approximate version of incorporating some elements of spatial variation along a flux tube, specifically the effects of thermal streaming. Everything we've discussed up to this point has been for an infinite, uniform flux tube. If there were spatial variation along this tube then by definition there would be areas where $\Delta B/B_0$ was higher, and creating localized areas where the pressure anisotropy would be higher. The particles will stream away from these regions at their speed, v, isotropizing the plasma at a much faster rate than the level of isotropization from Coulomb collisions, because for parameters relevant to collisionless space plasmas the rate of isotropization from Coulomb collisions is incredibly low. For this approximate version of incorporating 2D physics into the 1D model, we use the same 1D model, but create a new effective scattering rate that encapsulates the rate of isotropization from thermal streaming, $\nu_{\text{eff}} = v/L$, where L is the spatial extent of the perturbation.

Before we review how this connects to existing research it is helpful to review how to capture the behavior of a collisionless, well-magnetized plasma in different regimes. We've mentioned the CGL limit, where for well-magnetized particles in a collisionless plasma we obtain the relationship for how the parallel and perpendicular pressures evolve when the heat flux vanishes ($q = 0$). In general, however, we know that plasmas have finite heat fluxes. In a collisional plasma the parallel heat flux is well modeled by $\mathbf{q}_{\parallel} = -\kappa_{\parallel}\nabla_{\parallel}T$ [24]. Taken in the limit of collisionless plasmas, this scaling implies an infinitely high heat conduction, which leads to the Boltzmann limit where the plasma is isothermal along field lines.

The validity of these two limits rests on how fast the fluctuations vary compared to the thermal speed of the particles, or in other words how the time scale of the fluctuations compare to the transit time of a particle through the perturbation, $\omega/k_{\parallel}$ compared to v_{th}. The CGL closure is valid in the limit where the phase speed of the fluctuations is much greater than the thermal speed of the particles, $\omega/k_{\parallel} \gg v_{\text{th}}$. In this limit the scale of the perturbation, $1/k_{\parallel}$ is much greater than the distance a particle moving at the thermal speed can travel during the time of a fluctuation, v_{th}/ω, so the particle experiences the full temporal evolution of the fluctuation with relatively little spatial variation, the exact circumstances that one would experience in a uniform flux tube. The Boltzmann limit occurs under the opposite circumstances, where $\omega/k_{\parallel} \ll v_{\rm th}$. In this limit the particles are moving so fast relative to the speed of the fluctuations that phase mixing gets rid of all the anisotropy and the plasma becomes isothermal along the field lines.

However, in real systems we know that heat fluxes are finite, usually neither zero nor infinite, and the temporal scale of fluctuations compared to the transit time of a particle is often in neither of those two extreme limits. To fully capture the behavior of the plasma in realistic circumstances we can use the kinetic equation. However, both for the computational benefits, as well as the additional insight into the underlying physics it is useful to find a set of a finite number of velocity moments of the kinetic equation that captures the behavior of the plasma.

A well-known approach, and the one that is most relevant to our extension of the 1D pumping model, is the Landau closure originally developed by Hammett and Perkins [25] and extended by Snyder et al., Ng et al., and others [26, 27]. These closures capture the effects of phase mixing as well as Landau damping. By using these closures we recover the the CGL limit for perturbations with $\omega/(k_{\parallel}v_{\rm th}) \gg 1$, and the Boltzmann limit when $\omega/(k_{\parallel}v_{\rm th}) \ll 1$, and a good approximation of the plasma behavior in the intermediate regime. These closures use a heat flux of the form

$$\tilde{q}_k = -n_0\chi_1\frac{\sqrt{2}v_{\rm th}}{k}ik\tilde{T}_k \qquad , \tag{2.10}$$

where $\tilde{T} = (\tilde{p} - T_0\tilde{n})/n_0$ is the perturbed temperature and χ_1 is a dimensionless coefficient. This heat flux closure is equivalent to our incorporation of thermal streaming. The heat flux closure form implies that the heat flux goes as the temperature of the plasma over the size of the perturbation, $\tilde{T}_k k$, which accounts for the effects of thermal streaming.

Something neglected in these closure methods are the effects of trapped particles, which can occur in the spatial variations along the flux tube. We would expect these trapped and passing particles to play a strong role in the evolution of the plasma. An example of the importance of including trapping can be found in magnetic reconnection literature. As described in Lê *et al.* [28], as flux tubes travel into the magnetic reconnection region, the magnetic field decreases, and they deform such that the electron population splits into a population of trapped particles and a population of passing particles. This closure is based on a solution of the drift kinetic equation in the limit of a fast electron transit time [28, 29, 30]. The model transitions between the Boltzmann response in the limit of small values of n/B where the plasma is dominated by passing electrons to the CGL scalings in the limit of large n/B where a majority of the electrons are trapped. It is important to note that this analysis is performed for a monotonically changing magnetic field. When instead of a monotonically changing magnetic field a fluctuating magnetic field in combination with pitch-angle mixing is considered, there is additional physics that comes into play, specifically the effects of magnetic pumping.

2.3 Relationship to quasilinear theory

One of the most significant results of this thesis comes when we include the effects of magnetic trapping. The extension of the 1D magnetic pumping model to include the effects of thermal streaming works well for the ions, but for the electrons the power-law portion of the distribution function cuts off before it would even be detectable in spacecraft measurements. When we include the fact that magnetic fluctuations can trap superthermal particles it turns out we can heat particles moving far faster than the wave speed, a regime where few heating mechanisms are effective.

To appreciate how the inclusion of magnetic trapping fits into existing research it is important to understand how magnetic pumping relates to heating through resonant heating mechanisms, in particular Landau and transit-time damping. In our magnetic pumping analysis the heating efficiency is derived by considering a standing wave for which wave-particle resonances are unimportant. Thus, the resultant heating does not involve a specific resonant velocity, as in Landau or transit-time damping where only particles with $v_\parallel \simeq \omega/k_\parallel$

are involved in the heating. With the standing wave being comprised of two oppositely propagating compressional waves, the heating can be interpreted as a nonlinear interaction between these two waves.

To better understand the derivation of magnetic pumping in 1D and how the 2D model is a significant departure from existing work, it is helpful to review quasilinear theory and Landau damping. When looking at oscillatory or damped modes in the plasma, to describe the evolution of the plasma and the transfer of the energy it is often (although not always) sufficient to use the linear approximation, where the perturbations are treated as extremely small when compared to the unperturbed equilibrium distribution, allowing us to express the evolution of the plasma in terms of a set of analytically tractable, homogeneous linear equations. Because the perturbations are assumed to be so small when compared to the equilibrium distribution, we can consider one wave at a time and ignore the nonlinear effects that come from waves interacting with each other. However, for unstable, or growing, modes this linear behavior must eventually break down as the amplitude of the mode cannot exhibit the predicted exponential growth indefinitely and it becomes important to take into account the effects of these nonlinear interactions.

Quasilinear theory is a convenient mathematical framework to describe the energy transfer and evolution in plasmas in the regime where waves change the background distribution function, but the departures from equilibrium are small enough that we assume that the background distribution changes slowly relative to the timescale of the fluctuations. The most common usage is in explaining the energy transfer and evolution in wave-particle interactions [3], where energy is transferred from the fluctuations in the plasma to particles moving at a particular, resonant velocity, but it has also been used in the derivation of the small-scale

[3] As mentioned in the introduction, the other commonly discussed channels of nonlinear energy transfer are wave-wave interactions, where the dominant mode of energy transfer is between fluctuations, as opposed to between the fluctuations and the particles. If the wave amplitudes are large enough and the interactions between different waves occur on a timescale on the order of or shorter than the constituent wave periods, then we have entered the regime of strong turbulence [31]. Two classic examples of strong turbulence are the Kolmogoroff treatment of homogeneous, isotropic fluid turbulence and the Goldreich-Sridhar theory of small-scale Alfvén wave turbulence. Both of these energy channels, wave-wave interactions and strong turbulence are outside of the scope of this thesis.

dynamo field evolution[32], and in our derivation of 1D magnetic pumping.

Fundamental to quasilinear theory are two key assumptions

1. The amplitude of perturbations in the plasma are small compared to the unperturbed plasma equilibrium ($\delta B \ll B_0$ and $\delta f \ll f_0$).
2. A broad enough spectrum of waves is assumed such that phase-sensitive effects will disappear.

Our work represents two major, related, departures from the standard quasilinear treatment. First, while we follow the blueprint of quasilinear theory we explicitly disregard one of the fundamental assumptions of quasilinear theory - that the distribution function will not generate significant structure in phase space. In fact, the phase space structure that corresponds to the trapped particle dynamics is integral to obtaining the heating and power-law distribution generation in magnetic pumping for electrons. The reason we are able to do this is the second major addition to the standard quasilinear approach - working specifically in the limit that the bounce time, τ_b, is much smaller than the time scales associated with the waves. In this limit, the particle orbits are well-described by the magnetic moment, μ, and the total energy, $U = \mathcal{E} - e\phi$, as well as the parallel action variable $J = \oint v_{\|} dl$. We also only consider particles moving with energies high enough that the $v \times B$ term dominates the Lorentz force, allowing us to use μ and $\mathcal{E}$ to characterize the particle orbits. The multiple time-scale method tells us that the distributions must be constant along these orbits. This allows us to integrate along the full “perturbed" orbits, as opposed to the unperturbed orbits as is usually done in quasilinear theory, and include the effects of trapped and passing particles in our analysis.

To see in more detail how our work compares to quasilinear theory it is helpful to go through the quasilinear approach to Landau and transit-time damping and discuss how this compares to our magnetic pumping analysis. The standard derivation of Landau damping starts with the 1D kinetic equation

$$\frac{\partial f}{\partial t} + v\frac{\partial f}{\partial x} - \frac{eE}{m}\frac{\partial f}{\partial v} = 0 \tag{2.11}$$

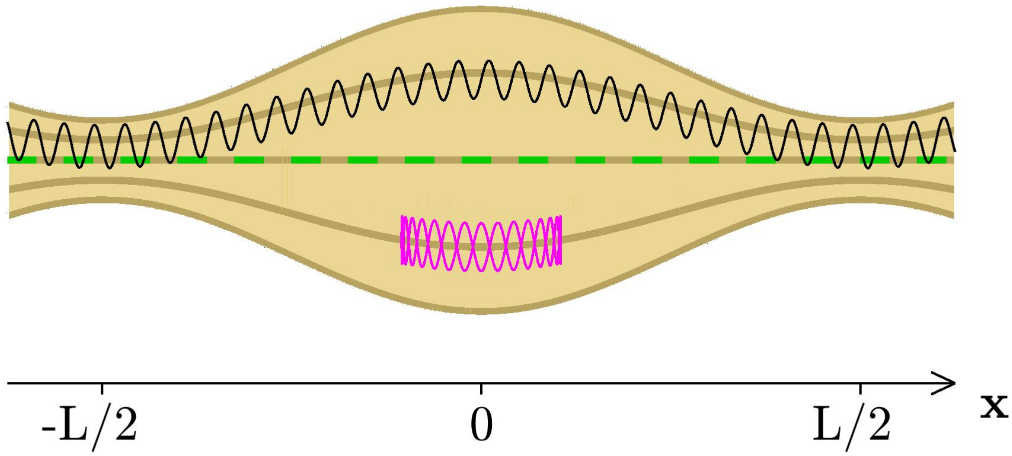

Figure 2.4: Cartoon of a flux tube and a set of trapped (magenta) and passing (black) orbits. The black and magenta orbits are both perturbed orbits, while the green dashed line denotes the field line of the unperturbed orbit used in earlier analyses.

which is linearized by writing the distribution function and electric field as

$$f(x, v, t) = f_0(v) + f_1(v) \exp(-i\omega t + ikx) \tag{2.12}$$

$$E(x, t) = E \exp(-i\omega t + ikx) \tag{2.13}$$

where f_1 and E are small enough that second order cross terms are neglected. When we input these linearized version of $f(x, v, t)$ and $E(x, t)$ into Eq. 2.11 and solve for f_1 we can obtain the expression

$$f_1(v) = \frac{ieE}{m} \frac{\partial f_0 / \partial v}{\omega - kv} \quad . \tag{2.14}$$

Here we can see that the perturbed portion of the distribution function is proportional to some drive term times the velocity gradient of the background distribution function, $f_1 \propto (Drive) * (\partial f_0 / \partial v)$, which is the form we will find for our magnetic pumping analysis in Chapters 4 and 5, with the primary difference being that our drive term is different.

At this point, the standard quasilinear method makes the assumption that there is some spectrum of waves present such that the microstructure of the particle orbits is destroyed, and the phase space structure in the distribution function is destroyed, allowing the use of zeroth order trajectories. As mentioned before, we do not make this assumption in our analysis.

Returning to the 1D Landau damping derivation, we can take Eq. 2.11, with our linearized distribution function and electric field and average over a period we can obtain the equation

$$\frac{\partial f_0}{\partial t} = \frac{e}{m}\left\langle E\frac{\partial f_1}{\partial v}\right\rangle \quad . \tag{2.15}$$

where $\langle ... \rangle$ is the time average over the course of a period and many wavelengths[4]. Only terms in E and f_1 with the same k value will have non-zero contributions after the time averaging, because all other terms will be oscillating and beat together at a finite frequency, and will vanish when integrated over a given period.

We can use Eqs. 2.14 and 2.15 to find the evolution of the background distribution plasma

$$\frac{\partial f_0}{\partial t} = -\frac{e^2}{2m}\frac{\partial}{\partial v}\left[\mathrm{Im}\left(\sum_k |E_k|^2 \frac{1}{\omega_k - kv}\right)\frac{\partial f_0}{\partial v}\right] \quad . \tag{2.16}$$

This is the same process that we use to find the expression for the velocity diffusion from magnetic pumping. Our equation for evolution of the background plasma that we obtain also has the form $\partial f_0/\partial t \propto (\partial/\partial v)(\langle (Drive)^2\rangle\,(\partial f_0/\partial v))$, although, again, our drive term is different.

However, all of this analysis has been for Landau damping, where energy is transferred from the fluctuating electric field to the plasma. It is well known that propagating magnetosonic

[4]. We note that we can recover the field-particle correlation detailed in the paper by Klein and Howes [33] by multiplying Eq. 2.11 by $mv^2/2$ to obtain an equation for the evolution of the phase-space energy density, $w = mv^2 f$,

$$\frac{\partial w}{\partial t} = -\frac{mv^3}{2}\frac{\partial f_1}{\partial x} - \frac{ev^2}{2}\frac{\partial f_0}{\partial v}E(x,t) - \frac{ev^2}{2}\frac{\partial f_1}{\partial v}E(x,t).$$

Using the same method as was just described in the text, this equation can be averaged over the fluctuation parts of the distribution function to obtain an equation for the transfer of energy in phase-space as a function of time

$$\frac{\partial w}{\partial t} = \left\langle \frac{ev^2}{2}\frac{\partial f_1}{\partial v}\right\rangle \quad .$$

waves are subject to transit-time damping, and Stix [34] showed that transit-time damping is equivalent to Landau damping. In particular, Stix noted the similarity between the guiding-center equations of motion for a particle in an electric field and that in a magnetic field

$$m\frac{dv}{dt} = q\mathbf{E} \tag{2.17}$$

$$m\frac{\partial v_\parallel}{\partial t} = -\mu\hat{b}\cdot\nabla\left|\mathbf{B}\right|. \tag{2.18}$$

Given the similarities of the equations of motion we can see that to derive f_1 or $\tilde{n}$ for transit-time damping, all we have to do is replace e with μ and $\mathbf{E} = \nabla\phi$ with $\hat{b}\cdot\nabla\left|\mathbf{B}\right|$. This gives us the equations

$$f_1 = \frac{i\mu\left|\mathbf{B}\right|}{m}\frac{\partial f_0/\partial v-\parallel}{\omega - kv-\parallel} \tag{2.19}$$

$$\tilde{n} = \frac{i\mu\left|\mathbf{B}\right|}{m}\left(\frac{n}{kv_{th}^2} - i\pi\left.\frac{\partial f_0}{\partial v_\parallel}\right|_{v_\parallel=\omega/k}\right) \tag{2.20}$$

In the above example of transit-time damping Eq. 2.20 is used to obtain the dispersion relation and damping rate of the magnetosonic wave. The result for the perturbed distribution f_1 may then be applied in a quasilinear diffusion analysis (as in Eq. 2.15) to obtained a diffusion equation for the back ground distribution (leading to diffusion and heating around the resonance velocity $v_\parallel = \omega/k$), at a level that is consistent with the damping rate.

Meanwhile, in the present analysis of magnetic pumping we assume a standing magnetic perturbation caused by some wave activity, and carry out an analysis similar to that of quasi linear diffusion in Eq. 2.15. This analysis reveals heating terms not included in Landau damping. Thus, our present work is not concerned with the dispersion relation of the involved waves, although, our derived heating could easily be translated into additional damping for, say, a standing magnetosonic wave.

Chapter 3

1D Model

How does the 1D magnetic pumping model, and its extension to include thermal streaming, work? How can it be used to explain heating in the solar wind?

The results in this chapter will focus on superthermal particles heated by magnetic pumping in the solar wind. The majority of the work presented is this chapter has been published in Lichko (2017) [35].

3.1 Introduction

One of the first hints that there was an outflowing streaming of charged particles from the Sun to the Earth occurred in 1859 when Richard Carrington and Richard Hodgson observed what we now know to be a solar flare, which was followed roughly 18 hours later by one of the largest recorded geomagnetic storms on record, known as the Carrington event[1]. Carrington believed there to be a connection between the two events, however, it was decades later, after work done by Birkeland, Lindemann, Chapman, and Biermann towards the existence of

[1]During the Carrington event, auroras were seen as far south as Colombia[36] and the light of the auroras in the northeastern United States were so bright that people could read newspaper print by their light. Telegraph systems failed throughout Europe and North America, some to spectacular effect. However, some telegraph operators were able to continue sending messages even after they had disconnected their power supplies[37].

'corpuscular radiation' coming from the Sun that the current picture of the solar wind was postulated by Eugene Parker in 1958.

Two developments that were critical to Parker's work were Biermann's work on the tails of comets and Chapman's work on the properties of a gas at the temperature of the solar corona. It had long been known that regardless of whether they are moving towards or away from the Sun the tails of comets are always pointed away from the Sun. Biermann suggested that there might be some sort of outflowing stream of particles coming from the Sun that would cause this phenomenon. Since the 1930s it had become clear that the base of the solar corona must be at an incredible temperature, roughly 10^6 degrees Kelvin. Chapman calculated that a gas at this temperature must be an incredible heat conductor. Using both these pieces of information, Parker showed that a static balance between the plasma pressure and the magnetic field led to unphysical solutions, and that there needed to be an supersonic stream of particles flowing outward from the Sun, which we call the solar wind.

The existence of the solar wind has been confirmed via spacecraft observations for many years now. However, despite this there are a number of open questions about the solar wind, many of which will be addressed by the Parker Solar Probe mission, which launched in August of 2018. One of the most well known open questions in solar physics is one we've already alluded to - the coronal heating problem. The surface of the sun is about 6000 K, but over the course of only a few tens to hundreds of km the temperature jumps to over one million degrees Kelvin, far faster than can be accounted for by diffusion alone. Determining the source of this heating is an important part of Parker Solar Probe's science mission, but even beyond this point there is a discrepancy in the observed and predicted temperatures. In the Parker spiral, as the plasma streams away from the Sun we would expect it to cool adiabatically. As we can see from Fig. 3.1, this is not what is observed. Understanding the additional heating mechanism that causes the plasma in the heliosphere outside of the corona to be so much hotter than expected is the question that will be at the center of this section.

As mentioned in the introduction, there has been a great deal of work towards determining the mechanism that is responsible for this additional heating. Most of the work on the subject

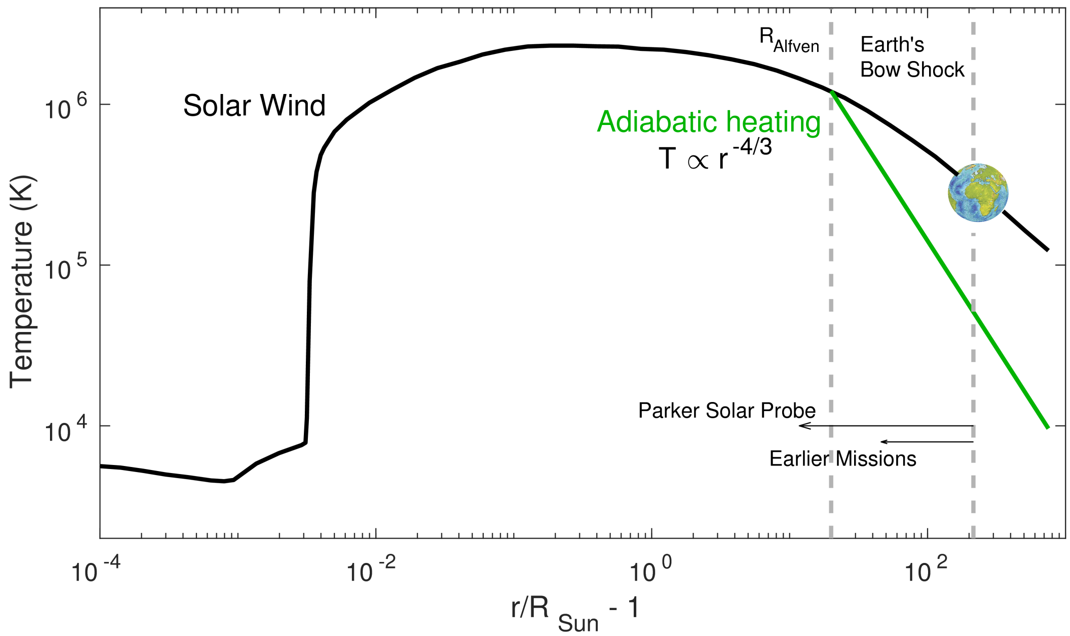

Figure 3.1: Plot of temperature as a function of the distance to the sun in solar radii, $R_{\rm Sun}$. Temperature is taken from a prediction of a model presented in Cranmer 2012 [38]. Earth cartoon is taken from [39].

has focused either on wave particle-interactions or the turbulent cascade. In both of these categories the plasma is energized at a particular velocity scale, unlike magnetic pumping which naturally generates superthermal power-law distributions like those observed in the solar wind. We believe magnetic pumping is a complementary heating mechanism to these wave-particle interactions and the turbulent cascade, but, as will be detailed in this chapter, for realistic solar wind parameters magnetic pumping can account for a substantial amount of the heating, suggesting that it is an important part of the heating process.

In this chapter we start by deriving the exact predictions for magnetic pumping in an infinite, uniform flux tube, then verify these predictions using VPIC, a particle-in-cell (PIC) code developed at Los Alamos National Laboratory. Once this model is derived and verified, we then apply magnetic pumping to the problem of anomalous heating in the solar wind. Because there are so few collisions in the solar wind, in order for magnetic pumping to be physically relevant, we had to include some 2D physics into our 1D model, specifically the effects of thermal streaming. For physically relevant solar wind parameters, we can see that for pessimistic parameters, magnetic pumping could account for a substantial amount of the heating in the solar wind.

3.2 Detailed derivation of the model

We next proceed to derive an analytic model to explain the energization and demonstrate that it matches the results from the kinetic simulations. To that end, we consider a periodic flux tube with length l and radius r. The plasma within the flux tube is assumed to remain uniform while r and l change slowly in time such that the magnetic moment $\mu = mv_\perp/(2B)$ of the particles is conserved. Furthermore, given the periodic boundary conditions, the action integral $J = \oint v_\parallel dl$ is also an adiabatic invariant provided that the length of the tube is not changed significantly during a typical particle transit.

For this system, our first aim is to obtain a reduced drift kinetic equation, $df/dt = 0$, where

$$\frac{d}{dt} = \frac{\partial}{\partial t} + \frac{dv_\perp^2}{dt}\frac{\partial}{\partial v_\perp^2} + \frac{dv_\parallel}{dt}\frac{\partial}{\partial v_\parallel}, \tag{3.1}$$

is the total time derivative along the particle trajectories. Note that given the assumption of a uniform plasma the convective spatial derivative term $(\mathbf{v}\cdot\nabla)$ vanishes.

Assuming $\mu \propto v_\perp/B$, $J \propto lv_\parallel$, $\Phi = B\pi r^2$, and $N = \pi r^2 nl$, we use the conservation of magnetic moment, action, and particle number to rewrite the above time derivative. For the simple geometry considered, the drift kinetic equation $df/dt = 0$ simplifies to

$$\frac{\partial f}{\partial t} + \frac{\dot{B}}{B}v_\perp^2\frac{\partial f}{\partial v_\perp^2} + \left(\frac{\dot{n}}{n} - \frac{\dot{B}}{B}\right)v_\parallel\frac{\partial f}{\partial v_\parallel} = 0 \quad . \tag{3.2}$$

In this limit without scattering, we note that evolution equations for $p_\parallel$ and $p_\perp$ are readily derived by calculating the $v_\parallel^2$ and $v_\perp^2$ moments of Eq. 3.2, which yields the CGL double adiabatic scaling laws

$$p_\parallel \propto n^3/B^2\,, \quad p_\perp \propto nB \quad . \tag{3.3}$$

In the following, we explore changes induced in f due to uniform perturbations of the flux tube in conjunction with steady pitch angle diffusion limiting the development of pressure anisotropy. Thus, we generalize our kinetic equation to include additional physical effects

$$\frac{df}{dt} = \nu \mathcal{L} f - c_1 f + c_2 f_{\rm ext} \quad , \tag{3.4}$$

where $\mathcal{L} = (\partial/\partial\zeta)(1-\zeta^2)(\partial/\partial\zeta)$ is the Lorentz scattering operator, $\zeta = v_\parallel/v$ is the cosine of the pitch angle, and ν is a typical frequency for the scattering processes. The constants c_1 and c_2 specify the rate of plasma losses and rate of incoming (external $f_{\rm ext}$) plasma, respectively.

For the analysis below it is convenient to change variables from $(v_\parallel, v_\perp)$ to (v, ζ). Eq. 3.4 then takes the form:

$$\frac{\partial f}{\partial t} + R\left(P_2(\zeta) v \frac{\partial f}{\partial v} + \frac{3}{2}\zeta(1-\zeta^2)\frac{\partial f}{\partial \zeta}\right) + \frac{\dot{n}}{3n} v \frac{\partial f}{\partial v} = \nu \mathcal{L} f - c_1 f + c_2 f_{\rm ext} \quad , \tag{3.5}$$

where $P_2(\zeta)$ is the second order Legendre Polynomial and $R = \frac{2}{3}\frac{\dot{n}}{n} - \frac{\dot{B}}{B}$. We note that $\frac{d}{dt}\log\left(\frac{p_\parallel}{p_\perp}\right) = \frac{d}{dt}\log\left(\frac{n^2}{B^3}\right) = 3R$, showing that R^3 is proportional to the rate at which the pressure anisotropy builds in the CGL system (the system with $\nu = c_1 = c_2 = 0$).

To evaluate the efficiency by which the plasma is energized in the above framework, we next consider periodic perturbations for the magnetic field and density. An approximate solution to Eq. 3.5 can be obtained by expanding f in a series of Legendre polynomials $f(v,\zeta,t) = \sum_j P_j(\zeta) f_j(v,t)$ where P_j is the jth order Legendre polynomial. The approach provides a set of coupled differential equations, which we solve numerically, and a first order approximation to the results. These two numerical solutions will then be compared to the results of the kinetic simulations.

We still consider the uniform and periodic flux tube but now with imposed sinusoidal temporal variations in density and magnetic field:

$$\frac{\dot{n}}{n} \;=\; \frac{\delta n}{n} i\omega e^{i\omega t} \;, \quad \frac{\dot{B}}{B} \;=\; \frac{\delta B}{B} i\omega e^{i(\omega t + \phi_B)} \;,$$

$$R = i\omega\delta R\, e^{i\omega t} \ , \ \delta R = \left|\frac{2}{3}\frac{\delta n}{n} - \frac{\delta B}{B} e^{i\phi_B}\right| \quad .$$

Our aim is again to obtain a solution to Eq. 3.5. Given the periodic variations of the drive, contrary to the analysis in [40] we do not need to impose an ordering involving ν, but only require that $\delta R \ll 1$. By inserting the above expansion in pitch angle into Eq. 3.5 and integrating over $\int_{-1}^{1} P_n(\zeta) d\zeta$, we obtain a set of coupled differential equations for an arbitrary order of Legendre polynomial:

$$\begin{aligned}
&\frac{\partial f_n}{\partial t} + n(n+1)\nu f_n + \frac{\dot{n}}{3n} v \frac{\partial f_n}{\partial v} \\
&\quad + \frac{3}{2} R \Bigg[\frac{n(n-1)}{(2n-3)(2n-1)} v \frac{\partial f_{n-2}}{\partial v} + \left(\frac{1}{2n+1} \left[\frac{(n+1)^2}{(2n+3)} + \frac{n^2}{(2n-1)} \right] - \frac{1}{3} \right) v \frac{\partial f_n}{\partial v} \\
&\qquad + \frac{(n+1)(n+2)}{(2n+3)(2n+5)} v \frac{\partial f_{n+2}}{\partial v} - \frac{n(n-1)(n-2)}{(2n-3)(2n-1)} f_{n-2} + \frac{n(n+1)}{(2n-1)(2n+3)} f_n \\
&\qquad + \frac{(n+1)(n+2)(n+3)}{(2n+3)(2n+5)} f_{n+2} \Bigg] = 0 \quad .
\end{aligned} \tag{3.6}$$

3.3 Deriving a Set of Coupled Differential Equations to Arbitrary Order

In this section we will apply the appropriate manipulations and Legendre polynomial identities to the drift-averaged kinetic equation to obtain a generalized set of coupled differential equations that describe the evolution of the system to arbitrary order n. For this derivation we will start with the equation for the 1D flux tube model from Section 3.2

$$\frac{\partial f}{\partial t} + \frac{\dot{n}}{3n} v \frac{\partial f}{\partial v} + R(t) \left[P_2(\xi) v \frac{\partial f}{\partial v} + \frac{3}{2} \xi (1-\xi^2) \frac{\partial f}{\partial \xi} \right] = \nu \mathcal{L} f \tag{3.7}$$

where we recall that $\xi = v_{\|}/v$, $R = \left|\frac{\delta B}{B} - \frac{2}{3}\frac{\delta n}{n}\right|$, and $\mathcal{L} = \frac{\partial}{\partial \xi}(1-\xi^2)\frac{\partial}{\partial \xi}$. We recall that $P_2(\xi)$ is the second Legendre polynomial, where the first few Legendre polynomials are given by

$$P_0(x) = 1 \tag{3.8}$$

$$P_1(x) = x \tag{3.9}$$

$$P_2(x) = \frac{1}{2}(3x^2 - 1) \tag{3.10}$$

$$P_3(x) = \frac{1}{2}(5x^3 - 3x) \tag{3.11}$$

which we can rewrite in terms of the powers of x

$$1 = P_0(x) \tag{3.12}$$

$$x = P_1(x) \tag{3.13}$$

$$x^2 = \frac{1}{3}(2P_2(x) - P_0(x)) \tag{3.14}$$

$$x^3 = \frac{1}{5}(2P_3(x) + 3P_1(x)) \quad . \tag{3.15}$$

As in the derivation in Section 3.2, we start by expanding the distribution function in terms of Legendre polynomials,

$$f = \sum_n f_n(v,t) P_n(\xi) \quad , \tag{3.16}$$

which will then insert into Eq. 3.7 to yield the equation,

$$\frac{\partial f_n}{\partial t} P_n + \frac{\dot{n}}{3n} v \frac{\partial f_n}{\partial v} P_n + R\left[P_2(\xi)P_n(\xi) v \frac{\partial f_n}{\partial v} + \frac{3}{2}\xi(1-\xi^2)\frac{\partial P_n}{\partial \xi} f_n\right] = \nu \frac{\partial}{\partial \xi}(1-\xi^2)\frac{\partial P_n}{\partial \xi} f_n \quad . \tag{3.17}$$

For this derivation we will need to use the orthogonality of the Legendre polynomials over the interval $(-1, 1)$

$$\int_{-1}^{1} P_n(x) P_m(x) dx = \frac{2}{2n+1}\delta_{mn} \tag{3.18}$$

as well as the recurrence relations

$$(x^2-1)\frac{dP_n(x)}{dx} = xnP_n(x) - nP_{n-1}(x) \tag{3.19}$$

$$(2n+1)xP_n(x) = (n+1)P_{n+1}(x) + nP_{n-1}(x) \qquad . \tag{3.20}$$

From the form of Eq. 3.17 it is clear that we will need to find P_2P_n, $\xi(1-\xi^2)(dP_n/d\xi)$, and $(\partial/\partial\xi)(1-\xi^2)(\partial P_n/\partial\xi)$. The latter is a commonly used expression that is known to have a simple solution, *i.e.*

$$\frac{\partial}{\partial\xi}(1-\xi^2)\frac{\partial P_n}{\partial\xi} = -n(n-1)P_n \qquad . \tag{3.21}$$

For the other expressions, a combination of Eq. 3.19 & 3.20 can be combined and with some manipulations to obtain the necessary expressions

$$P_1(\xi)P_n(\xi) = \frac{n+1}{2n+1}P_{n+1}(\xi) + \frac{n}{2n+1}P_{n-1}(\xi) \tag{3.22}$$

$$\begin{aligned} P_2(\xi)P_n(\xi) = \frac{3}{2}\Bigg[&\frac{(n+1)(n+2)}{(2n+1)(2n+3)}P_{n+2}(\xi) + \frac{n(n-1)}{(2n+1)(2n-1)}P_{n-2}(\xi) \\ &+ \left(\frac{(n+1)^2(2n-1)+n^2(2n+3)}{(2n-1)(2n+1)(2n+3)} - \frac{1}{3}\right)P_n(\xi)\Bigg] \end{aligned} \tag{3.23}$$

$$\begin{aligned} \xi(1-\xi^2)\frac{dP_n(\xi)}{d\xi} = &\frac{n(n-1)(n+1)}{(2n-1)(2n+1)}P_{n-2}(\xi) + \frac{n(n+1)}{(2n-1)(2n+3)}P_n(\xi) \\ &- \frac{n(n+1)(n+2)}{(2n+1)(2n+3)}P_{n+2}(\xi) \qquad . \end{aligned} \tag{3.24}$$

When we insert these expressions back into Eq. 3.17 we obtain the expression

$$\begin{aligned} &\sum P_n(\xi)\frac{\partial f_n}{\partial t} + \sum n(n+1)\nu P_n(\xi)f_n + \sum P_n(\xi)\frac{\dot{n}}{3n}v\frac{\partial f_n}{\partial v} \\ &\quad + \frac{3}{2}R\Bigg[\sum\frac{(n+1)(n+2)}{(2n+1)(2n+3)}P_{n+2}(\xi)v\frac{\partial f_n}{\partial v} \\ &\quad + \sum\left(\frac{(n+1)^2(2n-1)+n^2(2n+3)}{(2n-1)(2n+1)(2n+3)} - \sum\frac{1}{3}\right)P_n v\frac{\partial f_n}{\partial v} \\ &\qquad + \sum\frac{n(n-1)}{(2n-1)(2n+1)}P_{n-2}(\xi)v\frac{\partial f_n}{\partial v} + \sum\frac{n(n-1)(n+1)}{(2n-1)(2n+1)}P_{n-2}(\xi)f_n \\ &\qquad + \sum\frac{n(n+1)}{(2n-1)(2n+3)}P_n(\xi)f_n - \sum\frac{n(n+1)(n+2)}{(2n+1)(2n+3)}P_{n+2}(\xi)f_n\Bigg] = 0 \end{aligned} \tag{3.25}$$

We then adjust the indices to more easily collect terms of $P_n(\xi)$

$$
\begin{aligned}
&\sum P_n(\xi)\frac{\partial f_n}{\partial t} + \sum n(n+1)\nu P_n(\xi) f_n + \sum P_n(\xi)\frac{\dot{n}}{3n} v \frac{\partial f_n}{\partial v} \\
&\quad + \frac{3}{2}R\Bigg[\sum \frac{n(n-1)}{(2n-3)(2n-1)} P_n(\xi) v \frac{\partial f_{n-2}}{\partial v} \\
&\quad + \sum\left(\frac{(n+1)^2(2n-1)+n^2(2n+3)}{(2n-1)(2n+1)(2n+3)} - \sum\frac{1}{3}\right) P_n v \frac{\partial f_n}{\partial v} \\
&\qquad + \sum \frac{(n+1)(n+2)}{(2n+3)(2n+5)} P_n(\xi) v \frac{\partial f_{n+2}}{\partial v} + \sum \frac{(n+1)(n+2)(n+3)}{(2n+3)(2n+5)} P_n(\xi) f_{n+2} \\
&\qquad + \sum \frac{n(n+1)}{(2n-1)(2n+3)} P_n(\xi) f_n - \sum \frac{n(n-1)(n-2)}{(2n-3)(2n-1)} P_n(\xi) f_{n-2}\Bigg] = 0
\end{aligned}
\tag{3.26}
$$

It is at this point that we use the orthogonality condition shown in Eq. 3.18 to find the nth order differential equation that describes the evolution of the distribution function.

$$
\begin{aligned}
&\frac{\partial f_n}{\partial t} + n(n+1)\nu f_n + \frac{\dot{n}}{3n} v \frac{\partial f_n}{\partial v} \\
&\quad + \frac{3}{2}R\Bigg[\frac{n(n-1)}{(2n-3)(2n-1)} v \frac{\partial f_{n-2}}{\partial v} + \left(\frac{(n+1)^2(2n-1)+n^2(2n+3)}{(2n-1)(2n+1)(2n+3)} - \frac{1}{3}\right) v \frac{\partial f_n}{\partial v} \\
&\qquad + \frac{(n+1)(n+2)}{(2n+3)(2n+5)} v \frac{\partial f_{n+2}}{\partial v} + \frac{(n+1)(n+2)(n+3)}{(2n+3)(2n+5)} f_{n+2} \\
&\qquad + \frac{n(n+1)}{(2n-1)(2n+3)} f_n - \frac{n(n-1)(n-2)}{(2n-3)(2n-1)} f_{n-2}\Bigg] = 0
\end{aligned}
\tag{3.27}
$$

3.4 Solving the coupled differential equations numerically

We can see that the equations we have just derived can be solved numerically to arbitrary precision. However, the size of the n-th order part of the distribution function, f_n falls off quickly with n and for this system contributions beyond the second order in n were negligible.

Taken to second order, the coupled system of differential equations becomes:

$$\frac{\partial f_0}{\partial t} + \frac{R}{5}\left[v\frac{\partial f_2}{\partial v} + 3f_2\right] + \frac{\dot{n}}{3n}v\frac{\partial f_0}{\partial v} = 0 \tag{3.28}$$

$$\frac{\partial f_2}{\partial t} + R\left[v\frac{\partial f_0}{\partial v} + \frac{2}{7}v\frac{\partial f_2}{\partial v} + \frac{3}{7}f_2\right] + \frac{\dot{n}}{3n}v\frac{\partial f_2}{\partial v} = -6\nu f_2 \tag{3.29}$$

In the following comparisons with the results of the kinetic simulations, all numerical solutions were taken to second order, truncating at the f_2 equation, as further terms resulted in negligible improvements in accuracy.

We were unable to find an analytic solution to Eq. 3.28 and 3.29, however it is possible to find an analytic solution for the energy of the system in the limit where $\nu = 0$. We start by taking the second velocity moment of Eq. 3.28 and 3.29 to obtain

$$\frac{dE_0(t)}{dt} = \frac{5}{3}\frac{\dot{n}}{n}(t)E_0(t) + 2R(t)E_2(t) \tag{3.30}$$

$$\frac{dE_2(t)}{dt} = R(t)E_2(t) + \left(\frac{5}{3}\frac{\dot{n}}{n}(t) + R(t)\right)E_2(t) \tag{3.31}$$

where $E_0 = \mathcal{E} = 6\pi\int_0^\infty f_0 v^4 dv$ and $E_2 = 3(P_\parallel - P_\perp) = (6\pi/5)\int_0^\infty f_2 v^4 dv$. We can rewrite this expression, using the real parts of the time-dependent density and magnetic field ($\dot{n}/n$ and $\dot{B}/B$), as

$$\frac{d}{dt}\begin{bmatrix} E_0 \\ E_2 \end{bmatrix} = \begin{bmatrix} \frac{5}{3}\omega\frac{\delta n}{n}\sin(\omega t) & 2\omega\delta R\sin(\omega t) \\ \omega\delta R\sin(\omega t) & \omega\left(\frac{5}{3}\frac{\delta n}{n} + \delta R\right)\sin(\omega t) \end{bmatrix}\begin{bmatrix} E_0 \\ E_2 \end{bmatrix}, \tag{3.32}$$

which we can represent as

$$\frac{du(t)}{dt} = A(t)u(t), \qquad u(t_0) = u_0 \quad . \tag{3.33}$$

which has eigenvalues $\lambda_1(t) = \omega(5/3(\delta n/n) - \delta R)\sin(\omega t)$ and $\lambda_2(t) = \omega(5/3(\delta n/n) +$

$2\delta R)\sin(\omega t)$, such that

$$A(t) = U^{-1}\begin{bmatrix}\lambda_1(t) & 0\\ 0 & \lambda_2(t)\end{bmatrix}U = U^{-1}\Lambda(t)U\ , \qquad \text{where} \qquad U = \begin{bmatrix}-2 & 1\\ 1 & 1\end{bmatrix}\quad . \tag{3.34}$$

So we can rewrite the equation as

$$\frac{dw(t)}{dt} = \Lambda(t)w(t) \tag{3.35}$$

where $w(t) = Uu(t)$. We can then use the Magnus expansion to get a closed form of the solution, where

$$w(t) = \exp(\Omega(t,t_0))w(t_0), \qquad \Omega(t) = \sum_{k=1}^{\infty}\Omega_k(t), \tag{3.36}$$

and

$$\Omega_1 = \int_0^t A(\tau)d\tau \tag{3.37}$$

$$\Omega_n = \sum_{j=1}^{n-1}\frac{B_j}{j!}\int_0^t S_n^{(j)}(\tau)d\tau, \qquad n \geq 2 \tag{3.38}$$

with the generating matrices given recursively through the equations

$$S_n^{(j)} = \sum_{m=1}^{n-j}[\Omega_m, S_{n-m}^{(j-1)}], \qquad 2 \leq j \leq n-1, \tag{3.39}$$

$$S_n^{(1)} = [\Omega_{n-1}, A], \quad S_n^{(n-1)} = \mathrm{ad}_{\Omega_1}^{n-1}(\Lambda) \tag{3.40}$$

where ad_{Ω}^{k} is shorthand for an iterated commutator. The commutativity of the solution, *i.e.* $A(t_1)A(t_2) = A(t_2)A(t_1)$ for any pair of values t_1 and t_2, means that all terms beyond Ω_1 are zero. Using the initial conditions $E_0(t=0) = \mathcal{E}_0$ and $E_2(t=0) = 0$, a closed form solution for the energy of the system with no scattering can be obtained,

$$E_0(t) = \mathcal{E}_0\exp\left(\left(\frac{5}{3}\frac{\delta n}{n} + \frac{1}{2}\delta R\right)\beta(t)\right)\left[\cosh\left(\frac{3}{2}\delta R\beta(t)\right) - \frac{1}{3}\sinh\left(\frac{3}{2}\delta R\beta(t)\right)\right] \tag{3.41}$$

$$\beta(t) = 1 - \cos(\omega t). \tag{3.42}$$

Despite what the form of the equation may suggest, the result is essentially sinusoidal, as can be seen in the example in Fig. 3.2.

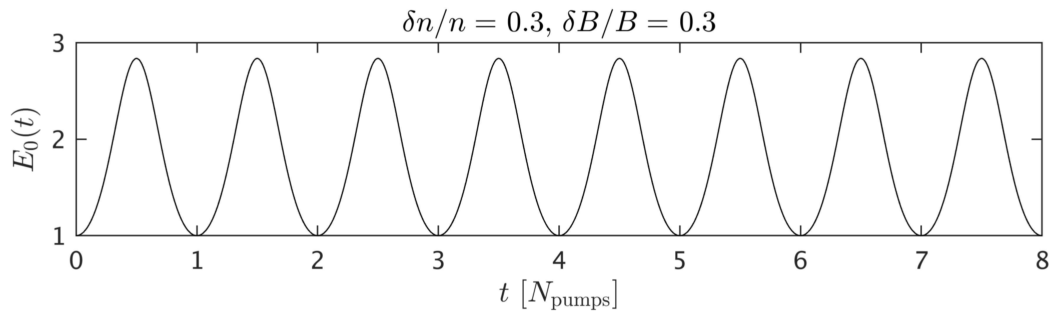

Figure 3.2: Plot of $E_0(t)$ as a function of time for $\delta n/n = 0.3$ and $\delta B/B = 0.3$ with $\mathcal{E}_0 = 1$.

In addition to the numerical solution to Eq. 3.6 we obtain an approximate solution by assuming that each f_n is comprised of a slowly varying component and a rapidly varying component, denoted hereafter as:

$$f_n = f_n^s(v,t) + \tilde{f}_n(v)e^{i\omega t} \quad . \tag{3.43}$$

Inserting this approximation into Eq. 3.6 and collecting terms proportional to $P_2(\zeta)e^{i\omega t}$ we obtain the relation:

$$\tilde{f}_2 = Kv\frac{\partial f_0^s}{\partial v} \quad , \quad K = -\frac{\omega\delta R(\omega + i6\nu)}{\omega^2 + 36\nu^2} \quad . \tag{3.44}$$

Eq. 3.44 shows how the P_2-perturbation of the distribution develops and will, for finite ν, be offset in phase from the drive oscillation in R, by the angle $\theta = \arctan(6\nu/\omega)$. This phase shift is important because when solving for f_0 we obtain non-vanishing time averages from the terms involving $\tilde{f}_2$. Since $\mathcal{E} = \int \frac{3}{2}v^2 f d^3v = 6\pi \int f_0 v^4 dv$, these non-vanishing terms become the source of the energization. Using Eq. 3.44, an equation is obtained for the slowly varying "background" distribution:

$$\frac{\partial f_0^s}{\partial t} - \frac{3}{5}\frac{\nu(\omega\delta R)^2}{\omega^2+36\nu^2}\frac{1}{v^2}\frac{\partial}{\partial v}v^4\frac{\partial f_0^s}{\partial v} = -c_1 f_0 + c_2 f_{\text{ext}} \quad . \tag{3.45}$$

Assuming that there is not a source of cold plasma (*i.e.* $c_2 = 0$), the solutions to Eq. 3.45 then take the form:

$$f_0^s \propto v^\gamma, \quad \gamma = -\frac{3}{2} - \sqrt{\frac{9}{4} + \frac{c_1}{G}}, \quad G = \frac{3}{5}\frac{\nu(\omega\delta R)^2}{\omega^2+36\nu^2} \quad . \tag{3.46}$$

In the limit of no net losses (*i.e.* $c_1 = 0$), the exponent, γ, approaches -3. Thus, the heating mechanism is more than adequate to account for the observations of $f \propto v^{-5}$ distributions typically observed in the solar wind [13, 14].

Applying the results above we can also obtain an expression for how the energy of the system evolves. To accomplish this we first consider the $\nu = 0$ case, assuming f is truncated at the f_2 term:

$$\mathcal{E}_0(t) = \mathcal{E}_0(0)e^{\kappa\beta(t)}[\cosh(\alpha(t)) - \frac{1}{3}\sinh(\alpha(t))] \quad , \tag{3.47}$$

where $\kappa = \frac{5}{3}\frac{\delta n}{n} + \frac{\delta R}{2}$, $\beta(t) = 1 - \cos(\omega t)$, and $\alpha(t) = \frac{3}{2}\delta R\beta(t)$. From the form of the above equation, it is clear that $\mathcal{E}_0(t)$ is essentially sinusoidal with no net energization. To find an approximation to the energy with the all-important scattering included, we combine the $\nu = 0$ solution with an envelope obtained from the first order approximation.

To calculate this envelope, we use Eq. 3.45 to obtain the heating rate $\frac{\partial\mathcal{E}}{\partial t}$. Taking G from Eq. 3.46, for a Maxwellian f_0 and assuming $\nu(v)$ is independent of v, we then find

$$\frac{\partial\mathcal{E}}{\partial t} = \frac{3}{2}G\int_0^\infty v^2\frac{1}{v^2}\frac{\partial}{\partial v}\left(v^4\frac{\partial f_0}{\partial v}\right)4\pi v^2 dv = 10G\mathcal{E} \quad , \quad . \tag{3.48}$$

which gives us

$$\mathcal{E} = e^{\frac{6\nu(\omega\delta R)^2}{\omega^2+36\nu^2}t} \quad . \tag{3.49}$$

We combine these two expressions to obtain a solution for the energy of the system for arbitrary ν that agrees with the simulations presented in the next section

$$\mathcal{E}(t) = \mathcal{E}_0(t) e^{\frac{6\nu(\omega\delta R)^2}{\omega^2+36\nu^2} t} \quad . \tag{3.50}$$

3.5 Kinetic simulations

These predictions were tested using particle-in-cell (PIC) simulations performed with the the VPIC (Vector Particle In Cell) code developed at Los Alamos National Laboratory [41, 42]. While PIC simulations are computationally expensive when compared to other simulation methods such as fluid models they can capture kinetic physics that other simulation methods cannot. VPIC in particular has been used to simulate kinetic plasma physics from magnetic reconnection to laser-plasma interactions in remarkable detail. One of the things that sets VPIC apart from other particle-in-cell codes is its speed and efficiency. In particular, VPIC is designed to minimize data motion within and between micro-processors, as this data motion is more time consuming than the computations themselves and the maximum speed of this data motion is strictly limited by the speed of light.

Outside of its innovative algorithmic set-up, as detailed in the paper by Bowers, *et al.* 2008 [43], VPIC follows the same general workflow as most PIC codes. This workflow is represented visually in Fig. 3.3. First, the simulation domain is subdivided into several sections called cells. For each of the cells, the fields are computed along the edges of the cell from the constituent particles of the cell. To accomplish this, VPIC solves the relativistic Maxwell-Boltzmann equations in a linear background medium,

$$\left[\frac{\partial}{\partial t} + \gamma^{-1}\mathbf{u}\cdot\nabla + \frac{q_s}{m_s}\left(\mathbf{E} + \gamma^{-1}\mathbf{u}\times\mathbf{B}\right)\cdot\nabla\right] f_s = \left.\frac{\delta}{\delta t}\right|_{\text{coll}} f_s \tag{3.51}$$

$$\frac{\partial \mathbf{B}}{\partial t} = -\nabla\times\mathbf{E} \tag{3.52}$$

$$\frac{\partial \mathbf{E}}{\partial t} = \epsilon^{-1}\nabla\times\mu^{-1}\mathbf{B} - \epsilon^{-1}\mathbf{J} - \epsilon^{-1}\sigma\mathbf{E} \tag{3.53}$$

$$\nabla\cdot\mathbf{B} = 0 \tag{3.54}$$

$$\nabla \cdot \mathbf{E} = \rho/\epsilon \tag{3.55}$$

where f_s is the instantaneous phase-space distribution of species s, with q_s being the charge of species s, and m_s being the mass of species s. Additionally, ϵ and μ here denote the permittivity and permeability of the background plasma, σ is the background conductivity, and $\gamma = \sqrt{1+u^2}$ is the relativistic factor.

Once the fields are found, the particles' positions are updated based on the forces that they experience from the fields, using the equations of motion

$$\frac{d\mathbf{r}}{dt} = c\gamma^{-1}\mathbf{u} \tag{3.56}$$

$$\frac{d\mathbf{u}}{dt} = \frac{q_s}{m_s c}\left[\mathbf{E} + c\gamma^{-1}\mathbf{u}\times\mathbf{B}\right] \quad . \tag{3.57}$$

After the particles' positions are updated, the new currents for cell are calculated using the expression

$$\mathbf{J} = \sum_s \int d\mathbf{u} q_s c\gamma^{-1}\mathbf{u} f_s \quad . \tag{3.58}$$

This current can then be used to find the electric and magnetic fields on the mesh, and the entire process repeats until the simulation terminates.

While the $\delta/\delta t|_{\mathrm{coll}} f_s$ term can denote a variety of kinetic physics, including ionization effects, for the simulations described in this work this term denotes the presence of a collision operator for binary collisions. The VPIC simulations discussed in this work used a slightly modified form of the Takizuka and Abe collision operator [44], implemented for VPIC by Bill Daughton [45]. The traditional implementation of the Takizuka and Abe collision operator selects particles within a certain radius of each other with a given probability and allows them to 'collide', or exchange momentum with each other. It is a Monte Carlo method that converges to a Boltzmann collision operator as the number of particles increases. Usually the probability of any two particles 'colliding' within a given radius is velocity-dependent in order to obtain the expected velocity-dependence of the scattering operator. However, in our implementation of this operator we have removed the velocity dependence to obtain a scattering operator that acts more closely to that of a pitch-angle scattering operator as opposed to the Boltzmann collision operator.

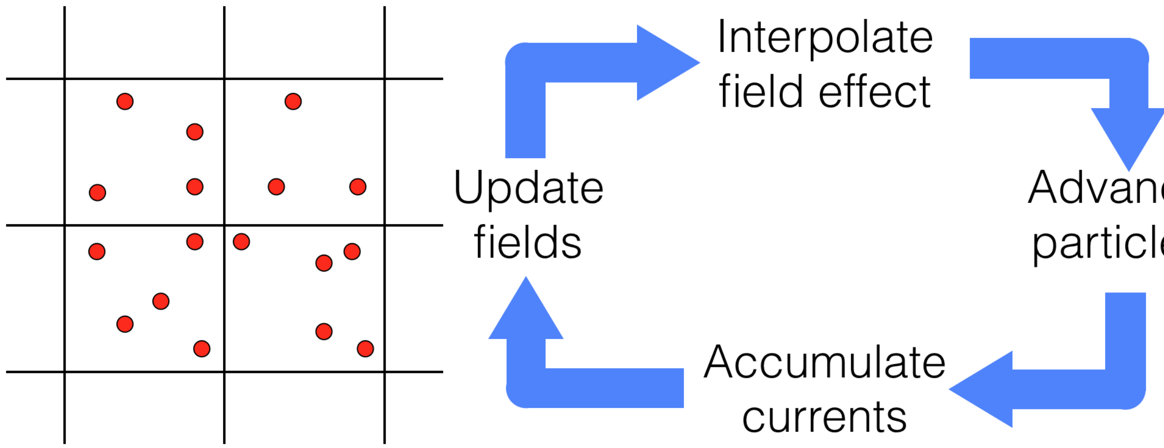

Figure 3.3: **a)** Cartoon representation of the simulation domain. The black lines denote the edges of the cells, that the domain is divided into. The red dots represent the particles that distributed across the domain, and evolved using the process described in **b)**, where the fields are computed along the edges of the cells, the fields are used to advance the position of the particles, the updated particle positions are used to calculate a current, which is then used to update the fields.

3.5.1 VPIC Results

Our initial set-up is a one-dimensional flux tube, as shown in Fig. 3.4(a). The domain is doubly periodic and an external, periodically driven current is applied along two infinite current sheets each located halfway between the mid-line and the top and bottom edge of the simulation space. The oppositely directed current sheets cause flux tube expansions and contractions as the current oscillates (as show in Fig. 3.4(b)). The background distribution is given by a Maxwellian with uniform temperature, $T_e = T_i = T_0$ with the mass ratio given by $m_i/m_e = 100$. The simulations used a non-relativistic thermal speed $v_{the}/c = 0.0707$ and $\omega_{pe}/\Omega_{e0} = 1$. Spatial scales are normalized by d_e, and our pumping frequency, ω_{pump}, is normalized by ω_{pe}. In the simulations presented below we use $\omega = \omega_{pump} = 0.1\ \omega_{pe}$, where

ω_{pump} is referred to hereafter as ω. Our density and magnetic field fluctuations are normalized by the initial density, $n_0 = 1$, and background magnetic field, $\mathbf{B_0} = B_0\hat{x} = 1$, respectively. For the purposes of this initial analysis, the scattering frequency, ν, is velocity-independent and is implemented using the Takizuka and Abe Monte Carlo method employed to calculate Coulomb collisions in VPIC [44, 45]. Only electron-ion collisions are included, so the energy diffusion is minimal given the mass ratio. The 1D flux tube simulations were carried out in VPIC for a variety of scattering frequencies. From Fig.3.4(d) it is clear that magnetic pumping is increasing the temperature of the plasma. Furthermore, both the energization and the phase difference between pressure anisotropy and magnetic field show a dependence on scattering frequency, ν.

Using the approximate solution, we recall that the phase will be offset from the drive oscillation in R by the angle $\theta = \arctan(6\nu/\omega)$, which implies that for $\nu/\omega \in (0, \infty)$, then $\theta \in (0, \pi)$. This can be used to reinforce the intuitive picture of Fig. 3.5(a).

Given the above results, we next compare the predictions of our analytic model with the results from the kinetic simulations. The relationship between the relative energy evolution $(\mathcal{E}/\mathcal{E}(t = 0))$ and the scattering frequency is shown in Fig. 3.5(a). Again there is good agreement between the VPIC simulations and both the exact numerical results of our analytic model as well as the results from the first order approximation. Based on the form of Eq. 3.50, the scattering frequency that will maximize the energization is obtained, as shown in Fig. 3.5(a). The analytic solutions and VPIC results all peak at this most efficient frequency, further lending credence to the agreement between the models. Similarly, for the phase difference between $P_\parallel/P_\perp$ and B there is a good agreement between the two analytic solutions and the VPIC simulations, as in Fig. 3.5(b).

3.6 1D+ Model

For the solar wind, scattering is infrequent and the main isotropizing effect for the pressure anisotropy is thermal streaming, for which we estimate $\nu_{\text{eff}} \sim l_{\text{pert}}/v$. To verify this estimate

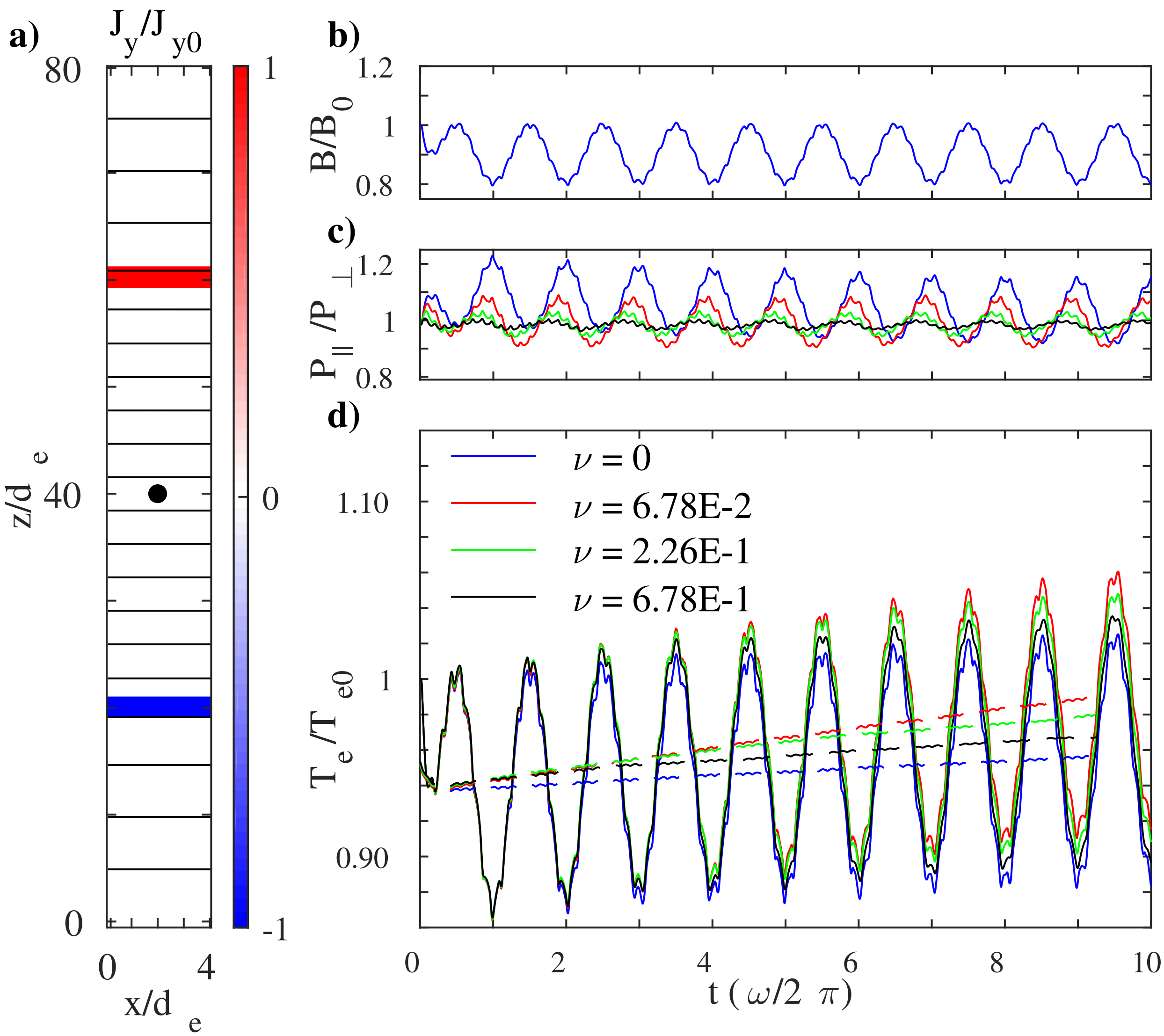

Figure 3.4: **(a)** Representation of the simulation domain. The colored regions are where the external current is applied. The width of the applied current region is increased 2.5x for visualization purposes. The black circle represents the z-coordinate where the measurements in (b-d) were obtained.**(b)** Plot of the magnetic field taken at $z = 40d_e$ **(c)** Plot of the pressure anisotropy taken at $z = 40d_e$ for $\nu/\omega_{pump} = 0$, 6.78E-2, 2.26E-1,and 6.78E-1. (See legend in (d)) **(d)** Plot of temperature taken at $z = 40d_e$. Temperature measurements were obtained by taking $T_e = tr(P)/(3n_e)$. The solid lines are the absolute results and the dotted lines are the average taken over one period.

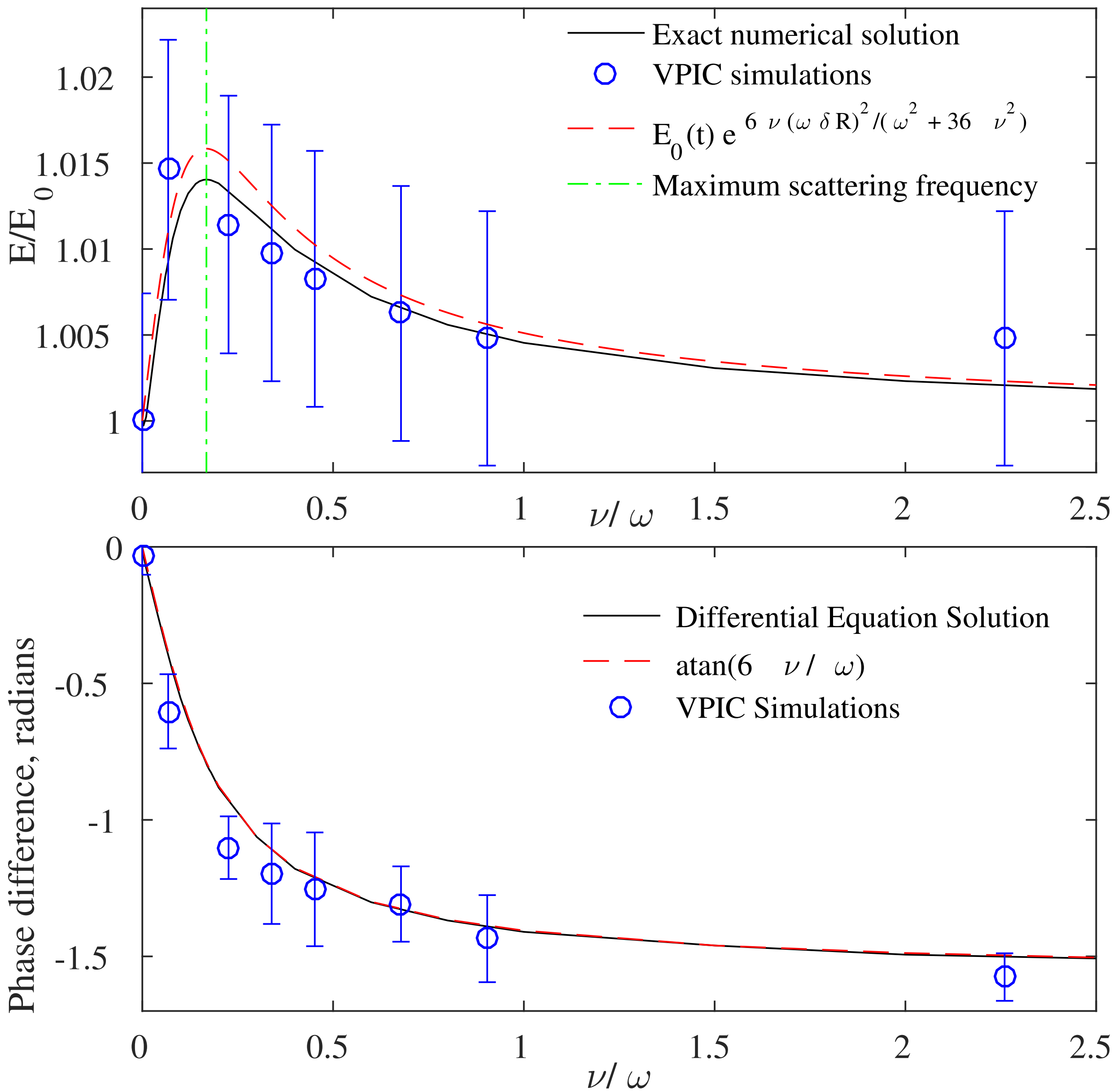

Figure 3.5: **(a)** Comparison of fractional energy increase as a function of scattering frequency for the results of the kinetic simulations and the two analytical methods. Error bars are determined using the standard deviation of particle energies. **(b)** Comparison of phase difference between $P_{\|}/P_{\perp}$ and B as a function of scattering frequency. Phase difference is normalized relative to the $\nu = 0$ phase difference. Error bars are determined using the standard deviation of the phase difference calculated for each period in simulation.

we set up a VPIC simulation using the same domain as the 1D simulations described above, but with no magnetic fluctuations. We initialized the domain with a spatially dependent anisotropy, as shown in Fig. 3.6(a), and observed the decay rate. The results of this for both electrons and ions are shown in Fig. 3.6(b), where the decay rate matches our expectations of $\nu_{\rm eff} \sim l_{\rm pert}/v_{\rm th}$. We note that we expect to observe $\nu_{\rm eff} \sim l_{\rm pert}/v_{\rm th}$ here as opposed to $\nu_{\rm eff} \sim l_{\rm pert}/v$ as this figure shows the decay rate for the entire distribution, for which $\nu_{\rm eff} \sim l_{\rm pert}/v$ would average out to an observation of $\nu_{\rm eff} \sim l_{\rm pert}/v_{\rm th}$. A similar phenomena has been used in other models, such as in the fluid closure by [25]. The isotropization caused by thermal streaming is much larger than that induced by pitch-angle scattering off waves and Coulomb collisions.

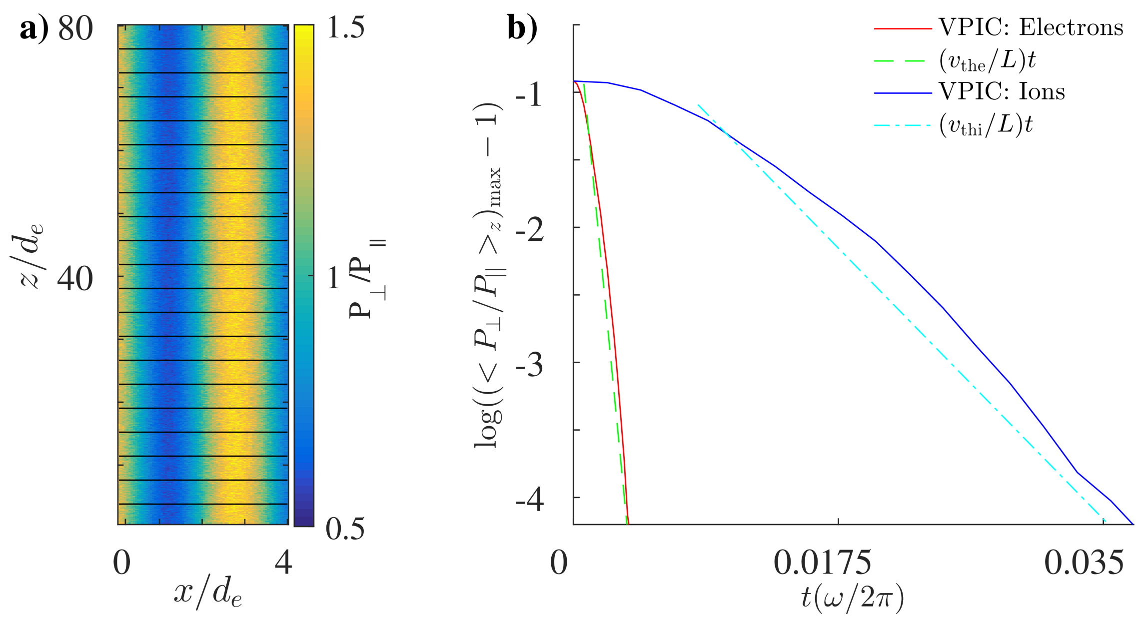

Figure 3.6: **(a)** VPIC initial set-up for testing the parallel streaming. Black lines are field lines of the background magnetic field. **(b)** Results from the VPIC simulations of streaming.

To estimate $\nu_{\rm eff}$ for the solar wind we need to take into account the spatial anisotropy of the fluctuations, *i.e.* that $k_\perp \gg k_\parallel$ [46]. Because the particle streaming is restricted to be along magnetic field lines, only the field-aligned parts of the perturbations are important, such that $\nu_{\rm eff} \sim v k_\parallel/2\pi \sim v/l_{\rm pert}(k_\parallel/k)/2\pi \sim v/l_{\rm pert}(k_\parallel/k_\perp)/2\pi$. Because the magnetic moment

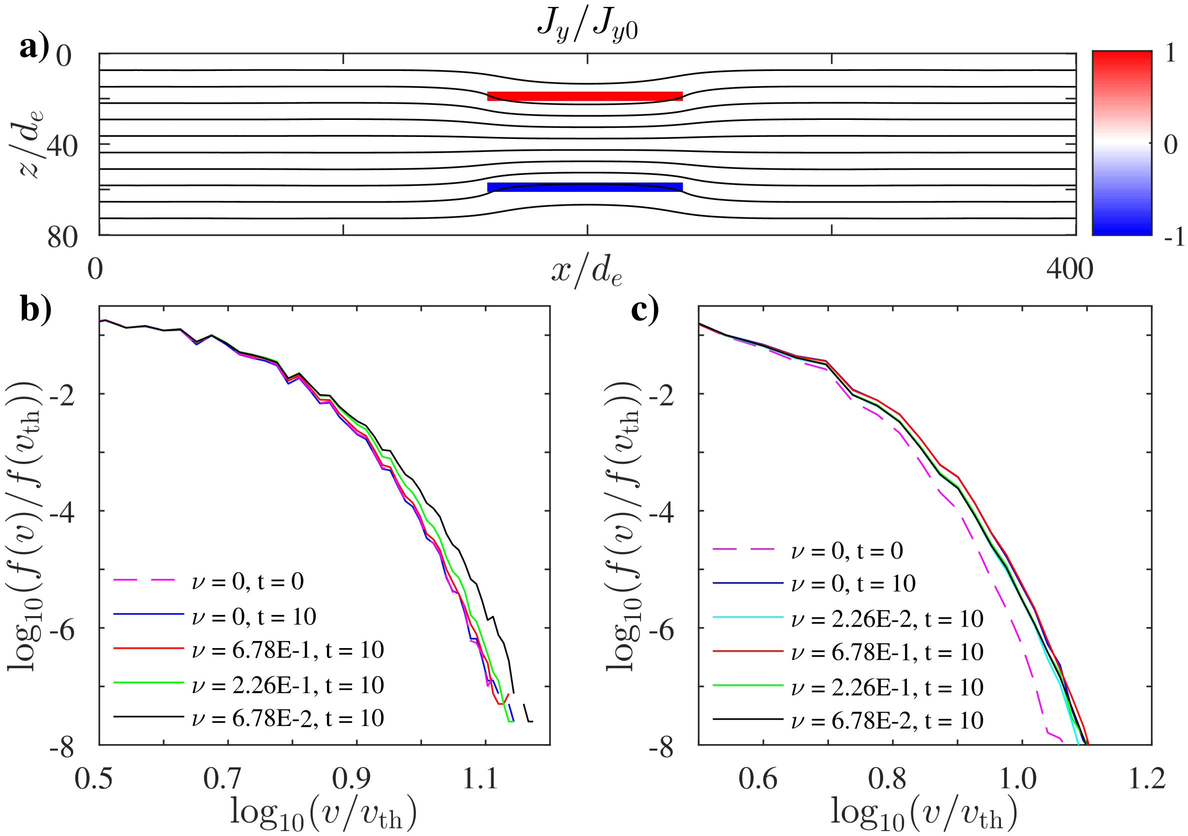

Figure 3.7: **(a)** Simulation domain for the 2D simulations. Notice that the current sheets only stretch across one-fifth of the domain. **(b)** Log-log plot of the distribution function for the 1D simulation. The level of heating is dependent on the scattering frequency, ν. **(c)** Log-log plot of the distribution function for the 2D simulation. Note that the heating is now independent of scattering frequency.

is conserved during streaming, the energization will now be in the parallel direction. The parallel heating can be transferred to the perpendicular directions through standard scattering mechanisms [47, 48]. However, in cases where scattering is sufficiently slow, the large scale and slowly-varying background distribution may develop a significant anisotropy $f_2^s \gtrsim \tilde{f}_2$. To be investigated elsewhere, this will then introduce additional terms in Eq. 3.45 which will help increase the effectiveness of the heating process beyond the examples considered here.

The role of parallel streaming can be tested directly in 2D kinetic simulations, but given the numerical cost only for a limited number of pump cycles. As shown in Fig. 3.7, the set-up is similar to that in Fig. 3.4(a), with the domain extended in the x direction, and the current sheets providing the oscillating magnetic perturbations only cover a portion of the simulation domain. From Fig. 3.7(c), we can see that the heating is no longer dependent on the scattering frequency, ν, as it was in the 1D simulations shown in Fig. 3.7(b). The thermal streaming of electrons in and out of the pumping region acts as an effective scattering process, dominating the applied scattering rates and leading to the expected increase in heating for low values of ν.

3.7 Application to the solar wind

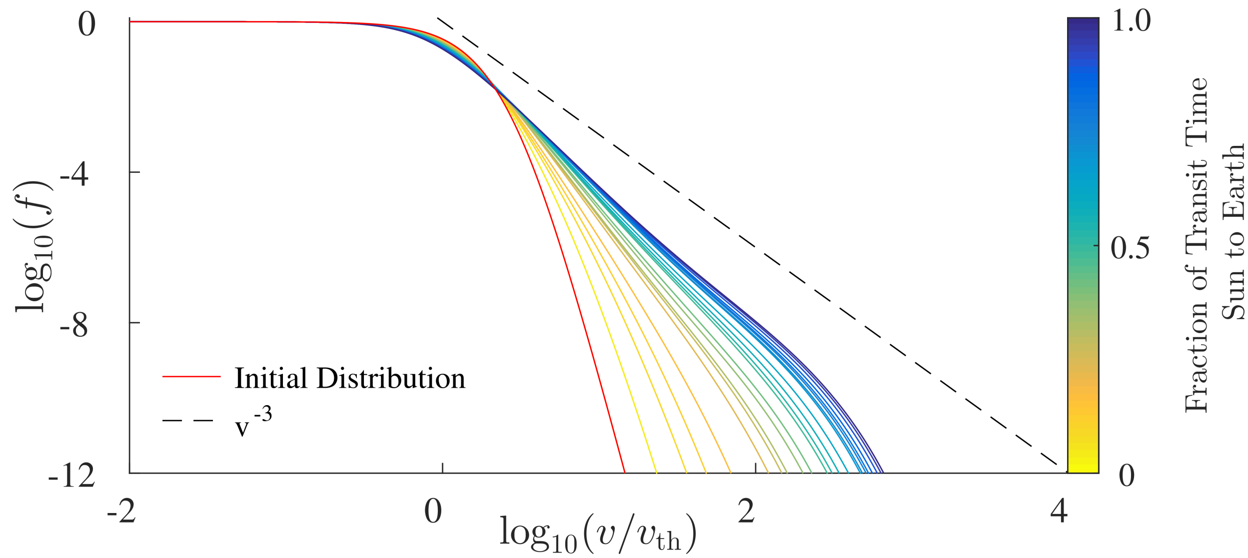

Figure 3.8: Numerical solution for the distribution function after many oscillations. Note that the slope approaches the value commonly observed in the solar wind, $\gamma = -3$. In this plot $v_{\rm th} = 90$ km/s.

To address heating over hundreds of pump cycles, we evolve Eq. 3.5 using parameters relevant to ions in the solar wind. To generate the results in Fig. 3.8 a selection of frequencies were randomly generated and their corresponding $dB/B(\omega)$ were taken from the spectra in [49]. After every cycle a new randomly-generated frequency and corresponding $dB/B(\omega)$ was chosen, so that every cycle the plasma would experience a new frequency, consistent with the observation that fluctuations in MHD turbulence decohere after a single cycle. From [46]

Fig. 7 we used $k_{\parallel}/k_{\perp} \sim 8$ when generating Fig. 3.8. Assuming a solar wind speed of 800 km/s, we obtain an estimate of the total transit time from the Sun to the Earth. We further assume that only 10% of the perturbations that the plasma experiences will be compressional. As shown in Fig. 3.8, we obtain a power-law distribution out to two orders of magnitude in velocity. In the model, the streaming rapidly dissipates the anisotropy at higher velocities, causing the drop-off in the power-law in Fig. 3.8 for $v > v_{wind}(k_{\perp}/k_{\parallel})$. While we observe a power law extending about four orders of magnitude in $\mathcal{E}$, work which will be detailed in Chapters 4 and 5 suggests that the streaming can be reduced by trapping effects, extending the power-law part of the distributions to even higher velocities, $v \gg v_{\mathrm{wind}}(k_{\perp}/k_{\parallel})$.

Chapter 4

2D Model

How does the 2D magnetic pumping model work? How can it be used to explain spacecraft observations of heating in the plasma preceding the Earth's bow shock?

4.1 Introduction

Superthermal populations of ions and electrons are abundant in a wide variety of astrophysical systems throughout the universe, often with distributions characterized by energetic power-law tails [3, 13]. However, the consensus on the physical mechanisms that heat these particles is far from settled. While it is well known that plasma can be energized by waves, most theories of wave-particle energization are only effective for heating particles moving at velocities close to the phase velocity of the waves [50, 51]. We here present a new analysis of particle heating by magnetic pumping. While previous work suggests that heating by pumping is only effective up to the phase velocity of the wave [35], we show that the addition of magnetic trapping of particle orbits renders pumping effective for heating particles moving far faster than the wave speed. The mathematical treatment reveals the underlying Fermi mechanism consistent with the formation of energetic power-law distributions.

Magnetic pumping is a mechanism where energy is transferred from magnetic fluctuations to directly heat the plasma, bypassing the turbulent cascade [52, 53, 54]. Extensive prior work has suggested that the mechanism is not effective for energizing superthermal particles.

For example, in the seminal book on waves in plasmas by Stix, magnetic pumping by compressional waves, related to transit-time damping [34], is shown to be a Landau damping process, where heating is limited to particles moving at the magnetic-field-aligned phase velocity of the wave considered, $v_p = \omega/k_\parallel$. In the framework of quasilinear theory Landau damping causes velocity diffusion limited to particles near the resonance velocity, $v \sim \omega/k_\parallel$, and is derived based on the standard procedure of integrating the plasma kinetic equations along unperturbed particle trajectories.

While the present analysis also follows the approach of quasilinear diffusion, a key difference is that the kinetic equation is integrated in the fast transit time limit[31] including the full evolution of the electron orbits. When a standing wave geometry is considered, the integration along the full orbits yields new, previously-neglected quasilinear terms. With the inclusion of these terms magnetic trapping generates extensive particle energization, applicable for electrons moving at high velocities, $v \gg \omega/k_\parallel$.

The effectiveness of pumping in the regime $v \gg \omega/k_\parallel$ is closely tied to the presence of trapped electrons, an example of which is shown in Fig. 4.1. Over the course of each pump cycle the trapped portion of the distribution function develops significant structure in velocity space. The corresponding pressure anisotropy can be moderated by processes such as pitch-angle-mixing or a limited confinement time of the electrons in the magnetic wells, causing a phase delay between the perpendicular pressure, $p_\perp$, and the flow perpendicular to the magnetic field, $\mathbf{u}_\perp$. Given this phase delay, when averaged over a pump cycle, mechanical work by $p_\perp \nabla_\perp \cdot \mathbf{u}_\perp$ then becomes finite and is the source of the energy for the heating process.

The main result of our quasilinear analysis with trapped electron effects in the limit where $v \gg \omega/k_\parallel$ is a velocity diffusion equation similar to that obtained by Lichko 2017[35] for the opposite limit, $v_\parallel \ll \omega/k_\parallel$. More specifically, the slowly-varying background distribution f_0 is governed by a diffusion equation of the form

$$\frac{\partial f_0}{\partial t} = \frac{1}{v^2}\frac{\partial}{\partial v}\left(v^2 D \frac{\partial f_0}{\partial v}\right), \quad D = \omega v^2 \mathcal{G}\left(\frac{\delta B}{B}, \nu/\omega\right) \tag{4.1}$$

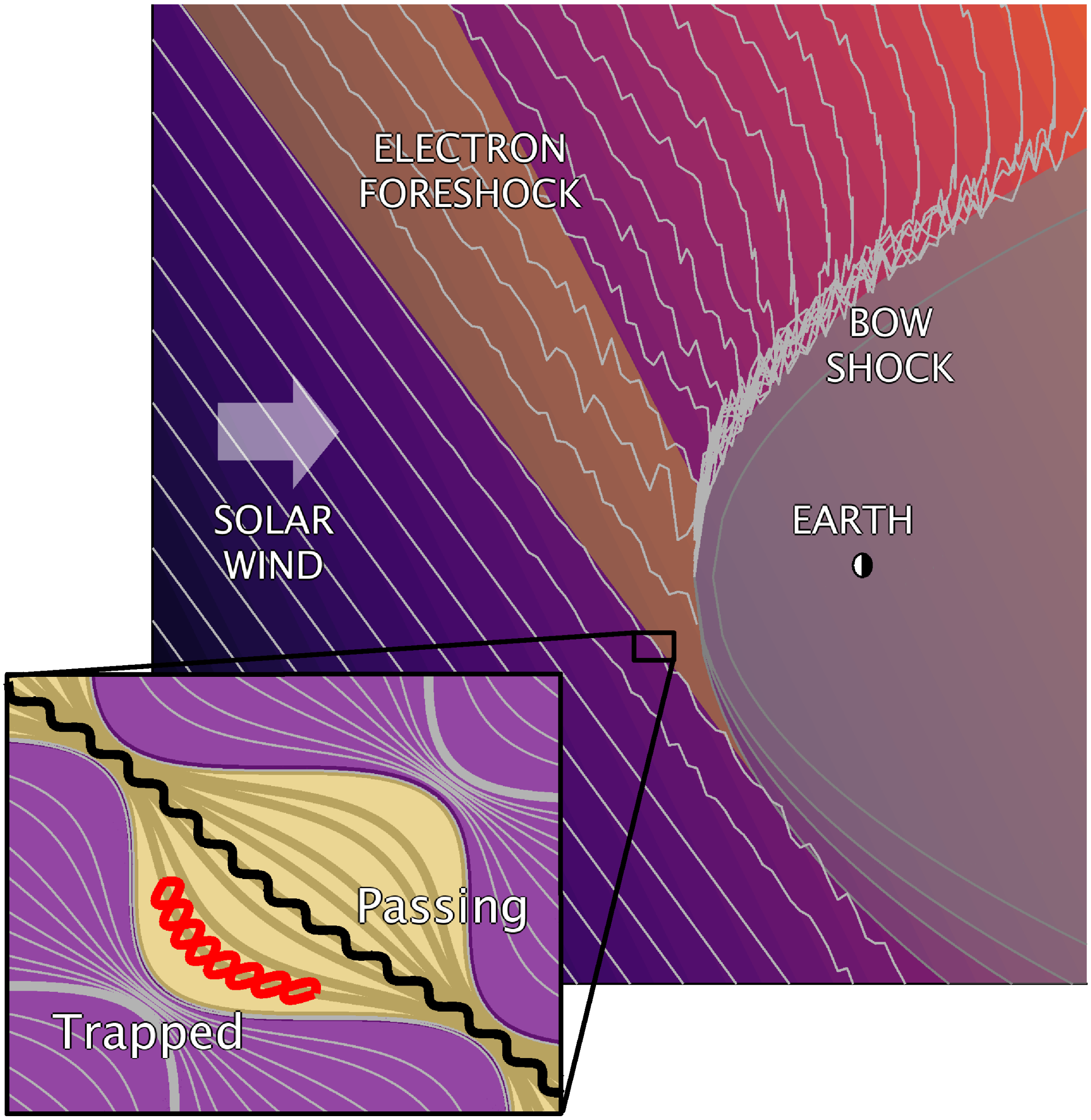

Figure 4.1: Cartoon of a flux tube and a set of trapped (red) and passing (black) particle orbits.

where $\mathcal{G}$ is independent of v, but is a function of the effective scattering frequency relative to the frequency of the fluctuations, ν/ω, and the size of the magnetic perturbations relative to the background magnetic field, $\delta B/B$. The result that $D \propto \omega v^2$ is evidence of a Fermi heating process with a diffusive step size proportional to the velocity, $\Delta v \propto v$.

Fundamentally, magnetic pumping is a nonlinear interaction between two oppositely-propagating compressional waves, which is typically neglected in the derivation of quasilinear diffusion. In the analysis mentioned above, the assumption of an isotropic background distribution was relaxed and nonlinear terms that beat with the applied perturbation were included. However in this analysis, as well as many classic derivations of quasilinear diffusion, only the zeroth-order trajectories of the particles where the orbits are assumed to be unperturbed are considered, such as the trajectory shown by the black line in the inset to Fig. 4.1. As will be shown in this chapter, when the perturbed orbits are included, such as those shown in Fig. 4.1 which include the effects of trapped and passing orbits, magnetic pumping can heat particles moving much faster than the wave speed, *i.e.* $v >> \omega/k_{\|}$. The inclusion of trapping allows for pressure anisotropy to remain persistent in the trapped particle population, thus allowing magnetic pumping to energize the particles.

4.2 MMS Observations

Below we will outline how Eq. 4.1 is obtained and provide an evaluation of $\mathcal{G}$, a metric of the effectiveness of the pumping process. Meanwhile, it is instructive to first consider observations by the Magnetospheric Multiscale (MMS) mission in the region of the Earth's bow shock [55]. These observations served both as guidance and motivator of our analytic model.

The MMS mission consists of four spacecraft flying in a tetrahedral formation around the magnetosphere, as shown in the cartoon in Fig. 4.3. The leftmost red ellipse denotes the orbit of MMS in Phase 1 of the mission, where the spacecraft observed magnetic reconnection near the Earth's dayside. Now the spacecraft are moving into Phase 2, denoted by the rightmost red ellipse, which will allow data to be collected on magnetic reconnection in the Earth's magnetotail. The science mission of MMS is to resolve the microphysics of magnetic reconnection, and to determine the kinetic processes that are responsible for collisionless magnetic reconnection. Studying this regime required a significant upgrade in the measurement of the velocity distribution function. Previous missions required the spacecraft to undergo a full rotation in order to get a full 3D distribution function. Since the spacecraft may only pass through a reconnection site for a fraction of a second, something much faster

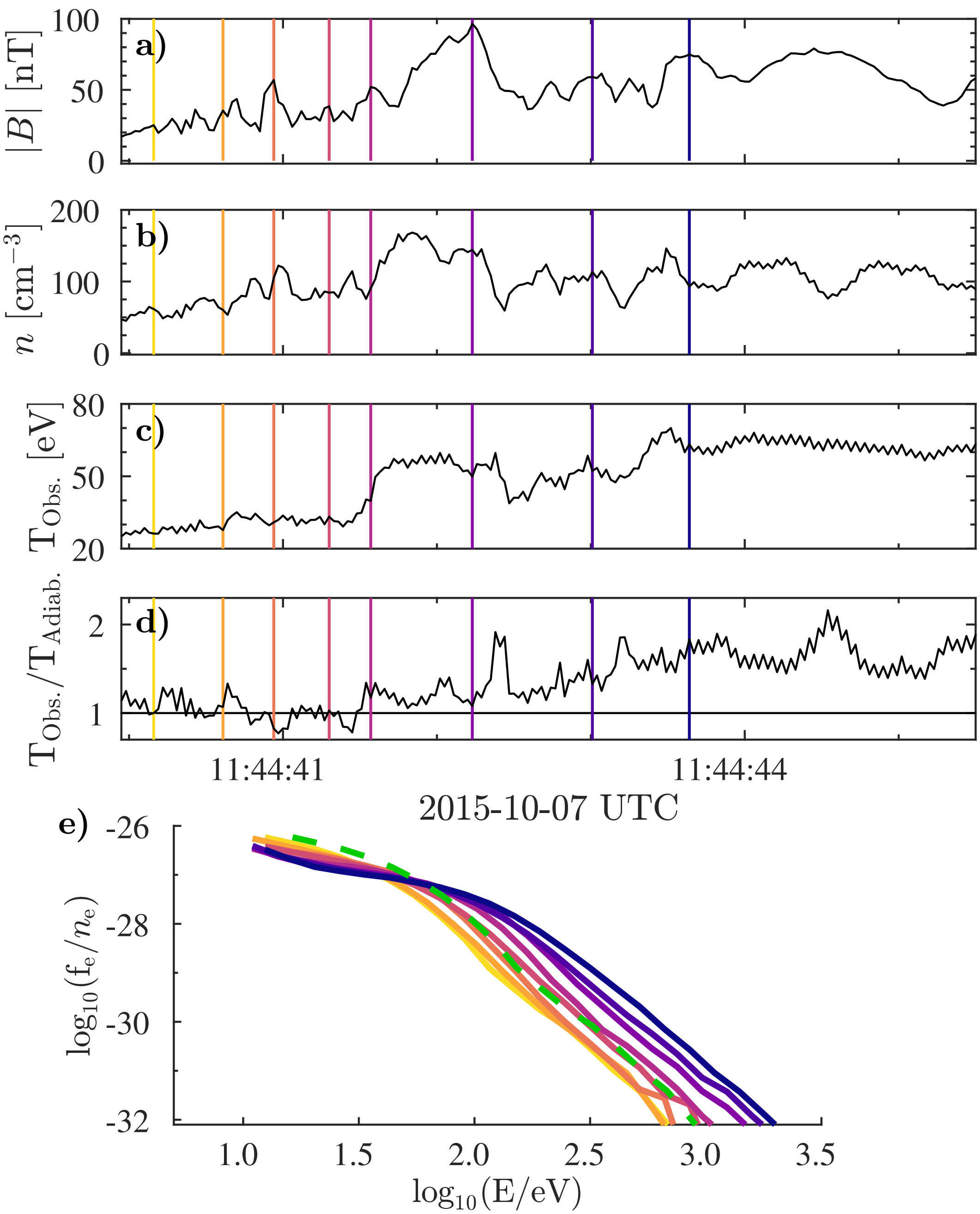

Figure 4.2: **(a)** Plot of the average magnetic field from MMS1 as a function of time. The spacecraft starts in the solar wind and as time goes on approaches the Earth's bow shock. **(b)** Plot of the density from MMS1 as a function of time. **(b)** Plot of the observed temperature ($T_{\rm Obs.} = Tr(P)/(3n)$) from MMS1 as a function of time. **(d)** Plot of the observed temperature as compared to the temperature expected from compressional heating alone ($T_{\rm Adiab.} = n^{2/3}$). **(e)** Pitch-angle-averaged distributions at the times denoted by the colored lines in (a-d). The green dashed line denotes what the final distribution at the last point should look like if it only underwent compressional heating from the yellow time point to the blue time point. All of these time points are chosen to be upstream of the shock front itself.

was needed to resolve the kinetic physics. In Fig. 4.3 we can see one of the MMS spacecraft with the diagnostics that measure the distribution function. Each spacecraft has four sensors are used to detect the electrons and another four for the ions, denoted in the picture above as DES (Dual Electron Sensors) and DIS (Dual Ion Sensors), distributed evenly around the spacecraft. Each sensor is made of two spectrometers whose field of view is separated by 45 degrees, each of which can scan through a 45-degree arc for a larger panorama. All together the sensors can observe the entire sky. For reference, the box for each dual sensor and its components is about the size of a small toaster oven. These sensors can combine to produce a 3D distribution function every 30 milliseconds. The incredible detail in the velocity-space distributions make MMS ideal not just for investigating magnetic reconnection, but also kinetic processes in general, including magnetic pumping.

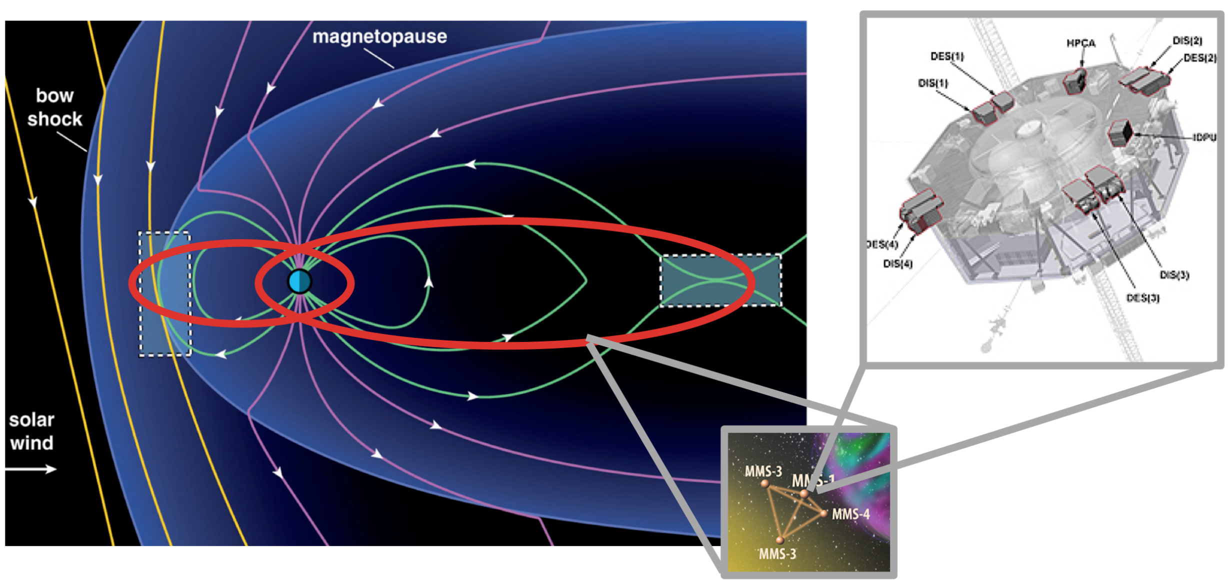

Figure 4.3: The leftmost diagram depicts the incoming solar wind, and the bow shock that forms as the wind hits Earth's magnetopause. The red ellipses denote the different orbits of the spacecraft during the different phases of the MMS missions. This image was taken from Burch, *et al.* 2016[55]. The first inset depicts the four MMS spacecraft, flying in a tetrahedral formation, with the image reproduced from Amano 2016 [56]. The final inset shows a close-up of one of the MMS spacecraft, with the different electron and ion distribution diagnostics labeled, taken from NASA [57].

Upstream of the shock front there are ripples, variations in the magnetic field itself, that have been shown to be a source of electron acceleration, as well as other large-amplitude magnetic field fluctuations[58, 59, 60, 61, 62]. An example of such fluctuations can be seen in data from the MMS mission, taken as the four spacecraft crossed the Earth's bow shock on October 7th, 2015[63]. From the time histories of $|B|$, n, $T_{\rm obs}$, and $T_{\rm obs}/T_{\rm adiabatic}$, as shown in Fig. 4.2(a-d), it can be seen that despite the strong, compressional fluctuations the temperature increase is greater than would be expected from compressional heating alone. The pitch-angle-averaged distribution functions in these pre-shock fluctuations, as shown in Fig. 4.2(e) for the times marked in Figs. 4.2(a-d), demonstrate energy transfer consistent with a Fermi heating mechanism, where $\Delta v \sim v$.

4.3 Detailed derivation of the model

Because the formation of anisotropy in the electron distributions is fundamental to our pumping model we start this analysis by demonstrating that the observed anisotropy is consistent with electron trapping in a standing wave perturbation and is representative of the perturbed distribution function driven during each pumping cycle. We consider the limit where the bounce time, τ_b, is much smaller than the time scales associated with the waves. In this limit "instantaneous" particle orbits are then described by the magnetic moment, $\mu = mv_\perp^2/(2B)$ and the total energy $U = \mathcal{E} - e\Phi$. Furthermore, we consider electron energies larger than the electrostatic potential associated with the perturbations [64], such that the $v \times B$ part of the Lorentz force dominates the orbit motion. At each time point during the magnetic pump cycle an instantaneous electron orbit is fully characterized by μ and $\mathcal{E}$. In turn, from the multiple time scale method[31, 65] the distribution must be constant along these instantaneous orbits, reducing the dimensionality of the problem.

Starting with the drift kinetic equation[66] with pitch-angle mixing, *i.e.*

$$\frac{df}{dt} = \nu\mathcal{L}f, \quad \mathcal{L} = \frac{\partial}{\partial\xi}(1-\xi^2)\frac{\partial}{\partial\xi}, \quad \xi = \frac{v_\parallel}{(v_\parallel^2 + v_\perp^2)^{1/2}}, \tag{4.2}$$

we then change variables from $f(t, x, v_\perp, v_\parallel) = f(t, \mathcal{E}, \chi)$, where $\mathcal{E} = \frac{1}{2}mv^2$ and $\chi = \Lambda/(j^2+\Lambda)$, where $\Lambda = \mu B_0/\mathcal{E}$ and $j = J/(4vL) = 1/(vL)\int_0^{L_b} v_\parallel dx$ with L_b denoting the bounce point. Here $\mathcal{E}$ and χ are both constant of motion variables where χ is representative of $v_\perp^2/v^2$ along the instantaneous orbits.

The kinetic description applied in this work is limited to the superthermal particles characterized by speeds, v, sufficiently large that the Lorentz force is dominated by the magnetic term, *i.e.* $vB \gg E$. To be more specific, in our drift kinetic analysis we are concerned with the parallel motion along the magnetic field, in general governed by forces due to the parallel electric field and the magnetic mirror force. For plasma variations of scale length L, the magnitude of these forces can be estimated as $|e\nabla_\parallel \Phi| \simeq T_e/L$ and $|\mu \nabla_\parallel B| \simeq mv^2 \delta B/(2B_0 L)$, and it follows that the superthermal limit requires $v^2 \gg v_t^2 B_0/(\delta B)$, where v_t is the electron thermal speed and $\delta B/B_0$ is the normalized magnetic fluctuation amplitude.

In the superthermal limit the description of the orbit motion is significantly simplified as the value of $v_\parallel/v = \sqrt{1-\Lambda B}$ along an orbit is only dependent on $\Lambda = \mu B_0/\mathcal{E}$ (and independent of the electron energy $\mathcal{E}$ with the assumption $E_\parallel = 0$). This strongly simplifies the calculation of the second adiabatic invariant $J(v, \Lambda)$ because $j = J/(4vL)$ is then a function of only Λ, readily evaluated numerically for the slowly evolving magnetic perturbation considered, as illustrated in Fig. 4.4, where

$$j(\Lambda, t) = \frac{1}{4L}\oint \frac{v_\parallel}{v} dl = \frac{1}{2L}\int_0^{L_b} \sqrt{1 - \Lambda B(t, x)}dx \quad . \tag{4.3}$$

Given this calculation of $j(\Lambda, t)$ over the course of a full pump cycle we can determine $\Lambda(\chi, t)$ and in turn obtain $j(\chi, t)$ as shown in Fig. 4.4(c). This function is fundamental to our analysis as it is related to the instantaneous rate of particle energization. Because $dJ/dt = d(vj)/dt = 0$ it follows that $j\,dv/dt + v\,dj/dt = 0$. Furthermore, as $j = j(\chi, t)$ and $d\chi/dt = 0$, we have $dj/dt = \partial j/\partial t|_\chi$, such that $v^{-1}dv/dt = -j^{-1}\partial j/\partial t|_\chi$. We then obtain the result implicit in Eq. 4.5 that

$$\left.\frac{d\mathcal{E}}{dt}\right|_{\chi} = -\mathcal{E}H, \text{ where } H \equiv \frac{2}{j}\left.\frac{\partial j}{\partial t}\right|_{\chi} \quad . \tag{4.4}$$

Using these new variables and following the approach of Montag *et al.* 2017[67], we obtain an orbit-averaged form of Eq. 4.2

$$\frac{\partial f}{\partial t} - H(t,\chi)\mathcal{E}\left.\frac{\partial f}{\partial \mathcal{E}}\right|_{\chi,t} = \nu \left\langle \mathcal{L} \right\rangle_x f \tag{4.5}$$

where $H = (2/j)(\partial j/\partial t)|_{\chi}$, $\langle(...)\rangle_x = 1/(\tilde{\tau}_b L)\int_0^{L_b} dx(...)/\sqrt{1-\Lambda(B/B_0)}$ is the orbit-averaging integral, and $\tilde{\tau}_b = v\tau_b/(4L)$ is the velocity-normalized bounce time.

As outlined above, our model is averaged over the fast electron orbit motion. Locally we assume that the scattering process is described by the familiar Lorentz pitch-angle scattering operator, $\mathcal{L}$, which is then subject to orbit averaging [65, 31]. For this orbit averaging, it is convenient to express $\mathcal{L}$ in terms of the constant of motion variable Λ. Starting with the Lorentz pitch-angle scattering operator in terms of $\xi = v_{\parallel}/v$,

$$\mathcal{L} = \frac{1}{2}\frac{\partial}{\partial \xi}(1-\xi^2)\frac{\partial}{\partial \xi} \tag{4.6}$$

we rewrite the scattering operator in terms of the new variables, Λ and $\mathcal{E}$

$$\mathcal{L} = \frac{m v_{\parallel} B_0^2}{\mathcal{E}^2 B}\left.\frac{\partial}{\partial \Lambda}\right|_{\mathcal{E}} \mu v_{\parallel} \left.\frac{\partial}{\partial \Lambda}\right|_{\mathcal{E}}, \quad v_{\parallel} = \sqrt{2\mathcal{E}(1-\Lambda\tilde{B})/m} \tag{4.7}$$

which then takes the form

$$\mathcal{L} = \left(\frac{2}{\tilde{B}} - 3\Lambda\right)\left.\frac{\partial}{\partial \Lambda}\right|_{\mathcal{E}} + \frac{2}{\tilde{B}}\Lambda(1-\Lambda\tilde{B})\left.\frac{\partial^2}{\partial \Lambda^2}\right|_{\mathcal{E}}. \tag{4.8}$$

After averaging along the spatial dimension of the flux tube we then obtain the orbit-averaged

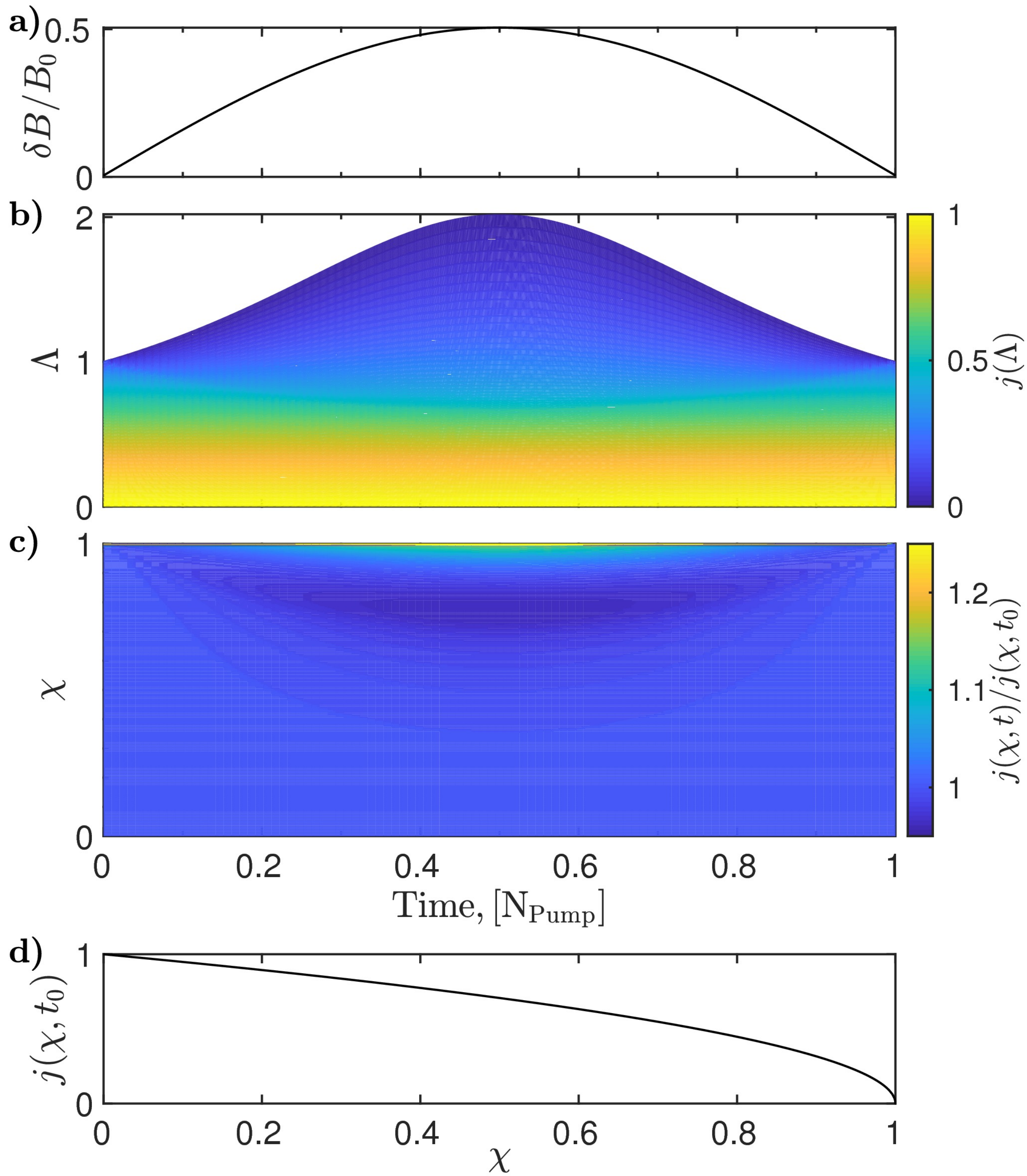

Figure 4.4: **(a)** Plot of the maximum magnetic field amplitude over the course of a fluctuation for a maximum magnetic field of $\delta B/B_0 = 0.5$ **(b)** Plot of j as a function of Λ over the course of a fluctuation for the magnetic field in (a). **(c)** Plot of $j(\chi, t)$ normalized by $j(\chi, t_0)$ for the same fluctuation. **(d)** Plot of $j(\chi, t_0)$.

operator,

$$\langle \mathcal{L} \rangle_x = \left(2 \left\langle \frac{1}{\tilde{B}} \right\rangle_x - 3\Lambda \right) \frac{\partial}{\partial \Lambda}\bigg|_{\mathcal{E}} \\ + 2\Lambda \left(\left\langle \frac{1}{\tilde{B}} \right\rangle_x - \Lambda \right) \frac{\partial^2}{\partial \Lambda^2}\bigg|_{\mathcal{E}}, \tag{4.9}$$

where the definition of $\langle (...) \rangle_x$ is given just below Eq. 4.5.

In the limit of negligible scattering, $\nu = 0$, we solve Eq. 4.5 numerically, assuming an initial isotropic distribution and a standing wave magnetic field, $\tilde{B}(x,t) = 1 - (\delta B/B_0)\sin(\omega t)\cos\left(k_\| x\right)$. The resultant distribution functions are shown in Fig. 4.5(a-h) for selected positions along the flux tube at a time t_0 where $\sin(\omega t_0)(\delta B/B_0) = 0.5$.

Despite the idealized form of the magnetic perturbation, there is good agreement between these model distribution functions and the distribution functions observed by MMS, as shown in Fig. 4.5(f-i), over the course of a single fluctuation of commensurate size, as shown in Fig. 4.5(j). This is true not just for this representative fluctuation, but also throughout the bow shock encounter, as can be seen in Fig. 4.6.

The model distributions (here at $\nu = 0$) have sharper features in velocity space compared to those observed by MMS. This difference may be related to the imperfect confinement of the trapped electrons within the local magnetic mirrors, but in some cases can likely be accounted for also by pitch-angle diffusion through electron scattering off of whistler waves[12].

An estimate of the effective scattering rate for the MMS event can be found by integrating the model in Eq. 4.5 for various values of ν and using this reference set to match the anisotropic features of an observed distribution function. For example, the distribution displayed in Fig. 4.5(k) was obtained by integrating Eq. 4.5 with $\nu/(\omega/2\pi) = 0.75$ and provides an excellent match to the MMS distribution in Fig. 4.5(d).

We can estimate how much scattering is needed to match the spacecraft observations by comparing the MMS distributions to theoretical distributions generated by integrating Eq. 4.5 for a range of scattering frequencies, ν. By comparing the anisotropic features in the MMS distribution to the features in this set of theoretical distribution functions, we can

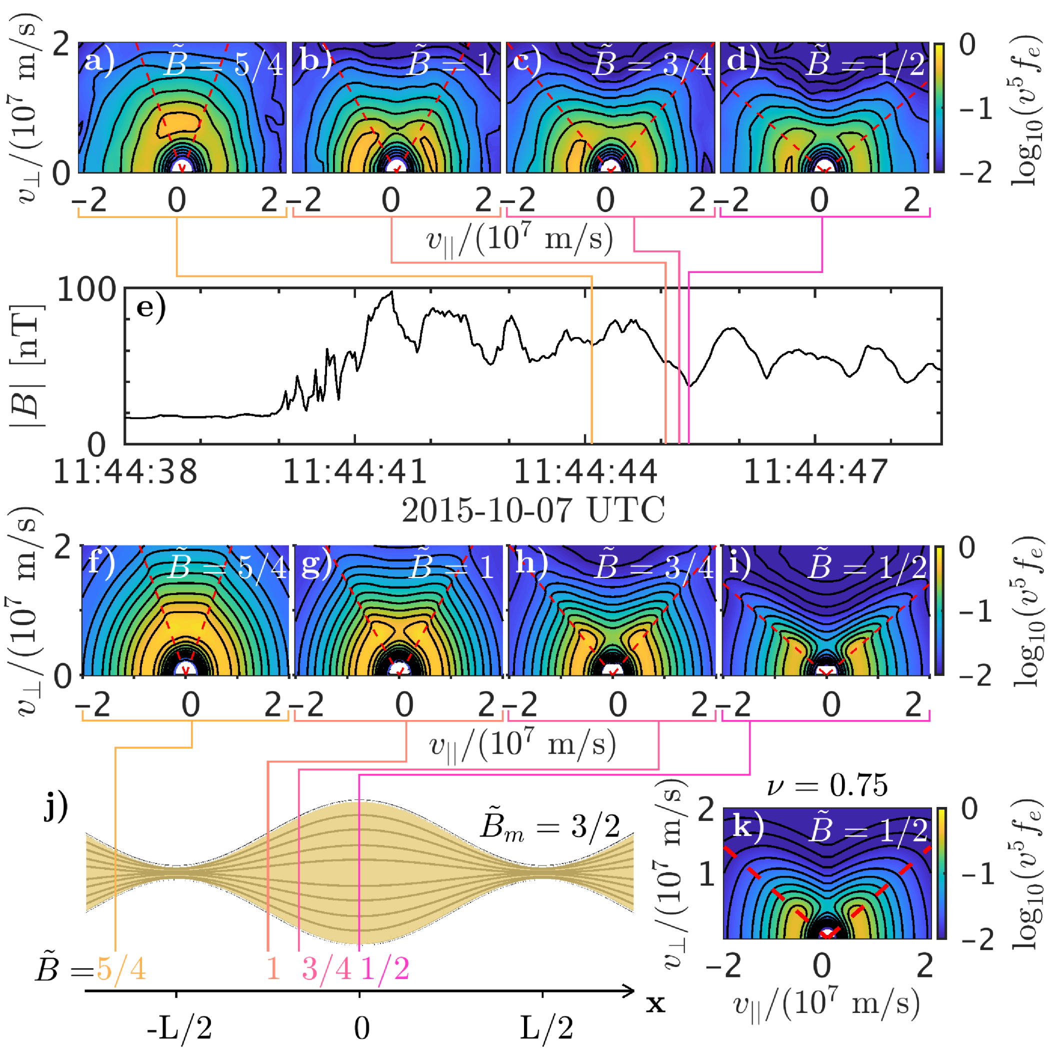

Figure 4.5: **(a-d)** show the electron distributions recorded by MMS3 for the rippled foreshock event reported in Ref. [63] for the estimated points along the fluctuation where $\tilde{B} \in \{5/4, 1, 3/4, 1/2\}$. The distributions are weighted by the factor v^5 to visually enhance the anisotropic features. **(e)** Magnetic field strength along the foreshock encounter, where the colored lines denote the times where the distributions in (a-d) were taken. **(f-i)** Expected distribution functions computed using Eq. 4.5 integrated at $(\delta B/B_0)\sin(\omega t_0) = 0.5$. The distributions are evaluated at the same $\tilde{B}$ inferred from the MMS data in (a-d). In this comparison we have applied the Taylor hypothesis[68], that the changes in B recorded by the spacecraft are mainly caused by the spatial, not temporal, variations. For all electron distributions, the red dashed lines indicate the trapped/passing boundaries, characterized by $v_\perp^2/v_\parallel^2 = (B_0 + \delta B)/B(t_0, x) - 1$. The enhanced values of f along these trapped-passing boundaries are due to the fact that electrons near these boundaries have orbits with near stagnation, $v_\parallel/v \simeq 0$, which causes the orbit average of the energizing term, $\mu(\partial B/\partial t)$, to become large and positive. **(j)** shows a cartoon version of the flux tube. **(k)** shows the theoretical distribution in (i) scattered with the Lorentz operator, $\mathcal{L}$, for $\nu/(\omega/2\pi) = 0.75$

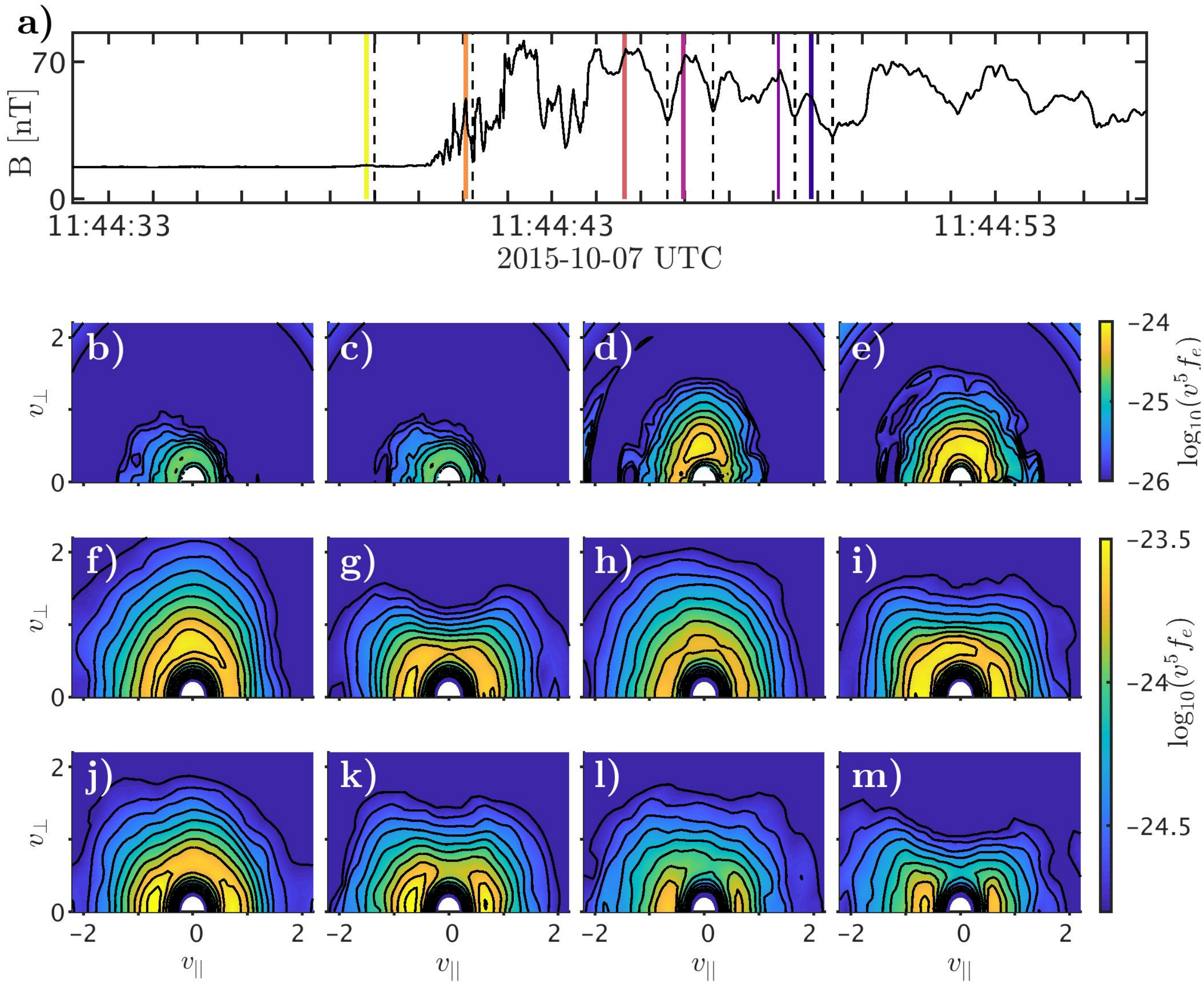

Figure 4.6: **(a)** Magnetic field strength, B, recorded by MMS4. **(b-m)** Electron distributions measured at times corresponding to the peaks and valleys of the magnetic perturbations, where the distributions with colored borders correspond to the peaks marked in (a) and the subsequent distribution functions correspond to the adjacent valleys, marked on (a) with the dashed lines. The anisotropy is highlighted by applying the weighting factor of v^5.

estimate the effective scattering frequency in the solar wind. Based on a least-squared-fit analysis, the scattering frequency that best fit this data varies as a function of velocity, where $\nu/(\omega/2\pi) \in [0.25, 1.5]$. A scattering frequency within this range, $\nu/(\omega/2\pi) = 0.75$, is chosen to generate a comparison with the MMS data, where the resulting scattered distribution is shown in Fig. 4.5(k).

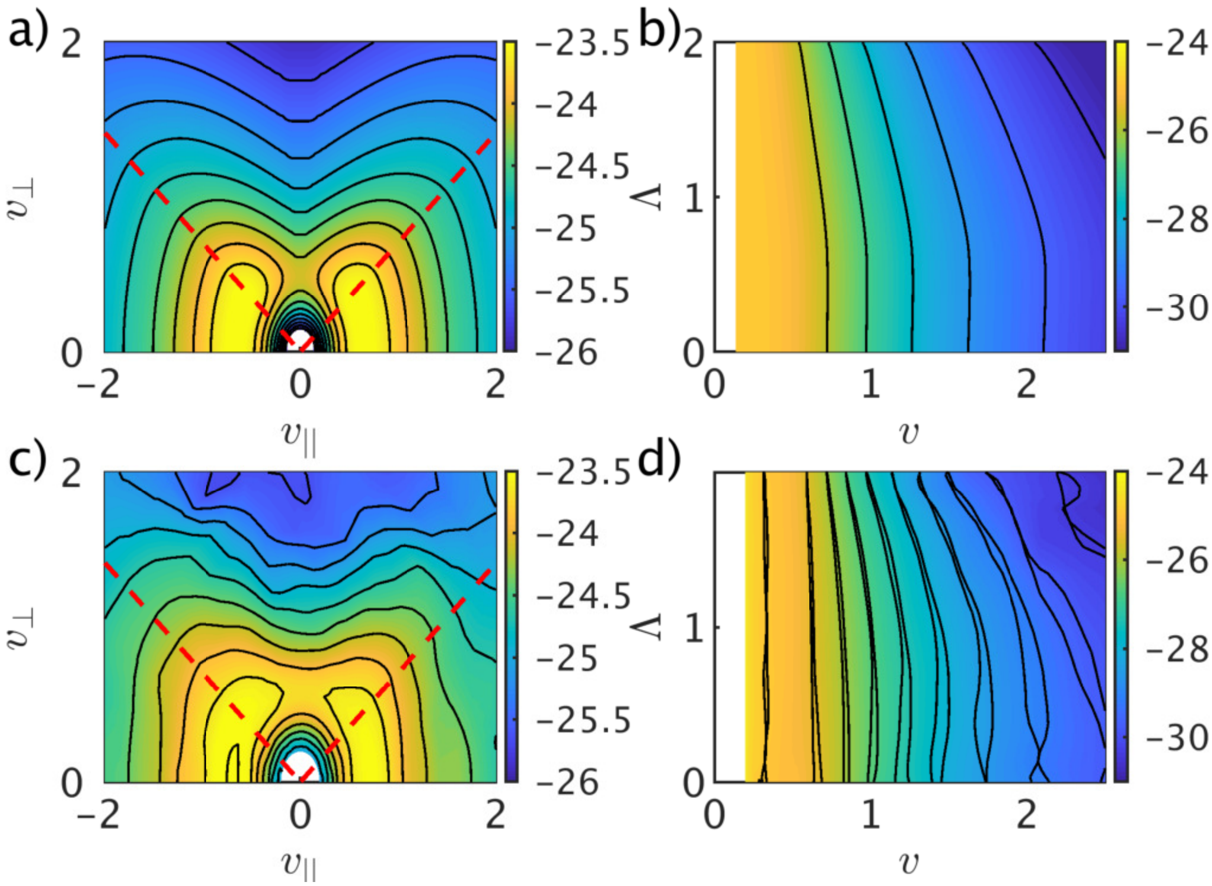

Figure 4.7: **(a)** This distribution function was generated by the model for a perturbation with $\delta B/B_0 = 0.5$. This distribution was scattered using a Lorentz collision operator with $\nu = 0.75$. The red dashed lines denote the trapped-passing boundaries and the distribution sis weighted by a factor of v^5 to better visualize the anisotropic features. **(b)** shows the same distribution function, but transformed to (v, Λ) space. In both (a) and (b) the lines of constant velocity are plotted in black. **(c)** shows a velocity distribution from the MMS spacecraft during a fluctuation of commensurate size as the distribution shown in (a) the distribution is again weighted by a factor of v^5. **(d)** shows the same velocity distribution as in (c), but here plotted in (v, Λ) space.

To find the scattering frequency that best fit the MMS observations, we created a set of scattered distribution functions with scattering frequencies, $\nu/(\omega/2\pi) \in [0, 1.5]$. The method of least-squared fit, $R(v_m; \delta F_{\text{Amp}}; \delta\Lambda_{\text{Amp}}) = \sum_n((f_{\text{Theory}}(v_m, \Lambda_n + \delta\Lambda_{\text{Amp}}) + \delta F_{\text{Amp}}) - f_{\text{MMS}}(v_m, \Lambda_n))^2$, was used to find the best fitting parameters for a given line of constant velocity for a given scattering frequency. This is due to the difficulty in reproducing exactly the same distribution function - some variations in the absolute magnitude are to be expected from the difference in the inflowing and outflowing plasma.

Once the set of best fitting parameters are found, the χ^2 value was found for the particular velocity, v_m, and scattering frequency, $\nu/(\omega/2\pi)$, where $\chi^2 = \sum_n(f_{\text{Theory,Fit}}(v_m, \Lambda_n) - f_{\text{MMS}}(v_m, \Lambda_n))^2/f_{\text{MMS}}(v_m, \Lambda_n)$ and the minimum value of χ^2 corresponds to the best fit.

Because the theoretical distribution that these scattered distributions were compared to were generated under the assumption of high velocity particles, only velocities that correspond to energies above 200 eV were considered.

The agreement demonstrated above suggests that the model is capturing the anisotropic features of the observed distribution functions and the analysis can be extended to address the heating of the electron population over many cycles. Following the blueprint of the quasilinear method, we then separate the distribution function into the slowly-varying, isotropic background distribution, f_0, and the anisotropic portion of the distribution function, f_1,

$$f = f_0(t, \mathcal{E}) + f_1(t, \mathcal{E}, \chi), \quad f_0(t, \mathcal{E}) = \langle f(t, \mathcal{E}, \chi) \rangle_\chi \,, \tag{4.10}$$

where the χ-averaging, $\langle(...)\rangle_\chi = (\int d\chi (d\Lambda/d\chi)\tilde{\tau}_b(...))/(\int d\chi (d\Lambda/d\chi)\tilde{\tau}_b)$. To make Eq. 4.5 more analytically tractable, the Lorentz operator is approximated with the Krook operator, where

$$\mathcal{L}_K = -C_K(f - \langle f \rangle_\chi) \quad . \tag{4.11}$$

The Lorentz operator more effectively isotropizes anisotropic structures with sharper, finer features. As can be seen in Fig. 4.5, the angular scale length of these features is related to the opening angle of the trapped-passing boundaries, which is controlled by $\delta B/B_0$, so the

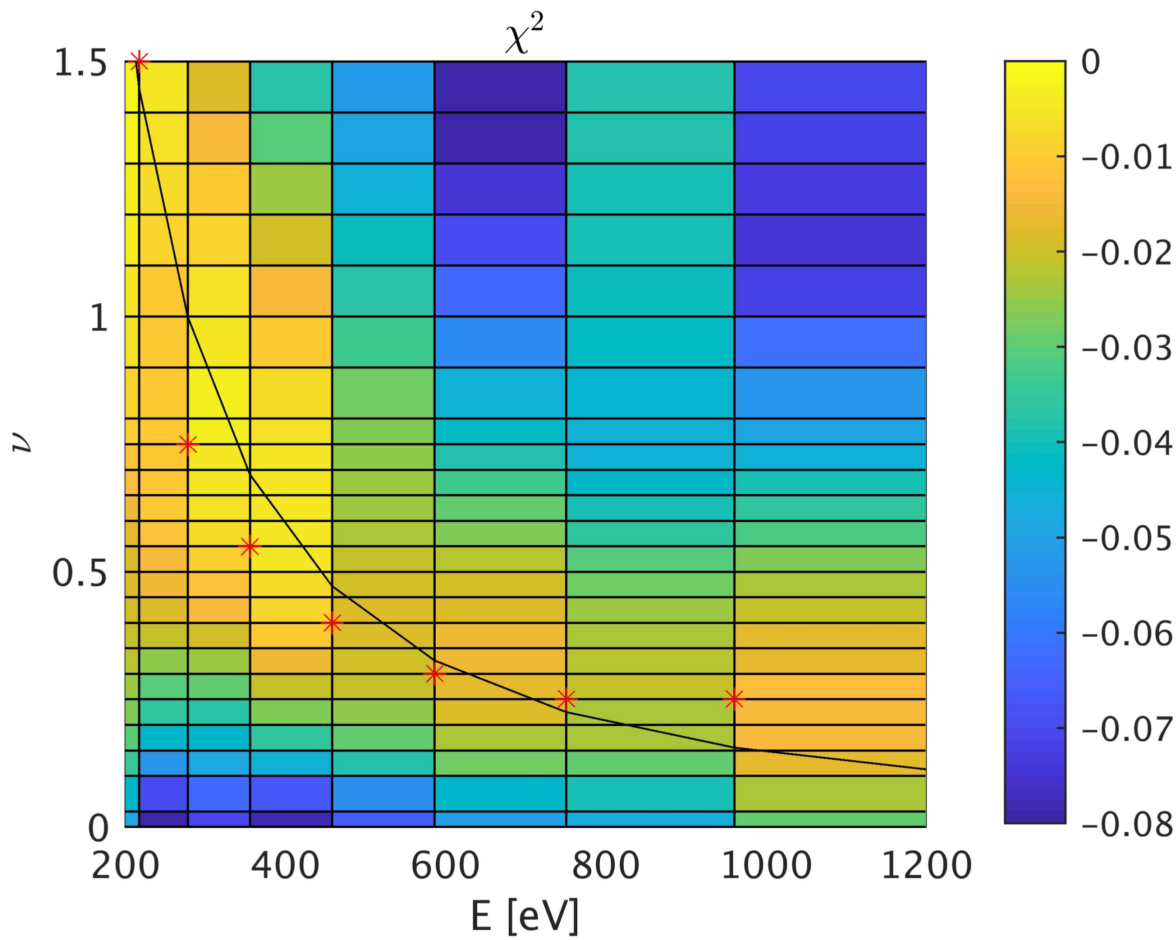

Figure 4.8: Plot of the χ-squared fit as a function of scattering frequency, ν, and energy, E.

effectiveness of $\mathcal{L}$ must depend on $\delta B/B_0$. In our Krook representation this dependency is included through $C_K = C_K(\delta B/B_0)$.

As is clear from the form of Eq. 4.6, the Lorentz operator describes diffusion of anisotropic features of the distribution function, f. Accordingly, the diffusion time scales as $\tau_D \propto (\delta\xi)^2$, where $\delta\xi$ is the typical scale for the anisotropic features of f. As the magnetic field increases, the trapped portion of the distribution function will increase commensurately, yielding larger values of $\delta\xi$.

The Krook operator does not have this same dependence on $\delta\xi$, as the rate of isotropization is in fact independent of $\delta\xi$. When computing the Krook collision operator the new, scattered distribution function is formed from a linear combination of the original distribution function, and a fully isotropized version of the distribution function,

$$f_{t+\Delta t} = (1-\alpha) f_t + \alpha \left\langle f_t \right\rangle_\chi , \tag{4.12}$$

where $\alpha = \exp(-\nu C_K \Delta t)$ determines the rate of isotropization.

To approximate the $\delta\xi$ dependency of $\mathcal{L}$ we have introduced the coefficient C_K. From an analysis of the kinetic equation it follows that $\delta\xi$ of f is similar to $\delta\xi$ of $g = j^2 + \Lambda$, which we used to provide a calibration for the efficiency of the Krook operator:

$$C_K = \frac{\left\langle (g - \langle g \rangle_\Lambda) \mathcal{L} g \right\rangle_\Lambda}{\left\langle (g - \langle g \rangle_\Lambda)^2 \right\rangle_\Lambda}. \tag{4.13}$$

By repeating this computation for a multiple $\delta B/B_0$ we find the result scales as

$$C_K(\delta B/B_0) = 1.15/(\delta B/B_0)^{1.13} \tag{4.14}$$

which is the result we used to compute the Krook distribution curves earlier in the chapter.

In addition to this approximation of the Lorentz scattering operator, the anisotropic part of the distribution function, f_1, as well as the other relevant anisotropic terms $H(t,\chi)$ and $h(t,\chi) = H - \langle H \rangle_\chi$ are Fourier transformed such that $f_1 = \sum_n f_1^n e^{in\omega t}$, $H = \sum_n H^n e^{in\omega t}$, and $h = \sum_n h^n e^{in\omega t}$.

By inserting these expansions and Eq. 4.10 into Eq. 4.5 an equation for the anisotropic part of the distribution function is found,

$$f_1^n = K_n \mathcal{E} \frac{\partial f_0}{\partial \mathcal{E}}, \qquad K_n = \frac{h^n(-in\omega + C_K \nu)}{n^2\omega^2 + (C_K\nu)^2}. \tag{4.15}$$

Inserting f_1 back into Eq. 4.5, an evolution equation is obtained for the slowly-varying background distribution $\partial f_0/\partial t = \left\langle \langle H f_1 \rangle_\chi \right\rangle_t$. Evaluating $\left\langle \langle H f_1 \rangle_\chi \right\rangle_t$ is somewhat involved and the calculation is given in detail in Chapter 5. Here we just provide the result of the calculation which is the recovery of Eq. 4.1

$$\frac{\partial f_0}{\partial t} = \frac{1}{v^2}\frac{\partial}{\partial v}\left(v^2 D \frac{\partial f_0}{\partial v}\right), \quad D = \omega v^2 \mathcal{G}\left(\frac{\delta B}{B}, \nu/\omega\right)$$

with

$$\mathcal{G} = \sum_n \frac{C_K \nu/\omega \left\langle \left\langle \mathrm{Re}(H^n e^{in\omega t})\, \mathrm{Re}(h^n e^{in\omega t}) \right\rangle_\chi \right\rangle_t}{4\omega^2 (n^2 + (C_K \nu/\omega)^2)}. \tag{4.16}$$

which again evidences the characteristic dependence of diffusive step size on velocity, $\Delta v \sim v$, that would be expected for a Fermi heating process.

We validate the analytical model of Eqs. 4.1 and 4.16 by integrating Eq. 4.5 numerically for a range of ν and considering a range of perturbation amplitudes, $\delta B/B_0$.

The numerical solver works as follows. First, the relevant parameters as a function of χ are computed over the course of a fluctuation, specifically $\tilde{B}(x,t) = 1 - \delta B/B_0 \sin(\pi t)\cos(\pi x)$, where $x \in [0,1]$ and $t \in [0,1]$. Earlier in this section we described how to find j as a function of Λ for a given $\delta B/B_0$, which here is associated with a given time. The same can be done for other parameters for a given time, t, specifically Λ, $g = j^2 + \Lambda$, j^2/Λ, $\tilde{\tau}_b$, and $(1/\tilde{\tau}_b)\int (1/\tilde{B})/\sqrt{1 - \Lambda B/B_0}dx$. The latter is used to calculate the orbit-averaged Lorentz operator, $\langle \mathcal{L} \rangle_x$. These values can then be interpolated using the same method as before to find their values as a function of χ. We can also use the conservation of the magnetic moment, $\mu v^2 \Lambda(\chi)/(2B_0)$ to find the change in energy over every time step.

Using the expected change in energy from the magnetic moment conservation, dE and the fact that χ is a constant of motion, a new distribution $F_{\mathrm{new}}(\ln(v_{\mathrm{new}}), \chi)$ is found at every time step by interpolating the old distribution $F_{\mathrm{old}}(\ln(v_{\mathrm{old}}), \chi)$. If there is no scattering, this interpolation will evolve the distribution, including the effects of particle trapping, without any net energization.

After the interpolation to the new variables, the distribution function is scattered using the appropriate operator. For the Lorentz operator, the scattered distribution is computed using Eq. 4.9, where $F_{\mathrm{new}} = F_{\mathrm{old}} + dt\,(\nu \langle \mathcal{L} \rangle_x F_{\mathrm{old}})$. For the Krook operator, the scattered

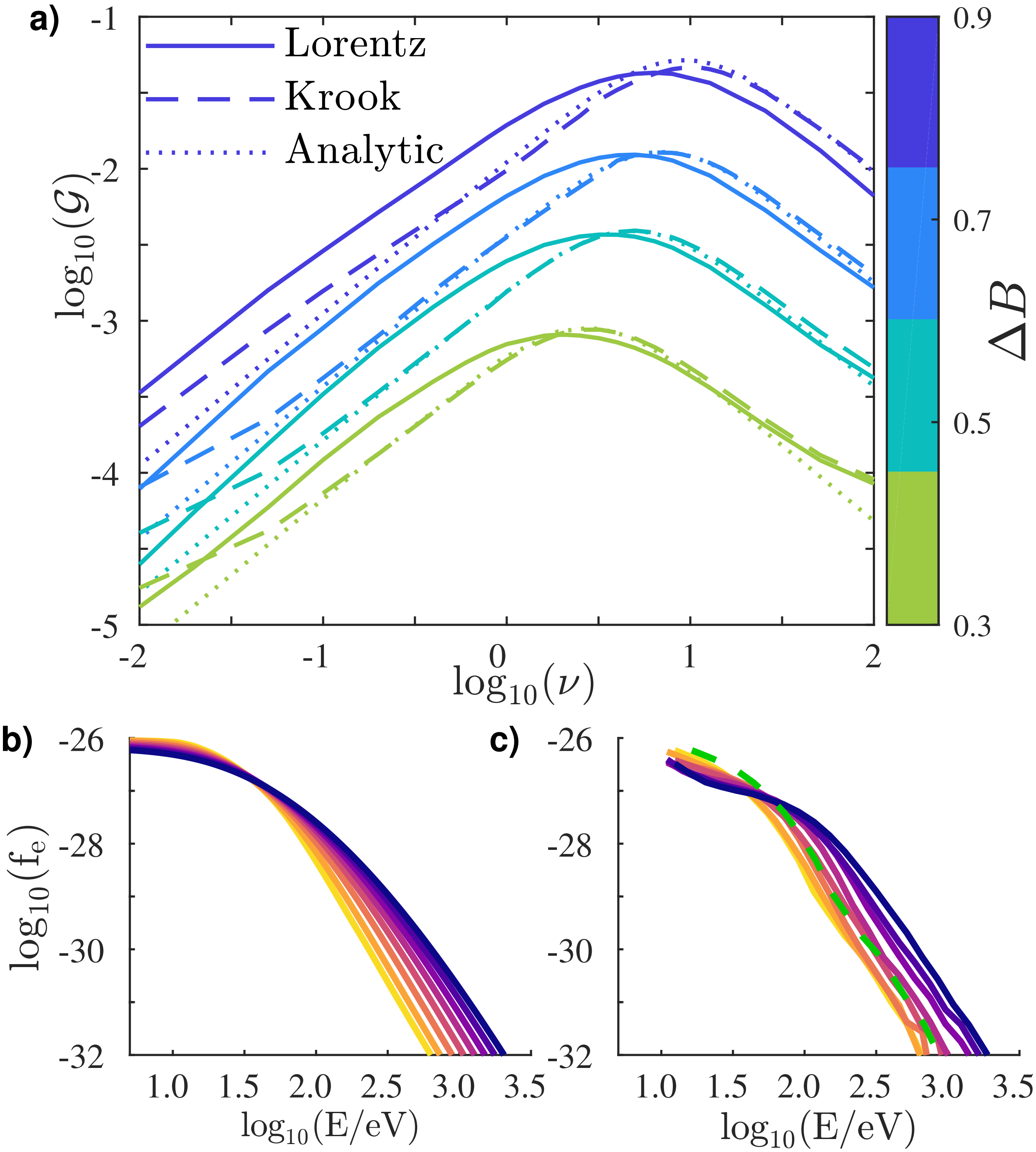

Figure 4.9: **(a)** The energization $\mathcal{G}$ as a function of the amplitude of a fluctuation, $\delta B/B_0$, and the scattering frequency, ν, for the numerically-computed Lorentz (solid) and Krook (dashed) operators, as well as the analytic solution in Eq. 4.16(dotted). **(b)** Combined estimate of the evolution of the distribution function from magnetic pumping and compressional heating for the points denoted in colored lines in Fig. 4.2(a), approximated using the number of fluctuations, $N_{\text{fluctuations}} = 15$, $\delta B/B_0 = 0.7$, and $\nu/(\omega/2\pi) = 0.75$. **(c)** Reproduction of Fig. 4.2(e).

distribution is computed using Eq. 4.12.

Numerical values of $\mathcal{G}$ in Eq. 4.16 are estimated through Eq. 4.17, where $T = 2\pi/\omega$ and the numerator and denominator are found to be nearly linearly dependent functions of v before averaging,

$$\mathcal{G}_{\text{estimate}} = \left\langle \frac{\left(\int_0^T (\partial f/\partial t)dt\right)/T}{\frac{1}{v^2}\frac{\partial}{\partial v}\left(v^4 \frac{\partial f}{\partial v}\right)} \right\rangle_v . \tag{4.17}$$

In Fig. 4.9(a), the numerical model of Eq. 4.5 is evaluated both with the full Lorentz operator and its Krook approximation, and demonstrates good agreement with Eq. 4.16.

Using the estimated parameters for the MMS event shown in Fig. 4.2, including an estimate for the overall amount of compressional heating, we apply the model in Eqs. 4.1 and 4.16 to predict the evolution of the pitch-angle-averaged distributions recorded by MMS. The result of this calculation is shown in Fig. 4.9(b) and is in good agreement with the observation from Fig. 4.2(e), repeated for convenience in Fig. 4.9(c). While there are some differences at lower energies, likely due to the effects of electric fields, which are neglected in our approach, the model provides a good account for the energization of electrons at moderate to superthermal energies, $\mathcal{E} > 100$ eV.

4.4 Conclusions

We have here presented a heating mechanism, magnetic pumping, that becomes applicable to superthermal particles, $v \gg \omega/k$, when the affects of trapping are incorporated into the model. The application of the pumping model to MMS observations provides evidence that magnetic pumping has a significant role in electron energization in the region of the Earth's bow shock. Given the potential universal applicability of the model, this could have a far-reaching impact on our understanding of electron and superthermal ion energization in many other plasma environments where particles with $v \gg \omega/k$ are observed, such as the solar corona, cosmic ray generation pumped by magnetic turbulence in the interstellar medium, or shocks driven by supernova explosions.

Chapter 5

2D Pumping Derivations

In this section we will go through the derivation of the equation for the background evolution of the 2D magnetic pumping model. Before we get into the details of the derivation we want to go through some background on the method that this result relies on, the multiple-time-scale perturbation analysis method[1].

5.1 Multiple-Time-Scale Perturbation Analysis

The multiple-time-scale perturbation analysis method is a technique that leverages the fact that different processes happen on dramatically different time scales to construct a solution to a perturbation problem. Following the example of Davidson [31], we can go through a description of what happens fundamentally in such an analysis. In a conventional perturbation analysis, we expand the variable of interest, $x(t)$ in terms of a small-amplitude parameter, ϵ, where $0 < \epsilon \ll 1$, such that

$$x \simeq x^{(0)} + \epsilon x^{(1)} + \epsilon^2 x^{(2)} + \ldots \quad . \tag{5.1}$$

[1] This method is also referred to as the multiple scale analysis. It is used in many contexts beyond plasma physics and is analogous to time-dependent perturbation theory in quantum mechanics[31, 69].

For certain analyses there is a great disparity between the time scale of different physical processes, such as the characteristic time of the linear growth rate of an instability when compared to the timescale of an oscillation in the plasma. For the moment we will refrain from committing to a particular physical system, but to incorporate the time-disparity between these processes, whatever they may be, we extend the number of time variables from one variable, t, to many independent time variables τ_0, τ_1, τ_2, ..., where

$$\frac{d\tau_0}{dt} = 1, \qquad \frac{d\tau_1}{dt} = \epsilon, \qquad \frac{d\tau_2}{dt} = \epsilon^2, \tag{5.2}$$

and the expansion of our relevant parameters take the form

$$x \simeq x^{(0)}(\tau_0, \tau_1, \tau_2, ...) + \epsilon x^{(1)}(\tau_0, \tau_1, \tau_2, ...) + \epsilon^2 x^{(2)}(\tau_0, \tau_1, \tau_2, ...) + ... \quad . \tag{5.3}$$

Since we are treating τ_0, τ_1, τ_2, ... as independent variables the time derivatives are also expanded as

$$\frac{d}{dt} = \frac{\partial}{\partial \tau_0} + \epsilon \frac{\partial}{\partial \tau_1} + \epsilon^2 \frac{\partial}{\partial \tau_2} + ... \quad . \tag{5.4}$$

The coefficients of successive powers of ϵ are collected to obtain a set of coupled differential equations.

The new variables $x^{(0)}(\tau_0, \tau_1, ...)$, $x^{(1)}(\tau_0, \tau_1, ...)$, ... , are 'generalized' solutions, which include both physical and unphysical solutions. Specifically there solutions included that have time secularities, where the parameter of interest steadily increases in time, violating physical constraints like energy conservation. However, the additional time variables allow us the freedom to remove these unphysical solutions, a feature that is not present in conventional perturbation analysis. Removing these time secularities puts constraints on the perturbation solution, called solvability conditions.

After the solution is obtained to the desired order of accuracy we can return to the physical time variable, t, and make the replacements

$$\tau_0 = t, \qquad \tau_1 = \epsilon t, \qquad \tau_2 = \epsilon^2 t, \qquad \dots \quad . \tag{5.5}$$

This method can provide solutions to perturbation problems that conventional perturbation theory cannot solve. For example, in the solution to the Van der Pol equation, conventional perturbation analysis must include infinite terms to obtain the correct the solution, whereas with multiple-time-scale perturbation analysis it is only necessary to expand to the first order, τ_1 to recover the correct solution.

5.2 Jean's Theorem

For the derivation of the 2D magnetic pumping result it is helpful to briefly consider the Boltzmann equation, as this equation is at the core of the analysis. Fundamentally, the Boltzmann equation describes the statistical behavior of a thermodynamic system not in a state of equilibrium, the latter part of the definition being an key point in applying this equation to collisionless space and astrophysical plasmas systems, such as the solar wind. The general statement of this equation is

$$\frac{df}{dt} = \left(\frac{\partial f}{\partial t}\right)_{\text{coll}} \tag{5.6}$$

where $f = f(\mathbf{x}, \mathbf{v}, t)$ is the probability density function, defined such that $dN = f(\mathbf{x}, \mathbf{v}, t)d^3\mathbf{x}d^3\mathbf{v}$ is the total number of particles that have positions within a volume element $d^3\mathbf{x}$ around the position vector $\mathbf{x}$ that have momenta within the momentum space element $d^3\mathbf{v}$ of momenta $\mathbf{v}$ at time t. The term on the right-hand side accounts for the effects of forces acting between the particles in the form of collisions.

Jean's theorem states that any steady-state solution of the collisionless Boltzmann equation depends on the phase-space coordinates only through the integrals of motion in the given potential, and conversely any function of the integrals of motion is a steady-state solution. An integral of motion is any function of only phase-space coordinates that are constant along an orbit, *i.e.* some function $I(\mathbf{x}, \mathbf{v})$ such that

$$\frac{d}{dt}\left[I(\mathbf{x}(t), \mathbf{v}(t))\right] = 0 \tag{5.7}$$

along all orbits[2]. We can see Jean's theorem directly by constructing some function, f, that is a function of only the n integrals of motion, for which we can see

$$\frac{d}{dt}\left[f(I_1(\mathbf{x}, \mathbf{v}), I_2(\mathbf{x}, \mathbf{v}), ..., I_n(\mathbf{x}, \mathbf{v}))\right] = \sum_{m=1}^{n} \frac{dI_m}{dt}\frac{\partial f}{\partial I_m} = \sum_{m=1}^{n}(0)\frac{\partial f}{\partial I_m} = 0 \tag{5.8}$$

so f satisfies the steady-state collisionless Boltzmann equation.

To get a better sense of the underlying physics of the Boltzmann equation, and how it explicitly relates to the kinetic equation in plasma physics, it is helpful to review the theoretical foundation of these equations. To do this we will begin with the Klimontovich formalism, which describes the space-time evolution of the microscopic distribution function in 6N dimensional phase space, where N is the total number of particles, then move to an ensemble-averaged distribution function. This will allows us to make a connection to the six-dimensional standard form of the kinetic equation, *i.e.*

$$\frac{\partial f_s}{\partial t} + \mathbf{v}\cdot\frac{\partial f_s}{\partial \mathbf{x}} + \frac{q_s}{m_s}\left(\mathbf{E} + \mathbf{v}\times\mathbf{B}\right)\cdot\frac{\partial f_s}{\partial \mathbf{v}} = \left(\frac{\partial f_s}{\partial t}\right)_{\text{coll}} \quad , \tag{5.9}$$

where the subscript s is due to the fact that we have multiple species in our plasmas and $(\partial f_s/\partial t)_{\text{coll}}$ represents the effects of collisions.

We start with the Klimontovich distribution[3] and the Klimontovich equation. We consider

[2]We note that every integral of motion is a constant of motion, but not every constant of motion is an integral of motion. A common example of this is a particle moving in a circular orbit in a spherical potential. The azimuthal speed will be of the form $\psi = \Omega t + \psi_0$, where $C(\psi, t) = t - \psi/\Omega$ will be a constant of motion, but not an integral of motion because of its explicit dependence on time.

[3]Some statistical mechanics textbooks start with the Gibbs ensemble instead of the Klimontovich distribution. The primary difference being the Klimontovich distribution consists of N points in six-dimensional space, while the Gibbs ensemble is a single point in the 6N dimensional phase space. However,

a system of N particles in a box of volume V in a six-dimensional phase space of the position $\mathbf{x}$ and the velocity $\mathbf{v}$, where the phase state vector for the ith particle is written as

$$\mathbf{X}_i = (\mathbf{x}_i(t), \mathbf{v}_i(t)) \quad . \tag{5.10}$$

The exact single particle phase space density is then a summation of six-dimensional delta functions,

$$f_{\text{exact}} = \sum_i \delta\left[\mathbf{X} - \mathbf{X}_i(t)\right] \quad , \tag{5.11}$$

where $X = (\mathbf{x}, \mathbf{v})$. f_{exact} is what is known as the Klimontovich distribution function. From the property of delta functions we can directly calculate the total time derivative of f_{exact}

$$\frac{\partial f_{\text{exact}}}{\partial t} = \frac{\partial}{\partial t}\sum_i \delta\left[\mathbf{X} - \mathbf{X}_i(t)\right] = -\sum_i \left(\frac{d\mathbf{X}_i}{dt} \cdot \frac{\partial}{\partial \mathbf{X}_i}\right)\delta\left[\mathbf{X} - \mathbf{X}_i(t)\right] = -\dot{\mathbf{X}} \cdot \frac{\partial f_{\text{exact}}}{\partial \mathbf{X}} \tag{5.12}$$

so we can see that f_{exact} satisfies the continuity equation in phase space

$$\frac{\partial f_{\text{exact}}}{\partial t} + \dot{\mathbf{X}} \cdot \frac{\partial f_{\text{exact}}}{\partial \mathbf{X}} = 0 \quad , \tag{5.13}$$

which is a shorthand notation for Hamilton's equations of motions for the N individual particles[70]. Changing our variable back to $\mathbf{x}$ and $\mathbf{v}$ and using the fact that the motion of the ith particle is governed by the Lorentz force,

$$\frac{d\mathbf{x}_i}{dt} = \mathbf{v}_i \tag{5.14}$$

$$\frac{d\mathbf{v}_i}{dt} = \frac{q_i}{m_i}\left[\mathbf{E}(\mathbf{x}_i, t) + \mathbf{v}_i \times \mathbf{B}(\mathbf{x}_i, t)\right] \quad , \tag{5.15}$$

we obtain the standard form of the Klimontovich equation,

$$\frac{df_{\text{exact}}}{dt} = \frac{\partial f_{\text{exact}}}{\partial t} + \mathbf{v} \cdot \frac{\partial f_{\text{exact}}}{\partial \mathbf{x}} + \frac{q}{m}\left[\mathbf{E}(\mathbf{x}, t) + \mathbf{v} \times \mathbf{B}(\mathbf{x}, t)\right] \cdot \frac{\partial f_{\text{exact}}}{\partial \mathbf{v}} = 0 \quad . \tag{5.16}$$

they encapsulate the same essential idea.

The solutions of the Klimontovich equation can be found by the method of characteristics, where the the characteristics correspond to the particle trajectories. It is clear that these trajectories depend on the electric and magnetic fields in the plasma, which can be thought of consisting of a combination of external fields and those produced self-consistently by the microscopic fine-grained distribution, *i.e.*

$$\mathbf{E}(\mathbf{x}, t) = \mathbf{E}_{\mathrm{ext}}(\mathbf{x}, t) + \mathbf{e}(\mathbf{x}, t) \tag{5.17}$$

$$\mathbf{B}(\mathbf{x}, t) = \mathbf{B}_{\mathrm{ext}}(\mathbf{x}, t) + \mathbf{b}(\mathbf{x}, t) \tag{5.18}$$

where $\mathbf{e}$ and $\mathbf{b}$ are determined from Maxwell's equations.

This equation shows that the distribution function, f_{exact}, is constant along the particle trajectories. While this solution is exact, it is not a practical form to use. Solving for the trajectories of the Klimontovich equation is equivalent to finding the exact trajectories of all N particles in a plasma, essentially the function of a PIC code, when combined with the electric and magnetic fields. In order to overcome this problem it is useful to replace f_{exact}, a singular, discontinuous function, with a smooth, continuous differentiable function. To make this transition we introduce a distribution function that is averaged over an ensemble of identical copies of the original system, called the phase-space averaged distribution function,

$$f_s(\mathbf{x}, \mathbf{v}, t) = \langle f_{\mathrm{exact}}(\mathbf{x}, \mathrm{v}, t) \rangle \quad . \tag{5.19}$$

This can also be interpreted as the number of particles in a given volume of phase space, i.e.

$$f_s(\mathbf{x}, \mathbf{v}, t) = \frac{\int \int_{\Delta\Omega} f_{\mathrm{exact}}(\mathbf{x}, \mathbf{v}, t) d\Omega}{\Delta\Omega} \quad , \tag{5.20}$$

where $\Delta\Omega = \Delta x \Delta y \Delta z \Delta v_x \Delta v_y \Delta v_z$. We then write the exact functions and fields in terms of the ensemble-averaged distribution functions and fields, where the terms of the form δg are referred to as the fluctuations,

$$f_{\text{exact}} = f_s + \delta f_{\text{exact}} \tag{5.21}$$

$$\mathbf{E}^m = \mathbf{E} + \delta\mathbf{E}^m \tag{5.22}$$

$$\mathbf{B}^m = \mathbf{B} + \delta\mathbf{B}^m \tag{5.23}$$

where $\langle \delta f_{\text{exact}} \rangle = \langle \delta\mathbf{E}^m \rangle = \langle \delta\mathbf{B}^m \rangle = 0$, so $E = \langle \mathbf{E}^m \rangle$ and $B = \langle \mathbf{B}^m \rangle$. Using these new definitions, with the Klimontovich equation given in Eq. 5.16, we obtain the expression[4]

$$\frac{\partial f_s}{\partial t} + \mathbf{v} \cdot \frac{\partial f_s}{\partial \mathbf{x}} + \frac{q_s}{m_s}\left(\mathbf{E} + \mathbf{v} \times \mathbf{B}\right) \cdot \frac{\partial f_s}{\partial \mathbf{v}} = -\frac{q_s}{m_s}\left\langle \left(\delta\mathbf{E}^m + \mathbf{v} \times \delta\mathbf{B}^m\right) \cdot \frac{\partial \delta f_{\text{exact}}}{\partial \mathbf{v}} \right\rangle \tag{5.24}$$

which can also be written as

$$\frac{df_s}{dt} = \left(\frac{\partial f_s}{\partial t}\right)_{\text{coll}} \quad . \tag{5.25}$$

We note that the left-hand side of the equation corresponds to the large-scale, collective effects and the right-hand side corresponds to the effects of collisions. In the limit of low collisionality, $(\partial f_s/\partial t)_{\text{coll}} \to 0$ we recover the Vlasov equation,

$$\frac{\partial f_s}{\partial t} + \mathbf{v} \cdot \frac{\partial f_s}{\partial \mathbf{x}} + \frac{q_s}{m_s}\left(\mathbf{E} + \mathbf{v} \times \mathbf{B}\right) \cdot \frac{\partial f_s}{\partial \mathbf{v}} = 0 \quad . \tag{5.26}$$

The Vlasov equation has the form of a Liouville equation for a set of non-interacting particles under the an external field. As discussed earlier, because these field are generated self-consistently from the moments of the distribution of charged particles, this equation is inherently nonlinear.

While the exact nature of the collisional term on the right-hand side of the equation varies between the Boltzmann equation and the kinetic equation derived in this manner, it

[4] There is a more rigorous way of obtaining the plasma kinetic equation, and by extension the Vlasov equation, that involves starting with the Gibbs ensemble, then using the Liouville equation, and finally the BBGKY hierarchy equations. This method better captures the correlations that result in the collisional term, but a thorough derivation is beyond the scope of this thesis. For the interested reader several very accessible derivations are given in [71, 72, 73, 74, 75, 76, 77]

is clear that the equations can be derived from the same first principles, and that Jean's theorem must hold for the plasma kinetic equation as well.

5.3 Jean's Theorem and the Multiple-Time Scale Perturbation Analysis

It turns out that we can recover Jean's theorem using the multiple-time scale perturbation analysis method for a particle trapped in a spatially-varying magnetic field, following the analysis from Davidson[31], Cordey *et al.* [65], and Kolesnichenko *et al.* [78]. Here the fundamental assumption is that the frequency of the bounce motion far exceeds the collision frequency, as well as the time scale for variations in the magnetic field. We define the small expansion parameter, ϵ_p, as the ratio of these two quantities, $\epsilon_p = \tau_b/\tau_*$, where τ_b is the characteristic time of particle motion in the magnetic field, or the bounce time, and τ_* is the characteristic time for particle collisions. For the kinetic equation

$$\frac{df}{dt} = C(f) \equiv \frac{G}{\tau_*} \tag{5.27}$$

we introduce independent time-variables of the form

$$\tau^{(0)} = t/\tau_b \tag{5.28}$$

$$\tau^{(n)} = (\epsilon_p)^n \tau^{(0)}, \qquad \text{where n} = 1, 2, ... \tag{5.29}$$

where the time derivative is of the form

$$\frac{d}{dt} = \frac{1}{\tau_b}\frac{d}{d\tau^{(0)}} + \frac{\epsilon_p}{\tau_b}\frac{d}{d\tau^{(1)}} + ... \tag{5.30}$$

and the distribution function is expanded in terms of these new independent variables and this small parameter

$$f = f_0(\tau^{(0)}, \tau^{(1)}, ...) + \epsilon_p f_1(\tau^{(0)}, \tau^{(1)}, ...) + ... \quad . \tag{5.31}$$

Using these expansion terms, to the lowest order in ϵ_p we obtain the equation

$$\frac{df_0}{d\tau^{(0)}} = 0 \quad . \tag{5.32}$$

This equation can be solved by integrating along it's characteristics, which are the equations for the particle orbits. The characteristics are given by $x = x(\alpha_1, \alpha_2, ..., \alpha_N, t)$, where $\alpha_1, \alpha_2, ..., \alpha_N$ are the integrals of motion. The solution then becomes

$$f_0 = g(\alpha_1, \alpha_2, ..., \alpha_6) \tag{5.33}$$

where g is an arbitrary function. From this form we can see directly that this result, Eq. 5.32 is the equivalent statement to Jean's theorem.

To the next order in ϵ_p we have the equation

$$\frac{df_1}{d\tau^{(0)}} = -\frac{df_0}{d\tau^{(1)}} + G \quad . \tag{5.34}$$

To avoid time secularities, *i.e.* unphysical solutions to the kinetic equation, we have the solvability condition

$$\int_0^{\tau_b} \left(\frac{df_0}{d\tau^{(1)}} - G \right) d\tau^{(0)} = 0 \quad . \tag{5.35}$$

This equation can be expressed as

$$\frac{\partial f_0}{\partial t} = \frac{1}{\tau_*} \int_0^{\tau_b} G \frac{dt}{\tau_b} \quad . \tag{5.36}$$

Eq. 5.36 is equivalent to the step where we orbit average the scattering operator in Eq. 4.5.

We also notice that Eq. 4.5 has an additional $\partial/\partial\mathcal{E}$ term on the left hand side of the equation. This is due to the fact that while $\mathcal{E}$ is a constant of motion during a orbit transit, it is not over the timescale of the pumping cycle. In fact, the energy of each particle oscillates significantly during each pumping cycle.

5.4 2D Magnetic Pumping Derivation

Now that we have used the multiple-time scale perturbation analysis to verify that Jean's theorem is valid in our system, our aim is to provide a derivation of the important result in Eq. 4.16. From the multiple-time scale method we know that the distribution is constant along the instantaneous particle orbits and thus can be expressed in terms of the integrals of motion. We recall from Chapter 4 that these are $\mu = mv_\perp^2/(2B)$ and $\mathcal{E} = \frac{1}{2}mv^2$. While we worked in $f = f(t, \mathcal{E}, \chi)$, where $\chi = (\Lambda)/(j^2 + \Lambda)$, where $j = J/(4vL)$ and $\Lambda = \mu B_0/\mathcal{E}$, we will instead for the purposes of this derivation work in $f = f(t, \mathcal{E}, \Lambda^*)$, where

$$\Lambda^* \equiv \frac{\mu B_0}{\mathcal{E}} \frac{B_{\mathrm{min}}}{B_0} = \Lambda \frac{B_{\mathrm{min}}}{B_0} \quad . \tag{5.37}$$

While the maximum value of Λ changes with time in our sinusoidal perturbation, this new, normalized value of Λ^* has the same maximum value at every timestep, specifically $\Lambda^* \in [0, 1]$. At the end of the chapter, we will switch variables back to the $f = f(t, \mathcal{E}, \chi)$ to connect to our results in Chapter 4.

In these new variables, the kinetic equation is

$$\frac{df}{dt} = \left.\frac{\partial f}{\partial t}\right|_{\Lambda^*, \mathcal{E}} + \frac{d\Lambda^*}{dt}\frac{\partial f}{\partial \Lambda^*} + \frac{d\mathcal{E}}{dt}\frac{\partial f}{\partial \mathcal{E}} = \nu \mathcal{L} f \tag{5.38}$$

We now seek to obtain expressions for the total derivatives, $d\Lambda^*/dt$ and $d\mathcal{E}/dt$. Consider the ratio J^2/μ. This is clearly a constant of motion which has the special property that it is independent of $\mathcal{E}$. Using the normalized action integral, j, we find

$$\frac{d}{dt}\frac{J^2}{\mu} = \frac{d}{dt}\frac{j^2 B_{\text{min}}}{\Lambda^*} = 0 \tag{5.39}$$

such that

$$\frac{2}{j}\frac{dj}{dt} + \frac{1}{B_{\text{min}}}\frac{dB_{\text{min}}}{dt} - \frac{1}{\Lambda^*}\frac{d\Lambda^*}{dt} = 0 \tag{5.40}$$

Our aim is now to obtain an expression for $d\Lambda^*/dt$. To evaluate the total differentials we notice that $j = j(\Lambda^*, t)$, while $B_{\text{min}} = B_{\text{min}}(t)$ and $\Lambda^* = \Lambda^*(t)$. Thus,

$$\frac{dj}{dt} = \frac{\partial j}{\partial t} + \frac{d\Lambda^*}{dt}\frac{\partial j}{\partial \Lambda^*} \quad . \tag{5.41}$$

By then combining Eqs. 5.40 and 5.41 we find

$$\frac{1}{\Lambda^*}\frac{d\Lambda^*}{dt} = \frac{2\frac{\partial j}{\partial t} + 2\frac{j}{B_{\text{min}}}\frac{dB_{\text{min}}}{dt}}{j - 2\Lambda^*\frac{\partial j}{\partial \Lambda^*}} \quad . \tag{5.42}$$

Considering the definition of Λ^* in Eq. 5.37 it follows that

$$\frac{d\Lambda^*}{dt} = -\frac{\Lambda^*}{\mathcal{E}}\frac{d\mathcal{E}}{dt} + \frac{\dot{B}_{\text{min}}}{B_{\text{min}}}\Lambda^* \quad , \tag{5.43}$$

so using Eq. 5.42 we may solve for $d\mathcal{E}/dt$ to find

$$\frac{d\mathcal{E}}{dt} = -g\mathcal{E} \tag{5.44}$$

with

$$\begin{aligned} g(\Lambda^*, t) &= \frac{2\frac{\partial j}{\partial t} + 2\frac{\dot{B}_{\text{min}}}{B_{\text{min}}}\Lambda^*\frac{\partial j}{\partial \Lambda^*}}{j - 2\Lambda^*\frac{\partial j}{\partial \Lambda^*}} \\ &= \frac{2\frac{\partial j}{\partial t} + 2\frac{\dot{B}_{\text{min}}}{B_{\text{min}}}\Lambda^*\frac{\partial j}{\partial \Lambda^*}}{\tilde{\tau}_b} \\ &= \frac{2\frac{\partial j}{\partial t} + \frac{\dot{B}_{\text{min}}}{B_{\text{min}}}(j - \tilde{\tau}_b)}{\tilde{\tau}_b} \quad . \end{aligned} \tag{5.45}$$

This also allows us to write an expression for $d\Lambda^*/dt$, *i.e.*

$$\frac{d\Lambda^*}{dt} = \left(g + \frac{\dot{B}_{\min}}{B_{\min}}\right)\Lambda^* \tag{5.46}$$

Note, to find the above expression for f we used

$$\tilde{\tau}_b = j - 2\Lambda^* \frac{\partial j}{\partial \Lambda^*} \tag{5.47}$$

which is readily shown using

$$\frac{\tau_b}{m} = \left.\frac{\partial J}{\partial \mathcal{E}}\right|_\mu, \quad \left.\frac{\partial}{\partial \mathcal{E}}\right|_\mu = \left.\frac{\partial}{\partial \mathcal{E}}\right|_{\Lambda^*} + 2\Lambda^* \frac{\partial}{\partial \Lambda^*} \quad . \tag{5.48}$$

Combining this all together, the kinetic equation in Eq. 5.38 now becomes:

$$\frac{\partial f}{\partial t} = g\,\mathcal{E}\frac{\partial f}{\partial \mathcal{E}} - \left(g + \frac{\dot{B}_{\min}}{B_{\min}}\right)\Lambda^* \frac{\partial f}{\partial \Lambda^*} + \nu \mathcal{L} f$$

or

$$\frac{\partial f}{\partial t} = g\,\frac{v}{2}\frac{\partial f}{\partial v} - \left(g + \frac{\dot{B}_{\min}}{B_{\min}}\right)\Lambda^* \frac{\partial f}{\partial \Lambda^*} + \nu \mathcal{L} f \quad . \tag{5.49}$$

5.4.1 Krook approximation for the scattering operator

Ideally, at this point we would use a quasilinear-like analysis as we did in Chapter 3 to find the evolution equation of the background distribution. Unfortunately, the Legendre polynomials are no longer good eigenfunctions of this equation with the inclusion of trapping along the flux tube, so the analysis in Chapter 3 cannot be directly repeated. While it may be possible to find good eigenvalues of this equation with the Lorentz scattering operator and solve for the slowly-varying background distribution, we were unable to solve this equation directly.

However, we were able to find an approximation to the Lorentz scattering operator, the

Krook operator,

$$\mathcal{L}_K f = -C_K \left(f - \frac{\langle f \rangle_\Lambda}{\langle 1 \rangle_\Lambda} \right) \quad , \tag{5.50}$$

where C_K is the Krook coefficient that we discussed in detail in Chapter 4. We note that this scattering operator is the same as the one given in Eq. 4.11, although it appears to be different. The different appearance is due to the fact that in Chapter 4 we were using the normalized version of the distribution function. Throughout this Chapter, we will be using the unnormalized version of the averaging over pitch-angle. More specifically, the averaging operator we will be using throughout this chapter is given by the expression

$$\langle (\dots) \rangle_\Lambda = \int d\Lambda^* \frac{B_0}{B_{\min}} \tilde{\tau}_b (\dots) \quad . \tag{5.51}$$

By using this approximation in place of the Lorentz scattering operator we were able to find an equation for the slowly-varying background distribution function. As we mentioned in Chapter 4, this is a much simpler scattering operator than the Lorentz scattering operator. Unlike the Lorentz operator, it does not scatter sharper features in phase-space more efficiently. As can be seen from the form of Eq. 5.50 and the analysis in Chapter 4, the Krook operator can be thought of as a linear combination of the full distribution function, f and the fully isotropized distribution function, $\langle f \rangle_\Lambda / \langle 1 \rangle_\Lambda$. We note that $\mathcal{L}_K f$ conserves particles and if the anisotropy in f were of the form $P_2(v_\parallel / v)$, which it is not because of the additional phase-space structure coming from the trapping, $\mathcal{L}_K f$ would yield an exact result.

In the remainder of this chapter we will find the equation for the evolution of the slowly-varying background distribution and show that this equation conserves particles. We will first do this in the limit where $\nu/\omega \gg 1$, and then for the case without restrictions on ν/ω. This will ultimately yield the result in Eq. 4.16.

5.4.2 Variables and Assumptions

We know that the number of particles in our system, *i.e.*

$$N = \int f d^3v d^3x = \frac{2\pi\,\Delta y}{m^2} \int d\mathcal{E} \int d\mu \int d\Psi \tau_b f \tag{5.52}$$

is conserved. Assuming that we have a sinusoidal magnetic field perturbation such that for $x = L/2$ we have $B = B_0$, and evaluating the width Δz of the flux tube at this location, we find that $\Delta\Psi = B_0 \Delta z$. We use this expression, as well as our definitions from before, $\tilde{\tau}_b = v\tau_b/(4L)$ and $d\mathcal{E} d\mu = m^2 v^3\, dv\, d\Lambda/B_0$ to rewrite the particle conservation statement as

$$N = 2\pi \Delta y \Delta z L \int v^2 dv \int d\Lambda^* \frac{B_0}{B_{\min}} \tilde{\tau}_b f \quad . \tag{5.53}$$

Guided by Eq. 5.53 we define the averaging operator as in Eq. 5.51 and define

$$F(v) = \langle f \rangle_\Lambda \tag{5.54}$$

such that

$$N = 2\pi \Delta y \Delta z L \int F v^2 dv \tag{5.55}$$

where it is clear that $Fv^2 dv$ is proportional to the number of particles of the entire flux-tube within a differential velocity interval dv.

Using these newly defined variables and averaging operators, we split f into its isotropic and non-isotropic parts

$$f = f_0(t, v) + f_1(t, v, \Lambda^*) \quad , \tag{5.56}$$

where

$$f_0 = \frac{\langle f \rangle_\Lambda}{\langle 1 \rangle_\Lambda} = \frac{1}{\langle 1 \rangle_\Lambda} F(v) \quad . \tag{5.57}$$

5.4.3 Extreme ordering of $\nu \gg \omega$

Using our newly defined variables, we can start the process of deriving an expression for $\partial F/\partial t$, or the evolution of F due to magnetic pumping. Inserting $f = f_0 + f_1$ back into Eq. 5.49 we obtain the equation

$$\frac{\partial f}{\partial t} = g\frac{v}{2}\frac{\partial(f_0 + f_1)}{\partial v} - \left(g + \frac{\dot{B}_{\text{min}}}{B_{\text{min}}}\right)\Lambda^* \frac{\partial f_1}{\partial \Lambda^*} - \nu\mathcal{L}_K f \quad . \tag{5.58}$$

Throughout this analysis we will use the fact that $\langle f_1 \rangle_\Lambda = 0$ and that $\langle k f_0 \rangle_\Lambda = f_0 \langle k \rangle_\Lambda$. We can evaluate the expression for the scattering operator,

$$\nu\mathcal{L}_K f = \nu\mathcal{L}_k(f_0 + f_1) = -C_K\nu\left(f_0 + f_1 - \frac{\langle f \rangle_\Lambda}{\langle 1 \rangle_\Lambda}\right) = -C_K\nu f_1 \quad . \tag{5.59}$$

Using Eq. 5.58 and taking the difference between $\partial f/\partial t$ and $\langle \partial f/\partial t \rangle_\Lambda$, and assuming a small amplitude ordering $|g| \simeq |f_1| \ll |f_0|$, then we obtain approximate equation for f_1

$$\frac{\partial f_1}{\partial t} = h\frac{v}{2}\frac{\partial f_0}{\partial v} + \nu\mathcal{L}_K f_1 \quad , \tag{5.60}$$

where $h = g - (\langle g \rangle / \langle 1 \rangle_\Lambda)$.

Up until this point we have not made any assumptions of the scattering frequency as compared to the fluctuation frequency, ν/ω. At this point we can introduce the extreme ordering $\nu/\omega \gg 1$, which causes Eq. 5.60 to reduces to

$$0 = h\frac{v}{2}\frac{\partial f_0}{\partial v} - C_K\nu f_1 \quad , \tag{5.61}$$

such that

$$f_1 = \frac{h}{C_K\nu}\frac{v}{2}\frac{\partial f_0}{\partial v} \quad . \tag{5.62}$$

Our aim is to derive an equation for $\partial F/\partial t$ which describes the evolution of $F(v)$ due to magnetic pumping. So we start with the expression for $\partial F/\partial t$

$$\begin{aligned}\frac{\partial F}{\partial t} &= \int d\Lambda^* \left[\frac{B_0}{B_{\min}}\,\tilde{\tau}_b \frac{\partial f}{\partial t} + f\,\frac{\partial}{\partial t}\left(\frac{B_0}{B_{\min}}\,\tilde{\tau}_b\right)\right] \\ &= \left\langle \frac{\partial f}{\partial t}\right\rangle_\Lambda + \int d\Lambda^* f \frac{\partial}{\partial t}\left(\frac{B_0}{B_{\min}}\tilde{\tau}_b\right) \\ &= \left\langle \frac{\partial f}{\partial t}\right\rangle_\Lambda + \int d\Lambda^* f_0 \frac{\partial}{\partial t}\left(\frac{B_0}{B_{\min}}\tilde{\tau}_b\right) + \int d\Lambda^* f_1 \frac{\partial}{\partial t}\left(\frac{B_0}{B_{\min}}\tilde{\tau}_b\right) \\ &= \left\langle \frac{\partial f}{\partial t}\right\rangle_\Lambda + f_0 \int d\Lambda^* \frac{\partial}{\partial t}\left(\frac{B_0}{B_{\min}}\tilde{\tau}_b\right) + \left\langle f_1 \frac{\dot{B}_{\min}}{B_{\min}}\right\rangle_\Lambda + \int d\Lambda^* f_1 \frac{B_0}{B_{\min}}\frac{\partial \tilde{\tau}_b}{\partial t} \\ \frac{\partial F}{\partial t} &= \left\langle \frac{\partial f}{\partial t}\right\rangle_\Lambda + f_0 \int d\Lambda^* \frac{\partial}{\partial t}\left(\frac{B_0}{B_{\min}}\tilde{\tau}_b\right) + \int d\Lambda^* f_1 \frac{B_0}{B_{\min}}\frac{\partial \tilde{\tau}_b}{\partial t} \quad , \end{aligned} \tag{5.63}$$

and evaluate the terms on the right hand side.

We start with the $\langle \partial f/\partial t\rangle_\Lambda$ term, beginning with Eq. 5.49 and inserting our expression for f_1 in Eq. 5.62.

$$\begin{aligned}\left\langle \frac{\partial f}{\partial t}\right\rangle_\Lambda = \langle g\rangle_\Lambda \frac{v}{2}\frac{\partial}{\partial v} f_0 + \frac{1}{C_K \nu}\langle gh\rangle_\Lambda \frac{v}{2}\frac{\partial}{\partial v}\frac{v}{2}\frac{\partial}{\partial v} f_0 \\ - \frac{1}{C_K \nu}\left\langle \left(g + \frac{\dot{B}_{\min}}{B_{\min}}\right)\Lambda^* \frac{\partial h}{\partial \Lambda^*}\right\rangle_\Lambda \frac{v}{2}\frac{\partial}{\partial v} f_0 \end{aligned} \tag{5.64}$$

Plugging this result back into Eq. 5.63 we obtain the expression

$$\begin{aligned}\frac{\partial F}{\partial t} = \langle g\rangle_\Lambda \frac{v}{2}\frac{\partial}{\partial v} f_0 + \frac{1}{C_K \nu}\langle gh\rangle_\Lambda \frac{v}{2}\frac{\partial}{\partial v}\frac{v}{2}\frac{\partial}{\partial v} f_0 \\ - \frac{1}{C_K \nu}\left\langle \left(g + \frac{\dot{B}_{\min}}{B_{\min}}\right)\Lambda^* \frac{\partial h}{\partial \Lambda^*}\right\rangle_\Lambda \frac{v}{2}\frac{\partial}{\partial v} f_0 + \int d\Lambda^* f_1 \frac{B_0}{B_{\min}}\frac{\partial \tilde{\tau}_b}{\partial t} \\ + f_0 \int d\Lambda^* \frac{\partial}{\partial t}\left(\frac{B_0}{B_{\min}}\tilde{\tau}_b\right) \quad . \end{aligned} \tag{5.65}$$

To rewrite the above equation in a more tractable form we will need to use the relations

$$\frac{3}{2}\langle gh\rangle_\Lambda = -\left\langle \left(g + \frac{\dot{B}_{\min}}{B_{\min}}\right)\Lambda^* \frac{\partial h}{\partial \Lambda^*}\right\rangle_\Lambda + \int \frac{B_0}{B_{\min}} h \frac{\partial \tilde{\tau}_b}{\partial t}\, d\Lambda^* \tag{5.66}$$

$$\frac{3}{2}\langle g\rangle_\Lambda = \int d\Lambda^* \frac{\partial}{\partial t}\left(\frac{B_0}{B_{\min}}\tilde{\tau}_b\right) \quad , \tag{5.67}$$

which we will now prove.

To prove Eqs. 5.66 and 5.67 it is useful to introduce the expression

$$H \equiv 2\tilde{\tau}_b \frac{d\Lambda^*}{dt} = \left(4\frac{\partial j}{\partial t} + 2\frac{\dot{B}_{\min}}{B_{\min}} j\right)\Lambda^* \quad . \tag{5.68}$$

This expression follows directly from Eq. 5.42 and Eq. 5.47. We also note that H is unrelated to the H used in Chapter 4. Here, like $d\Lambda^*/dt$ we have that H vanishes for $\Lambda^* = 0$ and $\Lambda^* = 1$.

We start be considering Eq. 5.67 and using the definition of g in Eq. 5.45, as well as the fact that

$$\frac{\partial}{\partial t}\left(\frac{B_0}{B_{\min}}\tilde{\tau}_b\right) - \frac{B_0}{B_{\min}}\frac{\partial \tilde{\tau}_b}{\partial t} = -\tilde{\tau}_b \frac{B_0}{B_{\min}}\frac{\dot{B}_{\min}}{B_{\min}} \tag{5.69}$$

we can rewrite the expression as

$$\begin{aligned}
\frac{3}{2}\langle g\rangle_\Lambda - \int d\Lambda^* \frac{\partial}{\partial t}\left(\frac{B_0}{B_{\min}}\tilde{\tau}_b\right) &= \frac{1}{2}\langle g\rangle_\Lambda + \langle g\rangle_\Lambda - \int d\Lambda^* \frac{\partial}{\partial t}\left(\frac{B_0}{B_{\min}}\tilde{\tau}_b\right) \\
&= \frac{1}{2}\langle g\rangle_\Lambda + \int d\Lambda^* \frac{B_0}{B_{\min}}\left(2\frac{\partial j}{\partial t} + \frac{\dot{B}_{\min}}{B_{\min}}(j - \tilde{\tau}_b)\right) - \int d\Lambda^* \frac{\partial}{\partial t}\left(\frac{B_0}{B_{\min}}\tilde{\tau}_b\right) \\
&= \frac{1}{2}\langle g\rangle_\Lambda + \int d\Lambda^* \left[-\tilde{\tau}_b \frac{\dot{B}_{\min}}{B_{\min}}\frac{B_0}{B_{\min}} + \frac{B_0}{B_{\min}}\left(2\frac{\partial j}{\partial t} + \frac{\dot{B}_{\min}}{B_{\min}} j\right)\right] \\
&\quad - \int d\Lambda^* \frac{\partial}{\partial t}\left(\frac{B_0}{B_{\min}}\tilde{\tau}_b\right) \\
&= \frac{1}{2}\langle g\rangle_\Lambda + \int d\Lambda^* \frac{B_0}{B_{\min}}\left(-\frac{\partial \tilde{\tau}_b}{\partial t} + 2\frac{\partial j}{\partial t} + \frac{\dot{B}_{\min}}{B_{\min}} j\right) \\
&= \frac{1}{2}\frac{B_0}{B_{\min}}\int d\Lambda^* \left[\left(2\frac{\partial j}{\partial t} + \frac{\dot{B}_{\min}}{B_{\min}}(j - \tilde{\tau}_b)\right) + 2\left(-\frac{\partial \tilde{\tau}_b}{\partial t} + 2\frac{\partial j}{\partial t} + \frac{\dot{B}_{\min}}{B_{\min}} j\right)\right]
\end{aligned}$$

Using Eq. 5.47, $\tilde{\tau}_b = j - 2\Lambda^*(\partial j/\partial\Lambda^*)$, the expression becomes

$$\begin{aligned}
\frac{3}{2}\langle g\rangle_\Lambda - \int d\Lambda^* \frac{\partial}{\partial t}\left(\frac{B_0}{B_{\min}}\tilde{\tau}_b\right) &= \frac{1}{2}\frac{B_0}{B_{\min}}\int d\Lambda^* \left[4\Lambda^* \frac{\partial}{\partial\Lambda^*}\frac{\partial j}{\partial t} + 4\frac{\partial j}{\partial t} + 2\frac{\dot{B}_{\min}}{B_{\min}} j + 2\frac{\dot{B}_{\min}}{B_{\min}}\Lambda^* \frac{\partial j}{\partial\Lambda^*}\right] \\
&= \frac{1}{2}\frac{B_0}{B_{\min}}\int d\Lambda^* \left[\left(4\frac{\partial j}{\partial t} + 2\frac{\dot{B}_{\min}}{B_{\min}} j\right) + \Lambda^* \frac{\partial}{\partial\Lambda^*}\left(4\frac{\partial j}{\partial t} + 2\frac{\dot{B}_{\min}}{B_{\min}} j\right)\right] \\
&= \frac{1}{2}\frac{B_0}{B_{\min}}\int d\Lambda^* \frac{\partial H}{\partial\Lambda^*}
\end{aligned}$$

$$= \frac{1}{2}\frac{B_0}{B_{\rm min}}\left[H|_{\Lambda^*=1} - H|_{\Lambda^*=0}\right]$$
$$= 0 \tag{5.70}$$

We can see that indeed the expression in Eq. 5.66 is valid.

We can do a similar analysis to verify that Eq. 5.67 is true. Using the fact that $d\Lambda^*/dt = \Lambda^*(g + \dot{B}_{\rm min}/B_{\rm min})$, we can rewrite the expression as

$$\begin{aligned}\frac{3}{2}\langle gh\rangle_\Lambda + \left\langle\left(g + \frac{\dot{B}_{\rm min}}{B_{\rm min}}\right)\Lambda^*\frac{\partial h}{\partial \Lambda^*}\right\rangle_\Lambda + \int d\Lambda^*\frac{B_0}{B_{\rm min}}h\frac{\partial \tilde{\tau}_b}{\partial t} \\ = \frac{1}{2}\frac{B_0}{B_{\rm min}}\int d\Lambda^*\left[3\tilde{\tau}_b gh + 2\tilde{\tau}_b\frac{d\Lambda^*}{dt}\frac{\partial h}{\partial \Lambda^*} - 2h\frac{\partial \tilde{\tau}_b}{\partial t}\right]\end{aligned} \tag{5.71}$$

then inserting the definitions from before for first g and then $\tilde{\tau}_b$ we obtain the expression

$$\begin{aligned}&= \frac{1}{2}\frac{B_0}{B_{\rm min}}\int d\Lambda^*\left[3\left(2\frac{\partial j}{\partial t} + \frac{\dot{B}_{\rm min}}{B_{\rm min}}(j - \tilde{\tau}_b)\right)h2\tilde{\tau}_b\frac{d\Lambda^*}{dt}\frac{\partial h}{\partial \Lambda^*} - 2h\frac{\partial \tilde{\tau}_b}{\partial t}\right] \\ &= \frac{1}{2}\frac{B_0}{B_{\rm min}}\int d\Lambda^*\left[3\left(2\frac{\partial j}{\partial t} + \frac{\dot{B}_{\rm min}}{B_{\rm min}}2\Lambda^*\frac{\partial j}{\partial \Lambda^*}\right)h2\tilde{\tau}_b\frac{d\Lambda^*}{dt}\frac{\partial h}{\partial \Lambda^*} - 2h\frac{\partial}{\partial t}\left(j - 2\Lambda^*\frac{\partial j}{\partial \Lambda^*}\right)\right] \\ &= \frac{1}{2}\frac{B_0}{B_{\rm min}}\int d\Lambda^*\left[6h\frac{\partial j}{\partial t} + 6h\frac{\dot{B}_{\rm min}}{B_{\rm min}}\Lambda^*\frac{\partial j}{\partial \Lambda^*} + 2\tilde{\tau}_b\frac{d\Lambda^*}{dt}\frac{\partial h}{\partial \Lambda^*} - 2h\frac{\partial j}{\partial t} + 4h\Lambda^*\frac{\partial}{\partial \Lambda^*}\frac{\partial j}{\partial t}\right].\end{aligned} \tag{5.72}$$

Before proceeding it is useful to note the relation

$$\begin{aligned}\frac{1}{2}\frac{B_0}{B_{\rm min}}\int d\Lambda^* 4h\frac{\dot{B}_{\rm min}}{B_{\rm min}} &= \int d\Lambda^*\frac{B_0}{B_{\rm min}}h\frac{\dot{B}_{\rm min}}{B_{\rm min}}2\Lambda^*\frac{\partial j}{\partial \Lambda^*} \\ &= \int d\Lambda^*\frac{B_0}{B_{\rm min}}h\frac{\dot{B}_{\rm min}}{B_{\rm min}}(j - \tilde{\tau}_b) \\ &= \frac{1}{2}\frac{B_0}{B_{\rm min}}\int d\Lambda^* 2h\frac{\dot{B}_{\rm min}}{B_{\rm min}}j - \frac{\dot{B}_{\rm min}}{B_{\rm min}}\int d\Lambda^*\frac{B_0}{B_{\rm min}}h\tilde{\tau}_b \\ &= \frac{1}{2}\frac{B_0}{B_{\rm min}}\int d\Lambda^* 2h\frac{\dot{B}_{\rm min}}{B_{\rm min}}j - \frac{\dot{B}_{\rm min}}{B_{\rm min}}\langle h\rangle_\Lambda \\ &= \frac{1}{2}\frac{B_0}{B_{\rm min}}\int d\Lambda^* 2h\frac{\dot{B}_{\rm min}}{B_{\rm min}}j \quad .\end{aligned} \tag{5.73}$$

We can plug the above relation into Eq. 5.72 to obtain the expression

$$
\begin{aligned}
&\frac{3}{2}\left\langle gh\right\rangle_\Lambda + \left\langle\left(g+\frac{\dot{B}_{\min}}{B_{\min}}\right)\Lambda^*\frac{\partial h}{\partial\Lambda^*}\right\rangle_\Lambda + \int d\Lambda^*\frac{B_0}{B_{\min}}h\frac{\partial\tilde{\tau}_b}{\partial t} \\
&\qquad = \frac{1}{2}\frac{B_0}{B_{\min}}\int d\Lambda^*\left[4h\frac{\partial j}{\partial t}+2h\frac{\dot{B}_{\min}}{B_{\min}}j+2h\frac{\dot{B}_{\min}}{B_{\min}}\Lambda^*\frac{\partial j}{\partial\Lambda^*}+H\frac{\partial h}{\partial\Lambda^*}+4h\Lambda^*\frac{\partial}{\partial\Lambda^*}\frac{\partial j}{\partial t}\right] \\
&\qquad = \frac{1}{2}\frac{B_0}{B_{\min}}\int d\Lambda^*\left[h\left(\left(4\frac{\partial j}{\partial t}+2\frac{\dot{B}_{\min}}{B_{\min}}j\right)+\Lambda^*\frac{\partial}{\partial\Lambda^*}\left(4\frac{\partial j}{\partial t}+2\frac{\dot{B}_{\min}}{B_{\min}}j\right)\right)+H\frac{\partial h}{\partial\Lambda^*}\right] \\
&\qquad = \frac{1}{2}\frac{B_0}{B_{\min}}\int d\Lambda^*\left[h\frac{\partial H}{\partial\Lambda^*}+H\frac{\partial h}{\partial\Lambda^*}\right] \\
&\qquad = \frac{1}{2}\frac{B_0}{B_{\min}}\int d\Lambda^*\frac{\partial(hH)}{\partial\Lambda^*} \\
&\qquad = 0 \quad ,
\end{aligned}
\tag{5.74}
$$

so we can see that Eq. 5.67 does in fact hold to be true.

To show numerically that Eq. 5.66 is true we define

$$T_1 = \frac{3}{2}\left\langle gh\right\rangle_\Lambda \quad , \tag{5.75}$$

$$T_2 = -\left\langle\left(g+\frac{\dot{B}_{\min}}{B_{\min}}\right)\Lambda^*\frac{\partial h}{\partial\Lambda^*}\right\rangle_\Lambda \quad , \tag{5.76}$$

$$T_3 = \int_0^1\frac{B_0}{B_{\min}}h\frac{\partial\tilde{\tau}_b}{\partial t}\,d\Lambda^* \quad , \tag{5.77}$$

and Fig. 5.1 shows that indeed $T_1 = T_2 + T_3$.

Inserting our newly-verified expressions, Eq. 5.67 and Eq. 5.66, into Eq. 5.65 and using $f_0 = F/\left\langle 1\right\rangle_\Lambda$ we find

$$
\begin{aligned}
\frac{\partial F}{\partial t} &= \left\langle g\right\rangle_\Lambda\frac{v}{2}\frac{\partial f_0}{\partial v}+\frac{1}{C_K\nu}\left\langle gh\right\rangle_\Lambda\frac{v}{2}\frac{\partial}{\partial v}\left(\frac{v}{2}\frac{\partial f_0}{\partial v}\right)+\frac{1}{C_K\nu}\frac{3}{2}\left\langle gh\right\rangle_\Lambda\frac{v}{2}\frac{\partial f_0}{\partial v}+\frac{3}{2}\left\langle g\right\rangle_\Lambda f_0 \\
&= \frac{\left\langle g\right\rangle_\Lambda}{\left\langle 1\right\rangle_\Lambda}\left[\frac{v}{2}\frac{\partial F}{\partial v}+\frac{3}{2}F\right]+\frac{1}{C_K\nu}\frac{\left\langle gh\right\rangle_\Lambda}{\left\langle 1\right\rangle_\Lambda}\left[\frac{v}{2}\frac{\partial}{\partial v}\left(\frac{v}{2}\frac{\partial F}{\partial v}\right)\frac{3}{2}\frac{v}{2}\frac{\partial F}{\partial v}\right]
\end{aligned}
$$

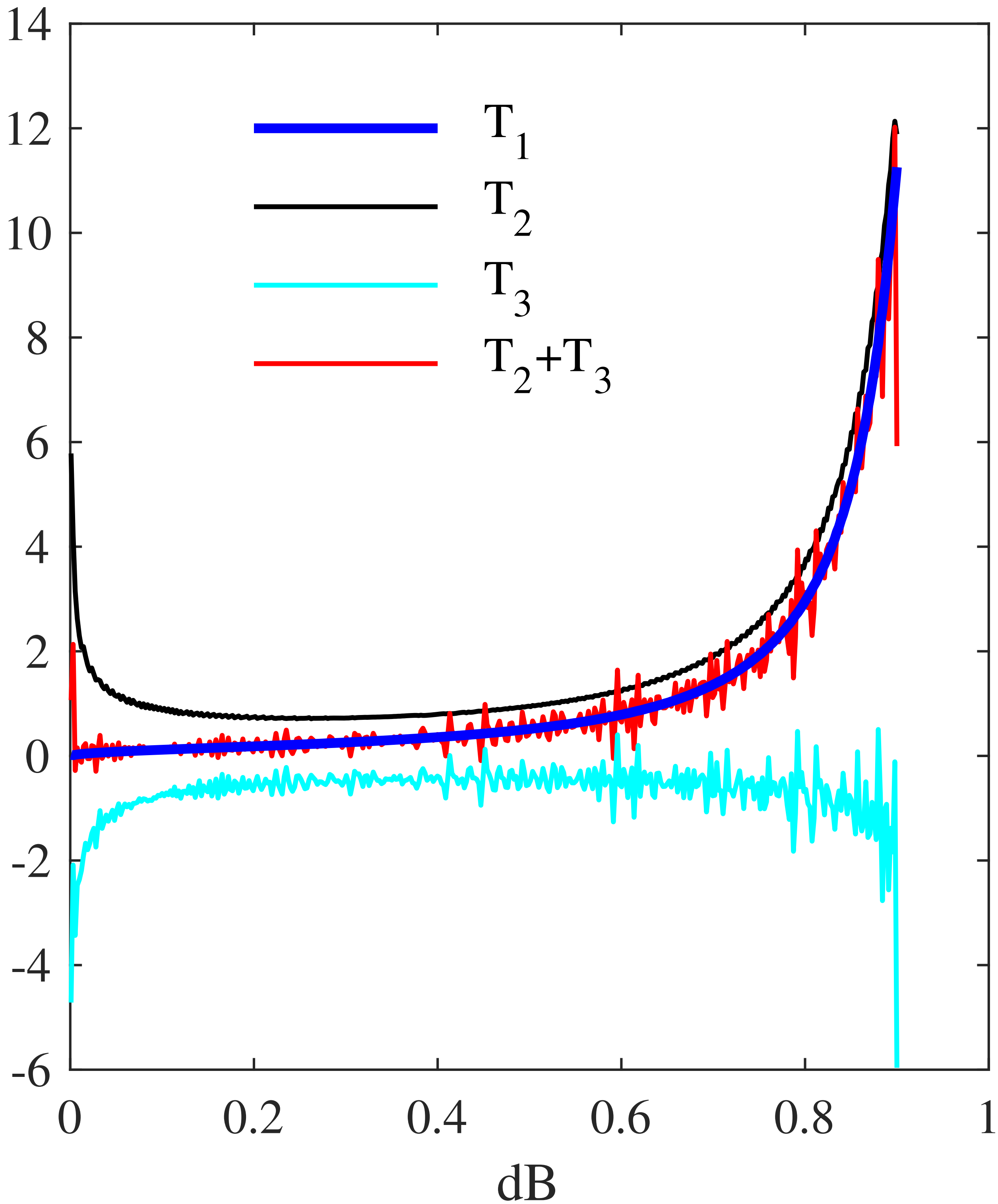

Figure 5.1: Here we have the different terms involved in our density conservation. From the plot it is clear that $T_1 = T_2 + T_3$, and we can see that the relation we verified analytically holds numerically.

which we can then rewrite as

$$\frac{\partial F}{\partial t} = \frac{1}{C_K \nu} \frac{\langle gh \rangle_\Lambda}{\langle 1 \rangle_\Lambda} \frac{1}{4v^2} \frac{\partial}{\partial v} v^4 \frac{\partial}{\partial v} F + \frac{\langle g \rangle_\Lambda}{\langle 1 \rangle_\Lambda} \frac{1}{2v^2} \frac{\partial}{\partial v} v^3 F \quad . \tag{5.78}$$

We can see that the first term on the right hand side corresponds to the energy diffusion, or the heating by magnetic pumping, and the second corresponds to the modifications in F due to compressions and expansions. In the analysis above, we have verified that this form conserves particles at every point in time. However this is also clear from the form of Eq. 5.78. To find the density we integrate the above equation over all velocities, and the left hand side yields $\partial n/\partial t$. Because both terms on the left hand side are of the form $\partial/\partial v(...)$ when we integrate over all velocities and use the fact that as v approaches infinity F approaches zero, we can see that the terms on the right hand side disappear and we get an expression for density conservation.

5.4.4 General Case

Above we solved Eq. 5.60 in the limit $\nu/\omega \gg 1$ to get an approximate solution for f_1. To address the general case with no restrictions on ν/ω we apply Fourier expansions of g, h and f_1

$$g(\Lambda^*, t) = g^1(\Lambda^*)e^{i\omega t} + g^2(\Lambda^*)e^{2i\omega t} + \dots \tag{5.79}$$

$$h(\Lambda^*, t) = h^1(\Lambda^*)e^{i\omega t} + h^2(\Lambda^*)e^{2i\omega t} + \dots$$

$$f_1(\Lambda^*, t) = f_1^1(\Lambda^*)e^{i\omega t} + f_1^2(\Lambda^*)e^{2i\omega t} + \dots$$

Then for the separate frequencies Eq. 5.60 reads

$$in\omega f_1^n = h^n \frac{v}{2} \frac{\partial f_0}{\partial v} - C_K \nu f_1^n$$

such that $f_1 = \sum_n f_1^n$, with

$$f_1^n = K_n \frac{v}{2}\frac{\partial f_0}{\partial v}\,, \quad K_n = \frac{h^n(-in\omega + C_K\nu)}{n^2\omega^2 + (C_K\nu)^2}$$

We may now follow the same steps that led to Eq. 5.78. Furthermore, we find that parts of f_1^n are in phase with g^n causing the time average $\langle\langle g f_1\rangle_\Lambda\rangle_t$ to become finite. An equation for the slow varying component $F_0(v,t)$ is then obtained as

$$\begin{aligned}\frac{\partial F_0}{\partial t} &= \frac{1}{v^2}\frac{\partial}{\partial v}\left(v^2 D\frac{\partial F_0}{\partial t}\right), \qquad D = \omega v^2 \mathcal{G}, \\ \mathcal{G}(\nu/\omega) &= \frac{1}{4}\sum_n \frac{C_K\nu/\omega}{n^2 + (C_K\nu/\omega)^2}\left\langle \frac{\mathrm{Re}(g^n e^{in\omega t})\,\mathrm{Re}(h^n e^{in\omega t})}{\omega^2\,\langle 1\rangle_\Lambda}\right\rangle_t \quad . \end{aligned} \tag{5.80}$$

Finally, while $\langle 1\rangle_\chi$ is not constant during a pump cycle, its periodic variations do not influence the rate of heating and we can introduce the approximation $F_0 = \langle 1\rangle_\chi f_0 \propto f_0$, yielding the form of Eq. 4.16 in Chapter 4.

Chapter 6

Conclusions

This thesis details magnetic pumping as a candidate for heating and power-law generation in a variety of space and astrophysical systems. Analytic work for a model assuming an infinite, uniform flux tube, an extension to this 1D model assuming the presence of thermal streaming, as well as a model that captures the effects of spatial variation along a flux tube, including magnetic trapping, are all detailed in this work. For the first two cases, the model is validated using particle-in-cell simulations. For the 2D case spacecraft observations of the pre-bow-shock region from the MMS mission are used to compare to the results of the analytic model. The key results of the thesis are listed below:

- **In the 1D uniform flux-tube model of magnetic pumping we obtain power-laws and heating that match kinetic simulations.**
- **With the inclusion of some two-dimensional effects magnetic pumping can play a significant role in heating the plasma of the solar wind.** This heating is on par with well-known heating mechanisms such as wave-particle interactions.
- **With the inclusion of magnetic trapping, magnetic pumping can heat particles moving far faster than the wave speed.** This is the most important result of the thesis, as this is a regime in which power-law distributions are observed, but few heating mechanisms are effective.

There are two lines of inquiry for future work on magnetic pumping - better understanding how the magnetic pumping model works under different physical conditions and applying the heating mechanisms to different astrophysical systems. For example, the analysis in Chapter 4 has been done for particles moving fast enough that the $v \times B$ term dominates the electric field, however recent research shows that electric fields in the pre-bow-shock area can play a strong role in heating particles moving at slower velocities[64]. Extending the model to include the effects of trapping in electric fields is one possible avenue of future work. Another promising avenue is examining at the effects of different mechanisms of phase-space-mixing that will be naturally present in space plasmas, such as local trapping arising from the presence of multiple, interacting waves, and the effect that this phase-space mixing will have on the resultant plasma and rate of energization from magnetic pumping, particularly in the case of low scattering, where magnetic pumping is not as effective of a process.

A variety of the different potential astrophysical systems where magnetic pumping could be applied were mentioned in the conclusions to Chapter 4, including explaining heating and power-law generation in . One potential application with particular promise is in using magnetic pumping to explain differential ion heating in the solar corona, the observation that different ion species experience different amounts of heating, an effect which is linearly dependent on their mass[79]. Recent work suggests that there is a zone of preferential heating close to the Sun, and after that point the plasma no longer experiences this preferential heating, but simply evolves with the changing plasma environment [80]. Given the strong, compressional fluctuations present close to the Sun, the plasma environment makes magnetic pumping a potential candidate to explain this heating.

“What we call the beginning is often the end. And to make an end is to make a beginning. The end is where we start from.”

— T.S. Eliot, *Little Gidding*

References

[1] S. Brown and L. Rudnick. Diffuse radio emission in/around the coma cluster: beyond simple accretion. *MNRAS*, 412(1):2–12, 2011.

[2] IceCube Collaboration: M.G. Aartsen et al. Measurement of the cosmic ray energy spectrum with icetop-73. *Physical Review D*, 88(4), 2013.

[3] M. Oka, J. Birn, M. Battaglia, C. C. Chaston, S. M. Hatch, G. Livadiotis, S. Imada, Y. Miyoshi, M. Kuhar, F. Effenberger, E. Eriksson, Y. V. Khotyaintsev, and A. Retinò. Electron power-law spectra in solar and space plasmas. *Space Science Reviews*, 214(5): 82, Jun 2018. ISSN 1572-9672.

[4] J. F. Drake, M. Swisdak, H. Che, and M. A. Shay. Electron acceleration from contracting magnetic islands during reconnection. *Nature*, 443(7111):553–556, OCT 5 2006. ISSN 0028-0836.

[5] C. Kennel and H. Petschek. Limit on stably trapped particle fluxes. *J. Geophys. Res.*, 71(1):1, 1966.

[6] R. E. Ergun, D. Larson, R. P. Lin, J. P. McFadden, C. W. Carlson, K. A. Anderson, L. Muschietti, M. McCarthy, G. K. Parks, H. Reme, J. M. Bosqued, C. D'Uston, T. R. Sanderson, K. P. Wenzel, H. Kaiser, R. P. Lepping, S. D. Bale, P. Kellogg, and J. L. Bougeret. Wind spacecraft observations of solar impulsive electron events associated with solar type III radio bursts. *Astrophys. J.*, 503(1, 1):435–445, AUG 10 1998.

[7] A. F. Vinas, H. K. Wong, and A. J. Klimas. Generation of electron suprathermal tails in the upper solar atmosphere: Implications for coronal heating. *Astrophys. J.*, 528(1): 509–523, JAN 1 2000.

[8] Tongnyeol Rhee, Chang-Mo Ryu, and P.H. Yoon. Self-consistent formation of electron kappa distribution. 2. Further numerical investigation. *Journal of Geophysical Research-Part A-Space Physics*, 111:8 pp., 1 Sept. 2006.

[9] F. Califano and A. Mangeney. A one dimensional, electrostatic Vlasov model for the generation of suprathermal electron tails in solar wind conditions. *J. Geophys. Res.*, 113 (A6), JUN 12 2008.

[10] C. Vocks, C. Salem, R. P. Lin, and G. Mann. Electron halo and strahl formation in the solar wind by resonant interaction with whistler waves. *Astrophys. J.*, 627(1, 1):540–549, JUL 1 2005.

[11] L. B. Wilson, A. Koval, A. Szabo, A. Breneman, C. A. Cattell, K. Goetz, P. J. Kellogg, K. Kersten, J. C. Kasper, B. A. Maruca, and M. Pulupa. Observations of electromagnetic whistler precursors at supercritical interplanetary shocks. *Geophy. Res. Lett.*, 39(8): L08109, APR 2012.

[12] M Oka, L B Wilson Iii, T D Phan, A J Hull, T Amano, M Hoshino, M R Argall, O Le Contel, O Agapitov, D J Gershman, Y V Khotyaintsev, J L Burch, R B Torbert, C Pollock, J C Dorelli, B L Giles, T E Moore, Y Saito, L A Avanov, W Paterson, R E Ergun, R J Strangeway, C T Russell, and P A Lindqvist. Electron Scattering by High-frequency Whistler Waves at Earth's Bow Shock. *The Astrophysical Journal Letters*, 842:L11, 2017.

[13] L. A. Fisk and G. Gloeckler. The common spectrum for accelerated ions in the quiet-time solar wind. *The Astrophysical Journal Letters*, 640(1):L79–L82, MAR 20 2006. ISSN 0004-637X.

[14] L. A. Fisk and G. Gloeckler. Particle Acceleration in the Heliosphere: Implications for Astrophysics. *Space Science Reviews*, 173(1-4):433–458, NOV 2012. ISSN 0038-6308.

[15] G. F. Chew, M. L. Goldberger, and F. E. Low. The boltzmann equation and the one-fluid hydromangetic equations in the absence of particle collisions. *Proc. Royal Soc. A*, 236 (1204):112–118, JULY 1956.

[16] M. W. Kunz, A. A. Schekochihin, S. C. Cowley, J. J. Binney, and J. S. Sanders. A thermally stable heating mechanism for the intracluster medium: turbulence, magnetic fields and plasma instabilities. *Mon. Not. R. Astron. Soc.*, 410(1):2446–2457, 2011.

[17] F. Ley, M. Riquelme, L. Sironi, D. Verscharen, and A. Sandoval. Stochastic ion acceleration by the ion-cyclotron instability in a growing magnetic field. *AJ, Year = 2019, Volume = 880, Number = 2, Pages = 100-115.*

[18] E. Fermi. On the Origin of the Cosmic Radiation. *Physical Review*, 75(8):1169, APR 1949.

[19] H. Alfven. On the solar origin of cosmic radiation ii. *Physical Review*, 77(3):375–379, FEB 1950.

[20] J. E. Borovsky and P. J. Hansen. The magnetic pumping of plasmas with sawtooth waveforms . *Physics of Fluids B: Plasma Physics*, 2(6):1114–1127, 1990.

[21] M. Laroussi and J. R. Roth. Theory of first-order plasma heating by collisional magnetic pumping. *Physics of Fluids*, 1(1):1034, 1989.

[22] J. E. Borovsky and P. J. Hansen. The Contribution of Compressional Magnetic Pumping to the Energization of the Earth's Outer Electron Radiation Belt During High-Speed Stream-Driven Storms. *JGR Space Phyiscs*, 122(12):12,072–12,089, 2017.

[23] J. Egedal, H. Monkhorst, E. Lichko, and P. Montag. Theory of ion dynamics and heating by magnetic pumping in frc plasma. *Phys. Plasmas*, 25(7):072510, 2018.

[24] S.I. Braginskii. Transport processes in a plasma. *Review of Plasma Physics*, 1(1):205–311, 1965.

[25] G. W. Hammett and F. W. Perkins. Fluid moment models for landau damping with application to the ion-temperature-gradient instability. *Physical Review Letters*, 64(25): 3019–3022, JUNE 18 1990. ISSN 00319007.

[26] P.G. Snyder, G.W. Hammett, and W. Dorland. Landau fluid models of collisionless magnetohydrodynamics. *Phys. Plasmas*, 4(11):3974–3985, 1997.

[27] J. Ng, A. Hakim, A. Bhattacharjee, A. Stanier, and W. Daughton. Simulations of anti-parallel reconnection using a nonlocal heat flux closure. *Phys. Plasmas*, 24(8): 082112, 2017.

[28] A. Le, J. Egedal, W. Daughton, W. Fox, and N. Katz. Equations of state for collisionless guide-field reconnection. *Phys. Rev. Lett.*, 102(1):085001, 2009.

[29] J. Egedal, W. Fox, N. Katz, M. Porkolab, M. Oieroset, R. P. Lin, W. Daughton, and J. F. Drake. Evidence and theory for trapped electrons in guide field magnetotail reconnection. *Journal of Geophysical Research Space Physics*, 113(A12):A12207, 2008.

[30] B.A. Wetherton, J. Egedal, A. Le, and W. Daughton. Validation of anisotropic electron fluid closure through *in situ* spacecraft observations of magnetic reconnection. *Geophy. Res. Lett.*, 2019.

[31] R. C. Davidson. *Methods in Nonlinear Plasma Theory.* Academic Press, 1972.

[32] R. M. Kulsrud. *Plasma Physics for Astrophysics.* Princeton University Press, 2005.

[33] K. G. Klein and G. G. Howes. Measuring collisionless damping in heliospheric plasmas using field-particle correlations. *Astrophys. J. Lett.*, 826(2):L30–L35, 2016.

[34] T. H. Stix. *Waves in Plasmas.* Springer-Verlag New York, Inc., 1992.

[35] E. Lichko, J. Egedal, W. Daughton, and J. Kasper. Magnetic Pumping as a Source of Particle Heating and Power-law Distributions in the Solar Wind. *Astrophys. J. Lett.*, 850(2), DEC 1 2017. ISSN 2041-8205.

[36] F. Moreno Cardenas, S. Cristancho Sanchez, and S. Vargas Dominguez. The grand aurorae borealis seen in colombia in 1859. *Advances in Space Research*, 57(1):257–267, 2016.

[37] R. A. Lovett. What if the biggest solar storm on record happened today? *National Geographic News*, MAR 2011.

[38] S. R. Cranmer and A. A. van Ballegooijen. Proton, electron, and ion heating in the fast solar wind from nonlinear coupling between alfvén and fast-mode turbulence. *The Astrophysical Journal*, 754(92):1–29, 2012.

[39] Toppng.

[40] J. F. Drake, M. Swisdak, and R. Fermo. The power-law spectra of energetic particles during multi-island magnetic reconnection. *The Astrophysical Journal Letters*, 763(1): , JAN 20 2013. ISSN 2041-8205.

[41] K. J. Bowers, B. J. Albright, L. Yin, W. Daughton, V. Roytershteyn, B. Bergen, and T. J. T. Kwan. Advances in petascale kinetic plasma simulation with VPIC and Roadrunner. *Journal of Physics: Conference Series*, 180(1):012055, 2009.

[42] W. Daughton, V. Roytershteyn, B. J. Albright, H. Karimabadi, L. Yin, and Kevin J. Bowers. Influence of Coulomb collisions on the structure of reconnection layers. *Physics of Plasmas*, 16(7):072117, july 2009.

[43] K. J. Bowers, B. J. Albright, L. Yin, B. Bergen, and T. J. T. Kwan. Ultrahigh performance three-dimensional electromagnetic relativistic kinetic plasma simulation. *Phys. Plasmas*, 15(5):055703, 2008.

[44] T. Takizuka and H. Abe. A Binary Collision Model for Plasma Simulation with a Particle Code. *Journal of Computational Physics*, 25(3):205–219, may 1977.

[45] W. Daughton, V. Roytershteyn, B. J. Albright, H. Karimabadi, L. Yin, and Kevin J. Bowers. Advances in petascale kinetic plasma simulation with VPIC and Roadrunner. *Physical Review Letters*, 103(1):065004, aug 2009.

[46] C. H. K. Chen. Recent progress in astrophysical plasma turbulence from solar wind observations. *Journal of Plasma Physics*, 82(6):1–28, NOV 2016.

[47] A. Achterberg. On the nature of small amplitude fermi acceleration. *Astronomy and Astrophysics*, 97(2):259–264, APR 1981.

[48] J. W. Lynn, E. Quataert, B. D. G. Chandran, and I. J. Parrish. The efficiency of second-order fermi acceleration by weakly compressible magnetohydrodynamic turbulence. *The Astrophysical Journal*, 777(2):128, OCT 2013.

[49] C. W. Leamon, R. J.and Smith, N. F. Ness, W. H. Matthaeus, and H. K. Wong. Observational constraints on the dynamics of the interplanetary magnetic field dissipation range. *JOURNAL OF GEOPHYSICAL RESEARCH*, 103(A3):4775–4787, MAR 1998.

[50] L. B. Wilson III, D. G. Sibeck, A. W. Breneman, O. Le Contel, C. Cully, D. L. Turner, V. Angelopoulos, and D. M. Malaspina. Quantified energy dissipation rates in the terrestrial bow shock: 2. waves and dissipation. *Journal of Geophysical Research: Space Physics*, 119(8):6475–6495.

[51] A.F. Alexandrov, L.S. Bogdankeich, and A.A. Rukhadze. *Principles of Plasma Electrodynamics*. Springer, 1984.

[52] G. G. Howes, W. Dorland, S. C. Cowley, G. W. Hammett, E. Quataert, A. A. Schekochihin, and T. Tatsuno. Kinetic simulations of magnetized turbulence in astrophysical plasmas. *Phys. Rev. Lett.*, 100(6):065004, 2008.

[53] G. G. Howes, J. M. Tenbarge, W. Dorland, E. Quataert, A. A. Schekochihin, R. Numata, and T. Tatsuno. Gyrokinetic simulations of solar wind turbulence from ion to electron scales. *Phys. Rev. Lett.*, 107(3):035004, 2011.

[54] B. D. G. Chandran and J. V. Hollweg. Alfvén wave reflection and turbulent heating in the solar wind from 1 solar radius to 1 au: An analytical treatment. *Astrophys. J.*, 707 (2):1659–1667, 2009.

[55] J. L. Burch, T. E. Moore, R. B. Torbert, and B. L. Giles. Magnetospheric Multiscale Overview and Science Objectives. *Space Science Reviews*, 199(1-4):5–21, 2016.

[56] T. Amano. Viewpoint: Inside a plasma shock. *Physics*, 9(117), OCT 2016.

[57] Instruments aboard mms. https://www.nasa.gov/mission_pages/mms/spacecraft/mms-instruments.html#ep. Accessed: 2020-02-03.

[58] F. Guo and J. Giacalone. The effect of large-scale magnetic turbulence on the acceleration of electrons by perpendicular collisionless shocks. *Astrophys. J.*, 715(1):406–411, 2010.

[59] R. E. Lowe and D. Burgess. The properties and causes of rippling in quasi-perpendicular collisionless shock fronts. *Annales Geophysicae European Geosciences Union*, 21(1): 671–679, 2003.

[60] D. Burgess. Simulations of electron acceleration at collisionless shocks: The effects of surface fluctuations. *Astrophys. J.*, 653(1):316–324, 2006.

[61] D. Morse, W. Destler, and P. Auer. Nonstationary behavior of collisionless shocks*. *Phys. Rev. Lett.*, 28(1):13–16, 1972.

[62] V. V. Krasnoselskikh, B. Lembége, P. Savoini, and V. V. Lobzin. Nonstationarity of strong collisionless quasiperpendicular shocks: Theory and full particle numerical simulations. *Phys. Plasmas*, 9(4):1192, 2002.

[63] A. Johlander, S. J. Schwartz, A. Vaivads, Yu. V. Khotyaintsev, I. Gingell, I. B. Peng, S. Markidis, P. A. Lindqvist, R. E. Ergun, G. T. Marklund, F. Plaschke, W. Magnes, R. J. Strangeway, C. T. Russell, H. Wei, R. B. Torbert, W. R. Paterson, D. J. Gershman, J. C. Dorelli, L. A. Avanov, B. Lavraud, Y. Saito, B. L. Giles, C. J. Pollock, and J. L. Burch. Rippled Quasiperpendicular Shock Observed by the Magnetospheric Multiscale Spacecraft. *Phys. Rev. Lett.*, 117(16), OCT 12 2016. ISSN 0031-9007.

[64] L. J. Chen, S. Wang, L. B. Wilson, S. Schwartz, N. Bessho, T. Moore, D. Gershman, B. Giles, D. Malaspina, F. D. Wilder, R. E. Ergun, M. Hesse, H. Lai, C. Russell, R. Strangeway, R. B. Torbert, F. A. Vinas, J. Burch, S. Lee, C. Pollock, J. Dorelli, W. Paterson, N. Ahmadi, K. Goodrich, B. Lavraud, O. Le Contel, Yu V. Khotyaintsev, P. A. Lindqvist, S. Boardsen, H. Wei, A. Le, and L. Avanov. Electron bulk acceleration and thermalization at earth's quasiperpendicular bow shock. *Phys. Rev. Lett.*, 120(1): 225101, 2018.

[65] J. G. Cordey. Effects of particle trapping on the slowing-down of fast ions in a toroidal plasma. *Nucl. Fusion*, 16(3):499–507, 1976.

[66] R. M. Kulsrud. Mhd description of plasma. In M. N. Rosenbluth and R. Z. Sagdeev, editors, *Handbook of Plasma Physics Vol. 1*, chapter 1, pages 115–145. North-Holland Publishing Company, New York, 1983.

[67] P. Montag, J. Egedal, E. Lichko, and B. Wetherton. Impact of compressibility and a guide field on fermi acceleration during magnetic island coalescence. *Phys. Plasmas*, 24 (1):062906, 2017.

[68] GI Taylor. The spectrum of turbulence. *Proceedings of the Royal Society*, 164(A919): 0476–0490, FEB 1938. ISSN 0080-4630.

[69] R. Shankar. *Principles of Quantum Mechanics*. Plenum Press, 1994.

[70] L. D. Landau and E. M. Lifshitz. *Mechanics*. Elsevier, 2010.

[71] J. D. Callen, K. J. Bunkers, and J. S. Kollasch. Lecture notes for plasma kinetic theory and radiation processes, September 2018.

[72] K. J. Bunkers. A magnetic fusion plasma physics primer. private communication, January 2020.

[73] G. Consolini. An introduction to kinetic plasma theories, September 2017.

[74] S. Ichimaru. *Statistical Plasma Physics*. Westview Press, 2004.

[75] D. C. Montgomery and D. A. Tidman. *Plasma Kinetic Theory*. McGraw-Hill Book Company, 1964.

[76] D. C. Montgomery. *Theory of the Unmagnetized Plasma*. Gordon and Breach, Science Publishers, 1971.

[77] K. Huang. *Statistical Mechanics*. John Wiley and Sons, Inc., 1987.

[78] Y. I. Kolesnichenko, M. Lisak, V. V. Lutsenko, and F. Wising. Space and velocity distributions of fast ions in magnetically confined plasmas. *Plasma Phys. Control. Fusion*, 37(1):363–386, 1995.

[79] P. Tracy, J. Kasper, J. Raines, P. Shearer, J. Gilbert, and T. Zurbuchen. Constraining Solar Wind Heating Processes by Kinetic Properties of Heavy Ions. *Phys. Rev. Lett.*, 116(25):255101, 2016.

[80] J.C. Kasper, K.G. Klein, M. Maksimovic, A. Zaslavsky, S.D. Bale, B.A. Maruca, M.L. Stevens, and A.W. Case. A zone of preferential ion heating extends tens of solar radii from the sun. *Astrophys. J.*, 849(2):126, 2017.

Appendix A

Magnetic Mirrors and Trapping

We consider a magnetic field that varies in space, but not in time. Because it is static, there are no induced electric fields and the particle's kinetic energy, $W = (m/2)(v_\parallel^2 + v_\perp^2)$, and magnetic moment, $\mu = mv_\perp^2/(2B)$, are both constant. From the form of W and μ we can see that if a particle enters a region of increasing magnetic field, $v \perp$ will need to increase for the magnetic moment to remain constant, which means that the parallel velocity, $v_\parallel$, will need to decrease in order for the kinetic energy to remain constant. If the magnetic field increases enough $v_\parallel$ will become zero and then the particle will be reflected back towards the weak field region. While the parallel velocity of the particle will increase as it enters the weak field region, for a sinusoidal field structure this process can trap both electrons and ions.

However, a particle moving in an increasing magnetic field will not necessarily be reflected. Naively, we can see this by considering a particle with $v_\parallel = v_0$ and $v_\perp = 0$, where the changing magnetic field will not change $v_\perp$, so $v_\parallel$ will remain unchanged as the particle passes through the region, "escaping" the trapped region. We can figure out which particles will be trapped by considering the marginally trapped particles and using the fact that the magnetic moment and kinetic energy are conserved in this system. We consider a region of increasing magnetic field where the minimum magnetic field is B_{min} and the maximum magnetic field is B_{max}, and $\theta v_\perp/v$ is the pitch-angle of the particle. We know that

$$\mu' \equiv \frac{2}{mv^2}\mu = \frac{\sin^2\theta}{B_{\min}} \tag{A.1}$$

is a constant. We are considering the marginally trapped particle, so we assume that the particle can reach the point $B = B_{\max}$. Its pitch-angel at that point must be limited by $\theta_{\max} < \pi/2$, so

$$\mu' = \frac{\sin^2\theta_{\max}}{B_{\max}} < \frac{1}{B_{\max}} \quad . \tag{A.2}$$

So the condition for particle starting at $B_{\min}$ that can reach the point $B_{\max}$ in the flux tube is

$$\sin^2\theta < \sin^2\theta_R = \frac{B_{\min}}{B_{\max}}. \tag{A.3}$$

If $\sin\theta > \sin\theta_R$ and the particle could reach $B_{\max}$ then we would have $\sin\theta > 1$, which is not possible, so in that case the particle cannot reach $B_{\max}$ and it is reflected before it reaches $B_{\max}$.